

REPORT DOCUMENTATION PAGE			1 Form Approved OMB NO. 0704-0188		
<p>The public reporting burden for this collection of information is estimated to average 1 hour per response, including the time for reviewing instructions, searching existing data sources, gathering and maintaining the data needed, and completing and reviewing the collection of information. Send comments regarding this burden estimate or any other aspect of this collection of information, including suggestions for reducing this burden, to Washington Headquarters Services, Directorate for Information Operations and Reports, 1215 Jefferson Davis Highway, Suite 1204, Arlington VA, 22202-4302. Respondents should be aware that notwithstanding any other provision of law, no person shall be subject to any penalty for failing to comply with a collection of information if it does not display a currently valid OMB control number.</p> <p>PLEASE DO NOT RETURN YOUR FORM TO THE ABOVE ADDRESS.</p>					
1. REPORT DATE (DD-MM-YYYY) 27-08-2014		2. REPORT TYPE Ph.D. Dissertation		3. DATES COVERED (From - To) -	
4. TITLE AND SUBTITLE Silicon quantum dots for quantum information processing			5a. CONTRACT NUMBER W911NF-13-1-0024		
			5b. GRANT NUMBER		
			5c. PROGRAM ELEMENT NUMBER		
6. AUTHORS Chih-Hwan Henry Yang			5d. PROJECT NUMBER		
			5e. TASK NUMBER		
			5f. WORK UNIT NUMBER		
7. PERFORMING ORGANIZATION NAMES AND ADDRESSES University of New South Wales Research Office University of New South Wales			8. PERFORMING ORGANIZATION REPORT NUMBER		
9. SPONSORING/MONITORING AGENCY NAME(S) AND ADDRESS (ES) U.S. Army Research Office P.O. Box 12211 Research Triangle Park, NC 27709-2211			10. SPONSOR/MONITOR'S ACRONYM(S) ARO		
			11. SPONSOR/MONITOR'S REPORT NUMBER(S) 63162-PH-OC.77		
12. DISTRIBUTION AVAILABILITY STATEMENT Approved for public release; distribution is unlimited.					
13. SUPPLEMENTARY NOTES The views, opinions and/or findings contained in this report are those of the author(s) and should not be construed as an official Department of the Army position, policy or decision, unless so designated by other documentation.					
14. ABSTRACT This thesis focuses on the development and demonstration of silicon metal-oxide-semiconductor (MOS) quantum dots (QDs) for spinbased quantum information processing. Firstly, by measuring the transport current through a MOS quantum dot, its multi-electron spin state was determined as the electron occupancy was reduced from twenty-seven electrons down to the single-electron limit. In particular, kinks observed in the electron addition energy as a function of magnetic field demonstrated that a valley-orbit excited state existed 100 meV above the ground state.					
15. SUBJECT TERMS Quantum computing, silicon quantum dots, quantum information processing, silicon metal-oxide-semiconductor (MOS)					
16. SECURITY CLASSIFICATION OF:			17. LIMITATION OF ABSTRACT UU	15. NUMBER OF PAGES	19a. NAME OF RESPONSIBLE PERSON Andrew Dzurak
a. REPORT UU	b. ABSTRACT UU	c. THIS PAGE UU			19b. TELEPHONE NUMBER 612-938-5631

Report Title

Silicon quantum dots for quantum information processing

ABSTRACT

This thesis focuses on the development and demonstration of silicon metal-oxide-semiconductor (MOS) quantum dots (QDs) for spinbased quantum information processing. Firstly, by measuring the transport current through a MOS quantum dot, its multi-electron spin state was determined as the electron occupancy was reduced from twenty-seven electrons down to the single-electron limit. In particular, kinks observed in the electron addition energy as a function of magnetic field demonstrated that a valley-orbit excited state existed 100 μ eV above the ground state. Secondly, by incorporating a silicon single-electron transistor (SET) charge sensor next to a quantum dot, the electron occupancy of the dot was probed via the sensor output signal. By applying a digitally-controlled dynamic feedback loop to the charge sensor, robust detection of the QD charge state was achieved, even in the presence of charge drifts and random charge upset events. Next, the excited states of a silicon MOS quantum dot were studied in detail. The electron occupancy and excited-state energy levels were detected using a SET charge sensor, with the aid of pulsed-voltage spectroscopy. The energy of the first orbital excited state was found to decrease rapidly as the electron occupancy increased from $N = 1$ to 4. By monitoring the sequential spin filling of the dot a valley splitting of $\sim 230 \mu$ eV was extracted, which was found to be independent of electron number. Finally, by performing single-shot spin readout on a silicon MOS quantum dot, spin lifetimes were extracted for different electron occupancies and valley splitting configurations, with a maximum one-electron spin lifetime exceeding 2 seconds. We also demonstrated the ability to tune the valley splitting energy via electrostatic gate control, with a splitting that increased linearly with applied electric field over the range 0.3 - 0.8 meV. The spin relaxation rates were found to be highly dependent on the valley splitting energy, with a dramatic rate enhancement (or hot-spot) when the Zeeman and valley splittings coincided, a process that had not previously been anticipated for silicon quantum dots.

Silicon quantum dots for quantum information processing

Chih-Hwan Henry YANG

A thesis in fulfilment of the requirements for the degree of
Doctor of Philosophy



School of Electrical Engineering and Telecommunications

University of New South Wales

November 2013

Abstract

This thesis focuses on the development and demonstration of silicon metal-oxide-semiconductor (MOS) quantum dots (QDs) for spin-based quantum information processing. Firstly, by measuring the transport current through a MOS quantum dot, its multi-electron spin state was determined as the electron occupancy was reduced from twenty-seven electrons down to the single-electron limit. In particular, kinks observed in the electron addition energy as a function of magnetic field demonstrated that a valley-orbit excited state existed $100\text{ }\mu\text{eV}$ above the ground state.

Secondly, by incorporating a silicon single-electron transistor (SET) charge sensor next to a quantum dot, the electron occupancy of the dot was probed via the sensor output signal. By applying a digitally-controlled dynamic feedback loop to the charge sensor, robust detection of the QD charge state was achieved, even in the presence of charge drifts and random charge upset events.

Next, the excited states of a silicon MOS quantum dot were studied in detail. The electron occupancy and excited-state energy levels were detected using a SET charge sensor, with the aid of pulsed-voltage spectroscopy. The energy of the first orbital excited state was found

to decrease rapidly as the electron occupancy increased from $N = 1$ to 4. By monitoring the sequential spin filling of the dot a valley splitting of $\sim 230 \mu\text{eV}$ was extracted, which was found to be independent of electron number.

Finally, by performing single-shot spin readout on a silicon MOS quantum dot, spin lifetimes were extracted for different electron occupancies and valley splitting configurations, with a maximum one-electron spin lifetime exceeding 2 seconds. We also demonstrated the ability to tune the valley splitting energy via electrostatic gate control, with a splitting that increased linearly with applied electric field over the range 0.3 - 0.8 meV. The spin relaxation rates were found to be highly dependent on the valley splitting energy, with a dramatic rate enhancement (or hot-spot) when the Zeeman and valley splittings coincided, a process that had not previously been anticipated for silicon quantum dots.

To all my loved ones.

Acknowledgements

First of all, I would like to thank my supervisor, Prof. Andrew Dzurak, for his encouragement, guidance and support from the beginning to the end of the research. I have been involved with his research in Centre for Quantum Computer and Communication Technology (formerly Centre for Quantum Computer Technology) since my undergraduate summer research program, with guidance from Dr. Chris Escott, who has been taking good care of me through out my undergraduate research. Then I completed my undergraduate thesis with them and continued on with a PhD research program.

I am grateful to all the members within the centre that have made my research being successful. I am very thankful to my seniors friends Dr. Wee Han Lim, Dr. Nai Shyan Lai, Dr. Kok Wai Chan and Dr. Kuan Yen Tan where we have shared most of the time within the research, lunches, and other activities. I would also like to thank to A.Prof. Andrea Morello, Dr. Floris Zwanenburg, Dr. Jarryd Pla, Bob Starett and Dave Barber for their guidance in measurements.

Special thanks to Fahd Mohiyaddin on modelling discussions, and Dr. Alessandro Rossi on assisting my measurements and journal paper writing ups. Finally, I also thank to my juniors Jason Cheng, Chandni

Ravi and Jason Hwang where we enjoyed our times within and outside research. This thesis would not be possible or this smooth without all the help from everyone. I also thank to Elite Editing for grammatical editing of this thesis.

Publications

Peer reviewed journal articles

W. H. Lim, **C. H. Yang**, F. A. Zwanenburg and A. S. Dzurak, **Spin filling of valley-orbit states in a silicon quantum dot**, *Nanotechnology* **22**, 335704 (2011).

C. H. Yang, W. H. Lim, F. A. Zwanenburg and A. S. Dzurak, **Dynamically controlled charge sensing of a few-electron silicon quantum dot**, *AIP Advances* **1**, 042111 (2011).

N. S. Lai, W. H. Lim, **C. H. Yang**, F. A. Zwanenburg, W. A. Coish, F. Qassemi, A. Morello and A. S. Dzurak, **Pauli spin blockade in a highly tunable silicon double quantum dot**, *Scientific Reports* **1**, 110 (2011).

C. H. Yang, W. H. Lim, N. S. Lai, A. Morello and A. S. Dzurak, **Orbital and valley state spectra of a few-electron silicon quantum dot**, *Physical Review B* **86**, 115319 (2012).

C. H. Yang, A. Rossi, R. Ruskov, N. S. Lai, F. A. Mohiyaddin, S. Lee, C. Tahan, G. Klimeck, A. Morello and A. S. Dzurak, **Spin-valley lifetimes in a silicon quantum dot with tunable valley splitting**, *Nature Communications* **4**, 2069 (2013).

L. Jiang, **C. H. Yang**, Z. Pan, A. Rossi, A. S. Dzurak and D. Culcer, **Coulomb interaction and valley-orbit coupling in Si quantum dots**, *Physical Review B* **88**, 085311 (2013).

Presentations

C. H. Yang, W. H. Lim, F. A. Zwanenburg and A. S. Dzurak, **Spin filling in a few-electron Si quantum dot**, *The 10th International Conference on Quantum Communication, Measurement and Computation*, Brisbane, Australia, July 2010 (Poster).

C. H. Yang, W. H. Lim, A. S. Dzurak, **Dynamically controlled charge sensing in a few-electron silicon quantum dot**, *The 19th Australian Institute of Physics Congress*, Melbourne, Australia, December 2010 (Poster).

C. H. Yang, W. H. Lim, N. S. Lai, A. Morello and A. S. Dzurak, **Excited-state spectroscopy in a few-electron silicon quantum dot via charge sensing and pulsed gating**, *6th Interna-*

tional School and Conference on Spintronics and Quantum Information Technology (SPINTECH6), Matsue, Japan, August 2011 (Poster).

C. H. Yang, W. H. Lim, N. S. Lai, A. Morello and A. S. Dzurak, **Excited-state spectroscopy in a few-electron silicon quantum dot via charge sensing and pulsed gating**, *International Workshop on Silicon Quantum Electronics*, Denver, USA, August 2011 (Poster).

C. H. Yang, W. H. Lim, N. S. Lai, A. Morello and A. S. Dzurak, **Orbital and valley state spectra of a one-electron silicon quantum dot probed via charge sensing**, *International Workshop on Silicon Quantum Electronics*, Sydney, Australia, February 2012 (Oral).

C. H. Yang, N. S. Lai, A. Rossi, A. Morello and A. S. Dzurak, **Single-shot measurement of spin lifetimes for $N=1,2$ & 3 electron states in a multi-valley silicon quantum dot**, *Quantum Computing Program Review*, Denver, USA, August 2012 (Poster).

C. H. Yang, N. S. Lai, A. Rossi, A. Morello and A. S. Dzurak, **Spin lifetime in silicon quantum dots with tunable valley splitting**, *The 20th Australian Institute of Physics Congress*, Sydney, Australia, December 2012 (Poster).

C. H. Yang, N. S. Lai, A. Rossi, A. Morello and A. S. Dzurak,
Electron Spin lifetimes in multi-valley silicon quantum dots,
Coogee Bay Meeting, Sydney, Australia, December 2012 (Oral).

C. H. Yang, A. Rossi, R. Ruskov, N. S. Lai, C. Tahan, A. Morello
 and A. S. Dzurak, **Electron Spin lifetimes in multi-valley silicon quantum dots**, *S3NANO Winter School Few spin solid-state nanosystems*, Windsor, UK, February 2012 (Poster).

C. H. Yang, A. Rossi, R. Ruskov, N. S. Lai, C. Tahan, A. Morello
 and A. S. Dzurak, **Electron Spin lifetimes in multi-valley silicon quantum dots**, *International Workshop on Silicon Quantum Electronics*, Grenoble, France, February 2012 (Poster).

C. H. Yang, A. Rossi, N. S. Lai, F. A. Mohiyaddin, A. Morello and
 A. S. Dzurak, **Valley splitting control in silicon quantum dots**,
Centre for Quantum Computer Technology Annual Workshop, Sunshine Coast, Australia, May 2013 (Oral).

Table of Contents

Abstract	iii
Acknowledgements	vii
Publications	ix
Table of Contents	xiii
Abbreviations and Symbols	xvii
List of Figures	xix
List of Tables	xxiii
1 Introduction	1
1.1 Preamble	2
1.2 Quantum Computers	2
1.3 Thesis Outline	4
2 Background Knowledge and Literature Review	7
2.1 Spin Qubit Basics	8
2.1.1 Electron Spin	8
2.1.2 Spin Readout	10
2.1.3 Spin Manipulation	11
2.1.4 Spin Lifetime	11

TABLE OF CONTENTS

2.2	Quantum Dot Structures in Other Material Systems	15
2.2.1	GaAs/AlGaAs Heterostructures	16
2.2.2	Si/SiGe Heterostructures	18
2.2.3	Silicon Nanowires	19
2.2.4	Carbon Nanotubes	20
2.2.5	Graphene	20
2.3	Silicon Device Physics	21
2.3.1	Silicon Band Structure	21
2.3.2	Silicon-based MOS Devices	26
2.3.3	Conduction-band Valleys in Silicon	27
2.4	Silicon Quantum Dot Physics	29
2.4.1	Electron Confinement in a Quantum Dot	29
2.4.2	Coulomb Blockade	30
2.4.3	Single Electron Transport through a Quantum Dot	32
2.4.4	Pulsed-Gate Spectroscopy Measurements	35
2.4.5	Quantum Dot Excited States	37
3	Experimental Methods	41
3.1	Device Fabrication	42
3.1.1	Optical Patterning of Ohmic Contacts and Oxide Growth	42
3.1.2	Electron Beam Lithography of Gates and Alignment Markers	42
3.1.3	Annealing and Packaging	44
3.2	Design of Device Structures	44
3.2.1	Multi-layer Gate Structure	45
3.2.2	Integrated SET Charge Sensor	47

TABLE OF CONTENTS

3.2.3	Extension to Multiple Dots and Qubits	47
3.3	Measurement	48
3.3.1	4 K Dewar Measurements	48
3.3.2	Dilution Refrigerator Measurements	49
3.3.3	Electronic Measurement Equipment	51
4	Spin Filling of Valley-Orbit States	53
4.1	Introduction	54
4.2	Device Architecture	54
4.2.1	Measurement Configuration	56
4.3	Transport Measurements and Bias Spectroscopy	56
4.4	Spin Filling	58
4.4.1	Valley-Orbit States	58
4.4.2	Spin State Characterisation via Magnetospectroscopy . . .	59
4.4.3	Spin Filling for $N = 2$ to 4 Electrons	61
4.4.4	Spin Filling for $N = 5$ to 12 Electrons	64
4.5	Conclusions	66
5	Dynamically Controlled Charge Sensing	67
5.1	Introduction	68
5.2	Device Architecture and Measurement Set-up	69
5.3	Charge Sensing Results for a Single QD	72
5.4	Conclusions	78
6	Excited State Spectroscopy of Orbital and Valley Levels	79
6.1	Introduction	80
6.2	Device Architecture and Measurement Set-up	80

TABLE OF CONTENTS

6.3	Quantum Dot Occupancy and Measurement of Excited States . .	85
6.4	Orbital State Spectrum	87
6.5	Spin and Valley Level Filling	89
6.6	Conclusions	94
7	Spin-Valley Lifetimes in a QD with Tunable Valley Splitting	97
7.1	Introduction	98
7.2	Quantum Dot Occupancy and Shell Structure	99
7.3	Single-Shot Spin Readout and Spin-Valley Lifetimes for $N = 1$ Electron	105
7.4	Theory of Spin-Valley Mixing in a Silicon QD	109
7.5	Spin-Valley Relaxation for $N = 2$ Electron States	113
7.6	Valley Splitting Control via Electric Field Tuning	118
7.6.1	TCAD Modelling	123
7.7	Conclusions	125
8	Conclusion	127
8.1	Key Achievements	128
8.2	Future Work	129
	References	131

Abbreviations and Symbols

1D	One-dimensional
2D	Two-dimensional
2DEG	Two-dimensional electron gas
3D	Three-dimensional
AC	Alternating current
Al	Aluminium
Al_xO_y	Aluminium oxide
AlGaAs	Aluminium gallium arsenide
ANFF	Australian National Fabrication Facility
BNC	Bayonet Neill-Concelman
CNOT	Controlled-not gate
CPU	Central processing unit
DC	Direct current
DCE	dichloroethylene
EBL	Electron beam lithography
ESR	Electron spin resonant
GaAs	Gallium arsenide
GPIO	General purpose interface bus
HF	Hydrofluoric acid
InGaAs	Indium gallium arsenide

ABBREVIATIONS AND SYMBOLS

IPA	Isopropanol
MIBK	methy-isobutyl-ketone
MOS	Metal-oxide-semiconductor
MOSFET	Metal-oxide-semiconductor field effect transistor
NML	National Magnet Laboratory
NMP	1-methyl-2-pyrrolidone
NPGS	Nanometer pattern generation system
PMMA	Polymethyl-methacrylate
QD	Quantum dot
QPC	Quantum point contact
SEM	scanning electron microscope
SET	Single electron transistor
Si	Silicon
SiGe	Silicon germanium
SiO₂	Silicon dioxide
SMU	Source-measure unit
SOC	Spin-orbit coupling
SOI	Spin-orbit interaction
SWAP	Swap gate
TCAD	Technology computer aided design
XTEM	Cross-sectional transmission electron microscopy

List of Figures

2.1	Bloch sphere	9
2.2	Spin lifetime and spin decoherence	12
2.3	Magnetic field from spin-orbit interaction	14
2.4	Vertical quantum dot	17
2.5	Energy levels in silicon	23
2.6	Band structure of bulk silicon in k-space	24
2.7	Band diagram of MOS device	26
2.8	Valley composition in silicon	28
2.9	Schematic of a single QD	30
2.10	Transport current Coulomb peaks and diamonds in a single QD .	31
2.11	Transport through a single QD	32
2.12	Transport through a single QD with excited states	34
2.13	Energy-selective tunnelling from reservoir	36
2.14	Origin of excited states in a QD	38
2.15	Change of excited-state energies under changing conditions	39
3.1	QD with triple-layer gate stack structure	45
3.2	Dilution refrigerator	49

LIST OF FIGURES

4.1	Single Dot Device Architecture	55
4.2	Coulomb Diamonds of Single Dot Device	57
4.3	Coulomb Peaks from $N = 1$ to 27	58
4.4	Stability Diagram of V_{B2} v.s. V_P	60
4.5	Spin filling of $N = 1, 2$	61
4.6	Spin filling of $N = 3, 4$	63
4.7	Spin filling of $N = 5$ to 12	65
5.1	Single Dot with Charge Sensor	70
5.2	Feedback Controller Block Diagram	71
5.3	Charge Sensor and Transport Currents	73
5.4	Stability Diagram with Charge Sensor	77
6.1	Single Dot with Charge Sensor	81
6.2	Pulsing Schematic	83
6.3	Charge Stability Diagram via Charge Sensor	84
6.4	Observation of Excited state via Charge Sensor	86
6.5	Excited state observation through pulse lock-in	88
6.6	Magneto-spectroscopy of the first 4 electrons	90
7.1	Device architecture	100
7.2	Device architecture 3D view	101
7.3	Filling energy of the QD	103
7.4	Spin readout for single-electron occupancy.	106
7.5	Energy spectrum and spin relaxation rates for single-electron oc- cupancy.	108

LIST OF FIGURES

7.6	Spin-valley relaxation for 2-electron occupancy.	114
7.7	Spin-valley relaxation for 3-electron occupancy.	117
7.8	Extraction of valley splitting energies.	119
7.9	Tunability of the valley splitting via gate-voltage control.	121
7.10	TCAD simulation model of the device.	123
7.11	Extracted data from TCAD simulation.	124

LIST OF FIGURES

List of Tables

2.1	Silicon properties.	22
7.1	Comparison of experimental and calculated tunabilities.	122
8.1	Comparison between generations of devices	128

LIST OF TABLES

Chapter 1

Introduction

‘The journey of a thousand miles begins with a single step.’

Lao Tzu

1. INTRODUCTION

1.1 Preamble

Silicon is one of the most widely used materials in our digital society. Silicon semiconductor industries offer us powerful computation systems, such as personal computers, mobile phones and electronic instruments. One of the key technologies used for their production these devices is the silicon metal-oxide-semiconductor (MOS) device structure. This technology has been growing exponentially in terms of speed, cost and fields of application. To maintain this growth, MOS transistors are becoming smaller, enabling them to be packed into one computer chip. But there are physical limitations to their size, such as the size of the atom; more importantly, there are limitations imposed by quantum physics in the nanoscale world.

1.2 Quantum Computers

Integrated circuit technologies began to boom in the mid-nineteenth century. In 1965, Gordon E Moore, the co-founder of Intel, predicted that the number of transistors on an integrated chip would double every 18 months [1]. This trend, following ‘Moore’s law’, has continued up until today, when a modern computers central processing unit (CPU) consists of billions of transistors, and the number keeps growing. However, exponential growth cannot continue forever because the transistors cannot be shrunk infinitely small.

When they are only nanometers (nm) in size, particles do not behave like ‘normal’ objects because quantum mechanical effects such as particle-wave duality, tunnelling and superpositions occur. While quantum mechanics may impose barriers to making the transistors even smaller, devices at these scales can also

1.2 Quantum Computers

be used in a new type of computation system in which the quantum states of elementary particles can store and process information. In such new *quantum* computation systems, the equivalent of a bit is a quantum bit (or qubit). Because qubits can exist in a quantum superposition of a logic ‘0’ and logic ‘1’ state simultaneously, it is possible to store 2^N integers in an N -qubit register, for exceeding the storage of classical computers.

During the 1980s, Richard Feynman said, ‘Nature isn’t classical ... and if you want to make a simulation of Nature, you’d better make it quantum mechanical, and by golly it’s a wonderful problem, because it doesn’t look so easy.’ [2]. At that time, the field of quantum computation an interesting concept in theoretical physics, but it was difficult to implement such a quantum computer with the technologies available.

In the 1990s, several quantum computation algorithms were proposed to solve realistic problems, including Shor’s factoring algorithm to factorise large numbers [3], and Grover’s search algorithm to perform fast database searching [4]. Both algorithms have been proven to solve problems much more efficiently than classical computers. For example, by performing Shor’s factoring algorithm on a large-scale quantum computer, encryptions relying on the product of two large prime numbers can be decrypted in polynomial time. Where classical computers may take centuries to factorise these huge numbers, a quantum computer could solve the problem within seconds.

Over the past decades, many different architectures and physical systems have been investigated for the realisation of a large-scale quantum computer. These systems include ion traps [5], photons [6], charge states in superconductors [7], charge [8, 9] and spin states [10, 11] in quantum dots (QDs), flux in superconduc-

1. INTRODUCTION

tors [12] and many more. In 1998, Bruce Kane proposed a silicon donor-based structure to realise a quantum computer [13]. This proposal can be adapted to the current silicon semiconductor industry, where, in terms of scalability, the silicon integrated circuit has clear advantages over other material platforms.

In this thesis, we follow the silicon integrated circuit architecture path, and utilise previous work on silicon MOS QDs [14, 15]. We fabricate and perform experiments on this type of QD in pursuit of the holy grail of a quantum computer. For the first time, we demonstrate the ability to extract the spin filling of a silicon MOS QD, and successfully integrate a nearby single-electron transistor. We reveal the quantum state composition of a silicon QD, where spin, valley and orbital states can be identified. Using a single-shot spin-readout experiment and an ability to control the valley-splitting energy, we discover a new mechanism to demonstrate that spin lifetimes are perturbed by valley states in silicon.

1.3 Thesis Outline

The thesis is divided into eight chapters.

Chapter 1 provides a brief introduction to our motivation for building a quantum computer.

Chapter 2 covers background knowledge and similar work carried out previously. We demonstrate how the spin of an electron can perform qubit operations, and the issues involved. A summary of different qubit architectures is presented for comparison with our silicon MOS structure. The basic physics properties of silicon, and the advantages of using this material to realise a spin-based qubit,

1.3 Thesis Outline

are discussed. Common experimental methods of operating and studying a QD are listed, as are the fundamentals of the main chapters.

Chapter 3 provides an overview of the fabrication and experimental methods. A list of equipment and fabrication recipes are presented, and details of how we pattern our silicon MOS QD device are specified. The basic techniques and instruments for performing experiments under cryogenic conditions are also given.

Chapter 4 demonstrates a low-disorder Si MOS QD containing a tunable number of electrons from zero to 27. The observed evolution of addition energies with parallel magnetic field reveals the spin filling of electrons into valley-orbit states. We find a splitting of 0.10 meV between the ground and first excited states, consistent with theory and placing a lower bound on the valley splitting. Our results prove optimism for the realisation of spin qubits based on silicon QDs in the near future.

Chapter 5 reports charge-sensing measurements of a silicon MOS QD using a single-electron transistor as a charge sensor with dynamic feedback control. Using digitally controlled feedback, the sensor exhibits sensitive and robust detection of the charge state of the QD, even in the presence of charge drifts and random charge upset events. The sensor enables the occupancy of the QD to be probed down to the single-electron level.

Chapter 6 reports studies of the energy spectra of a few-electron silicon MOS QD using dynamic charge sensing and pulsed-voltage spectroscopy. The occupancy of

1. INTRODUCTION

the QD is probed down to the single-electron level using a nearby single-electron transistor as a charge sensor. The energy of the first orbital excited state is found to decrease rapidly as the electron occupancy increases from $N = 1$ to 4. By monitoring the sequential spin-filling of the dot, we extract a valley-splitting of $\sim 230 \mu\text{eV}$, irrespective of electron number. This indicates that favourable conditions for qubit operation are in place in the few-electron regime.

Chapter 7 demonstrates that valley separation can be accurately tuned via electrostatic gate control in a MOS QD, providing splittings spanning 0.3 - 0.8 meV. The splitting varies linearly with applied electric field, with a ratio in agreement with atomistic tight-binding predictions. We demonstrate single-shot spin readout and measure the spin relaxation for different valley configurations and dot occupancies, finding one-electron lifetimes exceeding 2 seconds. Spin relaxation occurs via phonon emission due to spin-orbit coupling between the valley states, a process not previously anticipated for silicon QDs.

Chapter 8 concludes the thesis by revising the key breakthroughs within the experimental chapters. Engineering a silicon MOS QD, and reading and analysing the spin states, has brought us closer to realising a qubit. We discuss the future work required to reach this goal.

Chapter 2

Background Knowledge and Literature Review

This chapter covers background knowledge and related work carried out previously, including how the spin of an electron can perform qubit operations, and the issues involved. A summary of different qubit architectures is presented for comparison with our silicon MOS structure. The basic physic properties of silicon are discussed, as well as the advantages of using this material to realise a spin-based qubit. Common experimental methods of operating and studying a QD are listed, as are the fundamental concepts used in the main experimental results chapters.

2. BACKGROUND KNOWLEDGE AND LITERATURE REVIEW

2.1 Spin Qubit Basics

2.1.1 Electron Spin

Spin is the angular momentum carried by elemental particles, which can be visualised as spinning tops. Spin is a quantised property: each particle has only a set of available spin eigenstates. A boson, such as a single photon, carries an integer spin number, either -1 , 0 or 1 . Fermions, such as electrons, protons and neutrons can carry a spin number of $-1/2$ or $1/2$. According to the Pauli exclusion principle, any particle that carries a half-integer spin cannot share the same quantum state with any other particle, which leads to the key principles of solid state behaviour. This thesis focuses on the spin properties of electrons in silicon, in particular the ability of the electron spin to serve as a spin qubit, to store quantum information.

An electron with spin $-1/2$ is referred to as ‘spin-down’, while an electron with spin $1/2$ is referred to as ‘spin-up’. These are the eigenstates (the only two states that are measurable) of the single-electron system. The two spin states of an electron are degenerate in zero magnetic field (See also Chapter 2.4.5) and the degeneracy is lifted when a field is applied. By convention, the magnetic field direction along which the spin aligns is defined to as the ‘z-direction’, B_z . Unlike for classical information, the electron has only one pure state, although the quantum state of the electron can be a superposition of spin-up and spin-down, denoted as:

$$|\psi\rangle = \alpha |\uparrow\rangle + \beta |\downarrow\rangle \quad (2.1)$$

where $|\alpha|^2 + |\beta|^2 = 1$ and α and β are the complex amplitudes of spin-up and spin-down states respectively.

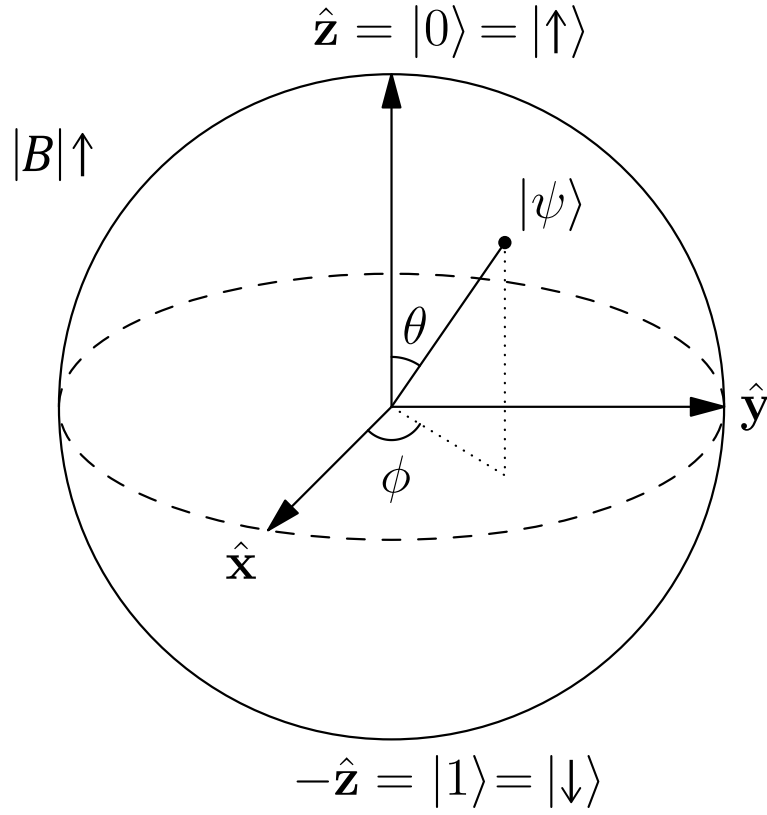


Figure 2.1: Bloch sphere - Bloch sphere representation of the electron spin state with complex amplitudes of spin-up $|\uparrow\rangle$ and spin-down $|\downarrow\rangle$, where $|\psi\rangle = \cos \frac{\theta}{2} |\uparrow\rangle + e^{i\phi} \sin \frac{\theta}{2} |\downarrow\rangle$.

2. BACKGROUND KNOWLEDGE AND LITERATURE REVIEW

To visualise the spin state, the Bloch sphere is a spherical surface coordinate system that represents the spin with any complex value of α and β . This then transforms the state into:

$$|\psi\rangle = \cos \frac{\theta}{2} |\uparrow\rangle + e^{i\phi} \sin \frac{\theta}{2} |\downarrow\rangle \quad (2.2)$$

Since the global phase does not affect the quantum state, the entire wavefunction can be multiplied by an overall phase factor (a complex number with unity magnitude). Figure 2.1 displays the Bloch sphere that represents the spin direction in three-dimensional (3D) space. When $\theta = 0, \pi$, this gives $|\psi\rangle = |\uparrow\rangle, |\downarrow\rangle$ which aligns and anti-aligns the spin with the z-direction. To have the spin pointing in the x- or y-direction, $\theta = \frac{\pi}{2}$ and $\phi = 0, \frac{\pi}{2}$ is required, and the spin states are $|\psi\rangle = \frac{1}{\sqrt{2}}(|\uparrow\rangle + |\downarrow\rangle), \frac{1}{\sqrt{2}}(|\uparrow\rangle + i|\downarrow\rangle)$ respectively. From the Bloch sphere diagram, we can easily see where the spin direction is pointing with two complex coefficients, which are technically generated by two basis states (spin-up and spin-down).

2.1.2 Spin Readout

To operate the electron-spin two-level system as a spin qubit, the ability to read out the spin state is essential. As mentioned previously, the measurable states of the system can only be the eigenstates of the Hamiltonian for the system, namely the pure spin-up and spin-down states, $|\psi\rangle = |\uparrow\rangle, |\downarrow\rangle$. When a readout process occurs, an electron carrying a mixed-spin state, $|\psi\rangle = \alpha |\uparrow\rangle + \beta |\downarrow\rangle$ will be projected onto either $|\uparrow\rangle$ or $|\downarrow\rangle$, with probability $|\alpha|^2$ and $|\beta|^2$ respectively.

In Section 7.3, we show how an individual electron spin in a silicon QD can be read out using the spin-charge conversion method.

2.1.3 Spin Manipulation

Spin manipulation is the basic process by which computations can be performed on spin qubit systems. Such manipulations include the rotation of a single spin about any axis, which can realise a quantum-NOT (or qNOT) gate, and also multi-qubit operations such as the CNOT (controlled-NOT) gate, the SWAP gate, and other universal quantum gates. A qNOT gate simply rotates the spin-up/down state to the opposite state. This can be written in matrix form as:

$$X = \begin{bmatrix} 0 & 1 \\ 1 & 0 \end{bmatrix} \quad (2.3)$$

where X is the operator that rotates the spin around the x-axis by 180° . Experimentally, electron spin can be manipulated using coherent controls such as ESR (electron-spin resonance) for single spins, and gate-controlled exchange coupling for pairs of spins. The spin states remain in superposition states or entangled states until the states are read out or they decay into a lower energy state. Hence, during a series of spin manipulations, the actual states cannot be observed before the computation is completed. In this thesis, the manipulation of electron spins is not presented, but workers in this field have demonstrated semiconductor-based electron-spin qubits in a variety of systems over the past few years [11, 16, 17, 18, 19, 20].

2.1.4 Spin Lifetime

Despite having readable and controllable qubits, the spin states are coupled to the environment, which is able to dephase the states. Several key dephasing mechanisms are present for a semiconductor-based spin qubit, including charge

2. BACKGROUND KNOWLEDGE AND LITERATURE REVIEW

noise, phonon and spin bath.

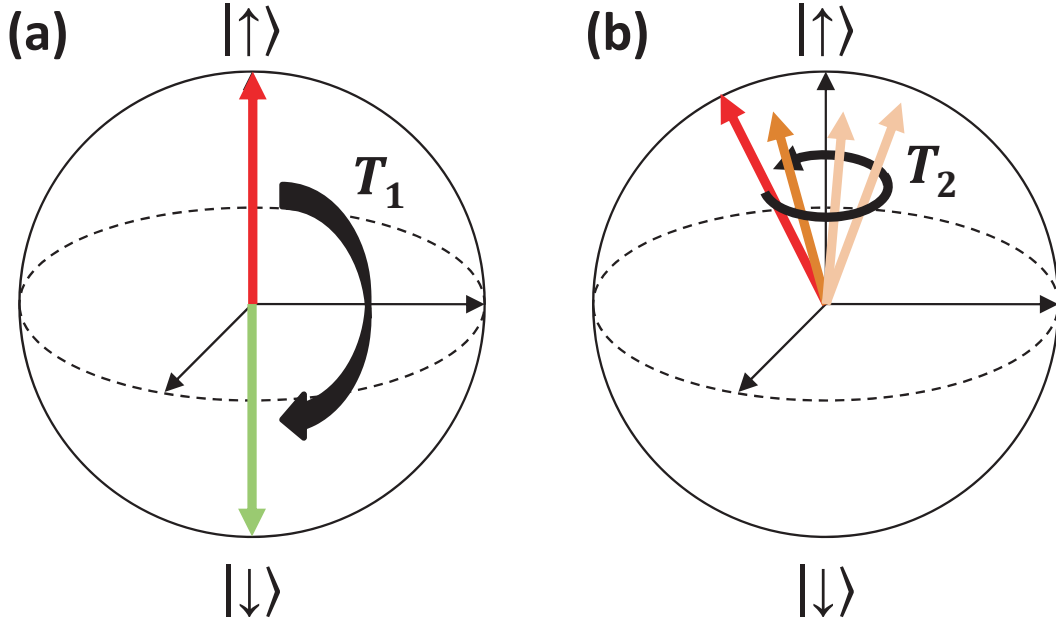


Figure 2.2: Spin lifetime and spin decoherence - (a) Spin lifetime, T_1 , the time taken for a spin to relax to a ground state. (b) Decoherence time, T_2 , the time taken for the spin to dephase around the spin axis with 2π .

The spin lifetime, denoted T_1 , is the time an excited spin state takes to relax to the ground state, see Figure 2.2 (a). T_1 can be determined from repeated spin readout events to extract the decay rate of the excited spin by fitting to the equation:

$$S_1(t) = S_{init} \exp(-t/T_1) \quad (2.4)$$

2.1 Spin Qubit Basics

where $S(t)$ is the probability of the excited spin state over a waiting time, t , and S_{init} is the excited spin initial probability in the system.

The spin decoherence time, T_2 , is the time taken for the spin to dephase around the spin axis. As seen in Figure 2.2 (b), T_2 does not change the spin projection on the spin axis (if $T_2 \ll T_1$), but it destroys most coherent operations, including ESR and qubit operations, where they are required to rotate the spin without causing dephasing. T_2 is extracted in a similar way to T_1 , but instead of waiting for the time t before the readout, a spin-resonance signal is applied during this time t . The resonance signal rotates the spin around the spin-up and spin-down, until the spin is fully dephased across the Bloch sphere and has a final excited spin probability of S_{fin} :

$$S_2(t) = (S_{init} - S_{fin}) \cos(rt) \exp(-t/T_2) + S_{fin} \quad (2.5)$$

where $\cos(rt)$ represents the spin-resonance-driven oscillation. By collecting the envelope of $S_2(t)$, the T_2 can be extracted by fitting the decay rate. Generally, T_2 is much shorter than T_1 , and there is a boundary of $T_2 \leq 2T_1$ as the time taken to reach the ground state cannot be faster than its dephasing speed. This thesis focuses on T_1 measurements and analysis only.

A pure spin does not couple to an electric field directly; the strongest way for the electric field to interact with the spin is via spin-orbit coupling (SOC). As long as an electron possesses an angular momentum within its own orbital, an internal magnetic field \vec{m} is generated under an electric field, given by $\vec{m} = \vec{E} \times \vec{p}$. This \vec{m} generated by the electron then interacts with its own spin, and causes the spin to dephase. The two common types of spin-orbit interaction (SOI) are named ‘Rashba’ [21, 22] and ‘Dresselhaus’ [23, 24, 25]. Figure 2.3 shows the difference

2. BACKGROUND KNOWLEDGE AND LITERATURE REVIEW

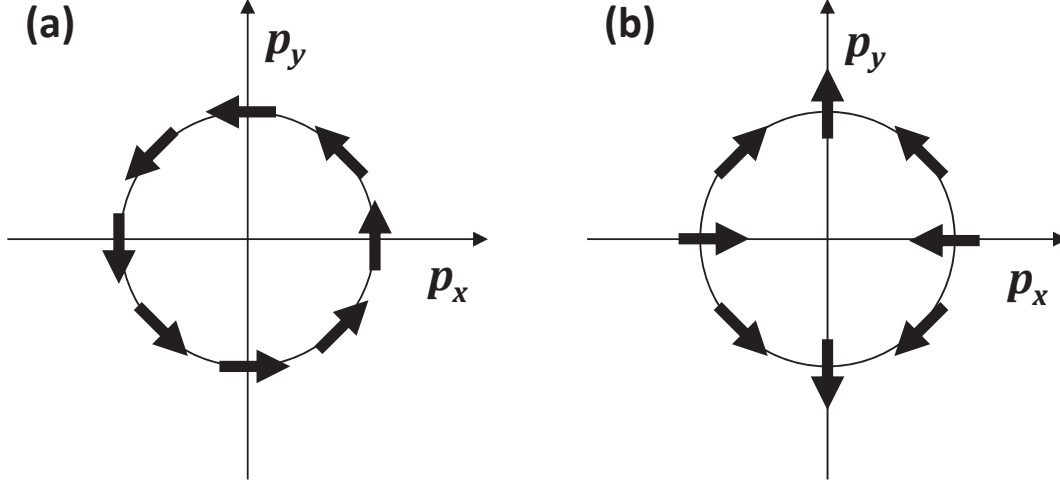


Figure 2.3: Magnetic field from spin-orbit interaction - The internal magnetic field generated by electrons with momentum of p_x and p_y , in different types of spin-orbit interaction (SOI): (a) Rashba SOI, α_R (b) Dresselhaus SOI, β_D

between (a) Rashba and (b) Dressulhaus SOIs. These types of SOC can exist at the same time and affect the T_1 and T_2 of electrons.

Once the spin can couple to an electric field via SOI, electric field fluctuations [26, 27] are able to reduce the electron-spin lifetime and decoherence time. However, the effect of such an electric field fluctuation is not strong enough to greatly reduce the spin lifetimes [28], as reported in many experiments [20, 29, 30, 31, 32, 33, 34, 35, 36, 37]. The fluctuation is typically caused by the gate potential noise or other nearby charge fluctuations around the system [38, 39], but the major electric field noise comes from the phonon bath [32]. Phonons can deform the lattice spacing and change the bandgap of the semiconductor, creating an electric field fluctuation. In polar crystals like gallium arsenide (GaAs), phonons can also change the electric field via the piezoelectric effect. The wavelength of the phonons is another important factor in reducing spin lifetime: the closer the wavelength is to the QD size, the faster the spin

2.2 Quantum Dot Structures in Other Material Systems

relaxes through SOC [40, 41, 42].

With the combination of SOC and the Zeeman effect, the typical dependency of a spin lifetime can be expressed as:

$$T_1^{-1} \propto \Delta E_Z^5 / \Delta E_{orb}^4 \quad (2.6)$$

where ΔE_Z is the Zeeman splitting energy and ΔE_{orb} is the orbital energy. In a QD system with a single valley only, piezoelectric phonons dominate [27, 43, 44]. This dependency has been observed in a GaAs QD [28, 45] and a single-donor spin qubit in silicon [46]. When the valley degree of freedom in a QD is involved, an extra ΔE_Z^2 dependency is predicted due to the Rashba SOC [28, 44, 47]:

$$T_1^{-1} \propto \Delta E_Z^7 / \Delta E_{orb}^4 \quad (2.7)$$

However, in Chapter 7, we report that an even more complicated spin-lifetime mechanism exists, which involves a spin-valley interaction due to SOI, in which the valley-splitting energy dominates and creates a ‘hot-spot’, where the T_1 grows significantly when $\Delta E_Z \sim \Delta E_{VS}$.

2.2 Quantum Dot Structures in Other Material Systems

QDs are tiny systems confined in all three spatial dimensions, for example, electrons in semiconductors confined via gate-defined electric fields. The idea of using QDs to implement a spin-based quantum computer was proposed by Daniel Loss and David DiVincenzo [10]. A significant advantage of using such a system is that semiconductor technologies offer great scalability for increasing the number of qubits.

2. BACKGROUND KNOWLEDGE AND LITERATURE REVIEW

Several material platforms have been implemented to create reliable QDs for spin manipulation, with pioneering work done in GaAs/aluminium gallium arsenide (AlGaAs) heterostructures. That work has demonstrated reading and controlling a singlet-triplet qubit [11]. Recently, silicon MOS, silicon/silicon-germanium (Si/SiGe) heterostructures and silicon nanowire architectures have also achieved spin manipulation and relevant quantum information processing.

2.2.1 GaAs/AlGaAs Heterostructures

GaAs is a III/V material that provides excellent electron mobility. An operable QD in GaAs is relatively larger than in silicon as it has a lower effective mass, and hence the QDs are easier to be confined and have less disorder because of the lower interface roughness. The direct-band property of GaAs also eliminates the perturbation from valley states, which makes both the experiment and analysis simpler compared to indirect-band-gap material.

One of the first GaAs/AlGaAs QDs was fabricated using a vertical island architecture. The isolated GaAs island can be seen as a QD, while the top and bottom substrates act as source and drain, see Figure 2.4. The gap between the dot and the source-drain contacts is formed by AlGaAs, creating isolating barriers that allow electrons to tunnel in and out of the dot. The charging energy of such QDs has been studied [48] to confirm that the desired quantum states have been produced. A comprehensive review of vertical GaAs QDs can be found in Kouwenhoven *et al.* [49].

While vertical QDs are less flexible in the fabrication process and gate control, laterally defined dots in GaAs/AlGaAs allow metallic gates to be patterned, and offer greater gate tunability and dot confinement. These depletion gates isolate

2.2 Quantum Dot Structures in Other Material Systems

the electron 2DEG channels and the QD; they can also control the barrier transparency between the dot and the channels. The ease with which the gates can be placed onto the device makes it extendable and scalable, including fabricating multiple dots near each other or integrating quantum point contacts (QPCs) as charge sensors to count the number of electrons in the dot. Charge sensing has been demonstrated by detecting electron occupancy in single and multiple QDs [50, 51, 52, 53, 54, 55].

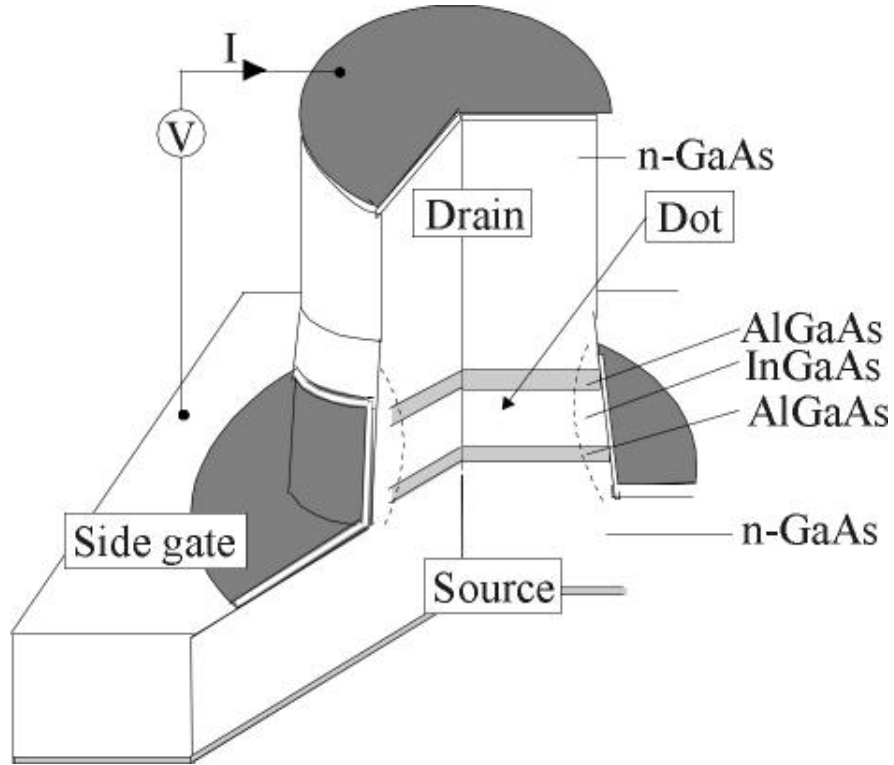


Figure 2.4: Vertical quantum dot - Schematic of a vertical GaAs/AlGaAs QD fabricated by Tarucha *et al.* [48]

GaAs/AlGaAs quantum-coherent experiments have demonstrated the process of obtaining Rabi oscillations on individually addressed QDs via integrated micromagnets [56, 57]. This is a significant step towards creating multiple qubits

2. BACKGROUND KNOWLEDGE AND LITERATURE REVIEW

on a scalable solid-state platform.

Similar GaAs QDs have also been used to implement charge-based qubits. Quantum operations on charged-based qubits have been demonstrated by Fujisawa *et al.* [58].

The pioneer platform for semiconductor-based quantum computation has been GaAs/AlGaAs heterostructures, and many other architectures have followed the experiments it has enabled. It is essential to understand these experiments comprehensively in order to build future silicon QDs.

2.2.2 Si/SiGe Heterostructures

Si/SiGe heterostructures have similar properties to GaAs/AlGaAs heterostructures. A significant issue when using III/V materials like GaAs is the hyperfine interaction between the electron spin and nuclear spins. Silicon is a group IV material, where its isotope ^{28}Si has zero nuclear spin. Spinless material-based substrates greatly enhances the coherence of electron spins in the QD, which is an essential requirement to store quantum information in the spin qubit.

Si/SiGe also offers relatively high electron mobility, approximately one or two orders of magnitude below GaAs/AlGaAs structures. Similarly to laterally defined GaAs/AlGaAs structures, gates are used to deplete and create barriers in the device [59]. Charge sensing and single-electron QDs in Si/SiGe architectures have been achieved [60, 61]; spin readout, lifetime measurements and coherent control have also been demonstrated [36, 62, 63, 64].

One drawback is that silicon does not have a direct bandgap, and has six degenerate band minima in k-space. However, with additional confinement, the valley degeneracies can be lifted. For [100] or [110] lattice configurations, the

2.2 Quantum Dot Structures in Other Material Systems

lowest valley states will be doubly degenerate at the silicon interface.

Experiments have been carried out to measure the valley-splitting energy between these two lowest valleys [65], and the valley splitting is also calculated to be less than 1 meV [66]. Goswami *et al.* showed that the valley splitting is controllable with lateral confinement and magnetic field [67]. Takashina *et al.* demonstrated valley polarisation with large splitting using a top-gate/bottom-gate structure [68].

2.2.3 Silicon Nanowires

Silicon nanowires can be reproduced with a diameter of only 36 nm using a controlled-growth technique [69]. The nanowire is confined in two dimensions, allowing a one-dimensional (1D) channel for electrons to flow. A QD can be defined in a more robust way compared to two-dimensional (2D) laterally defined gated dots, where only one axis-gate position is required. Transport measurements have demonstrated Coulomb blockade and spin filling in such dot [70].

While most research is focused on the spin of electrons, Zwanenburg *et al.* reported few-hole transport in a silicon nanowire dot and measured its spin-state [71]. The valence band in silicon has its band minimum centred at the Γ point; hence, holes are generally considered to have even longer spin lifetimes than electrons as a result of their single-valley state [72]. For clear observation of a single charge in nanowire QDs, a short channel length is desired to avoid the existence of impurities and defects in the wire.

2. BACKGROUND KNOWLEDGE AND LITERATURE REVIEW

2.2.4 Carbon Nanotubes

Carbon nanotubes are made by wrapping a plane of graphene, resulting in a cylindrical carbon nanostructure. Cobden *et al.* [73] demonstrated shell filling of electrons and holes. Electron-hole symmetry in carbon nanotubes is evident because of its high-purity structure. Jarillo-Herrero *et al.* observed nearly perfect symmetry [74], along with strong electron-electron interaction.

While carbon nanotubes offer almost perfect 1D channels, positioning the tubes on the substrate is not trivial. Hence, the scalability of carbon nanotubes would need to rely on more advanced fabrication techniques.

2.2.5 Graphene

In recent years, graphene monolayer structures have become an area of interest in semiconductors [75, 76, 77]. Graphene is a conducting material with high mobility, a special band structure [78], a low nuclear spin and a weak spin-orbit interaction [79, 80, 81]. This qualifies it as a QD base material. Despite its superior conductivity property, a few issues need to be solved in order to exploit it as a spin-based qubit. One major problem is graphene's band structure: it does not have a closed bandgap between the conduction and the valence band. Recent experiments have shown that Coulomb diamonds and relaxation times can be measured [82] in graphene QDs, via both transport current and integrated charge detection.

2.3 Silicon Device Physics

Silicon-based QDs are recognised as a promising system for the implementation of solid-state quantum computing [14, 19, 36, 63, 83]. While such devices are appealing because they can be engineered to show long coherence times [84, 85, 86], complications exist for the manipulation of quantum states that arise from the multi-valley conduction band present in bulk silicon [87]. In fact, valley degeneracy is typically lifted in nanodevices because of interfacial stress/strain and electrostatic confinement [88, 89].

Table 2.1 lists some important properties of intrinsic silicon crystal. Properties labelled with * are the values at room conditions ($T = 300$ K, $P = 1$ atm), and may vary in different conditions.

2.3.1 Silicon Band Structure

A silicon atom has the subshells $3s$ and $3p$ in its outer shell, with two electrons in each subshell. When a collection of silicon atoms are put together, these subshells begin to overlap with their neighbour atoms, causing the energy levels to be mixed. Figure 2.5 displays the way in which the energy levels are eventually separated into two main bands in the silicon crystal. There are $2N$ energy states available in the $3s$ subshell and $6N$ in the $3p$ subshell, where N is the total number of silicon atoms. When the wavefunction of the atoms begins to overlap, these states become mixed and the energy levels broaden. At one point, the two subshells' bands merge into a continuous band that contains $8N$ states. Finally the band separates again so that both the top (conduction) and bottom (valence) bands contain $4N$ states. The lattice spacing of the silicon crystal finds a stable

2. BACKGROUND KNOWLEDGE AND LITERATURE REVIEW

Atomic number	14
Electron configuration	$1s^2 2s^2 2p^6 3s^2 3p^2$
Isotopes	28(92%), 29, 30, 32(unstable)
Atoms per volume*	$5.0 \times 10^{22} \text{ cm}^{-3}$
Density*	2.328 g cm^{-3}
Crystal structure	diamond cubic
Lattice constant*	5.431 \AA
Thermal conductivity*	$1.5 \text{ W cm}^{-1} \text{ K}^{-1}$
Melting point*	1687 K
Boiling point*	3538 K
Band gap*	1.12 eV
Conduction band minima	6
Valence band maxima	2
Effective density of states in conduction band	$2.8 \times 10^{19} \text{ cm}^{-3}$
Effective density of states in valence band	$1.08 \times 10^{19} \text{ cm}^{-3}$
Electron mobility*	$1500 \text{ cm}^2 \text{ V}^{-1} \text{ s}^{-1}$
Hole mobility*	$475 \text{ cm}^2 \text{ V}^{-1} \text{ s}^{-1}$
Electrical resistivity*	$2.3 \times 10^5 \text{ } \Omega \text{ cm}$
Dielectric Constant	11.9
Magnetic ordering	diamagnetic
gyromagnetic ratio	2

Table 2.1: Silicon properties.

2.3 Silicon Device Physics

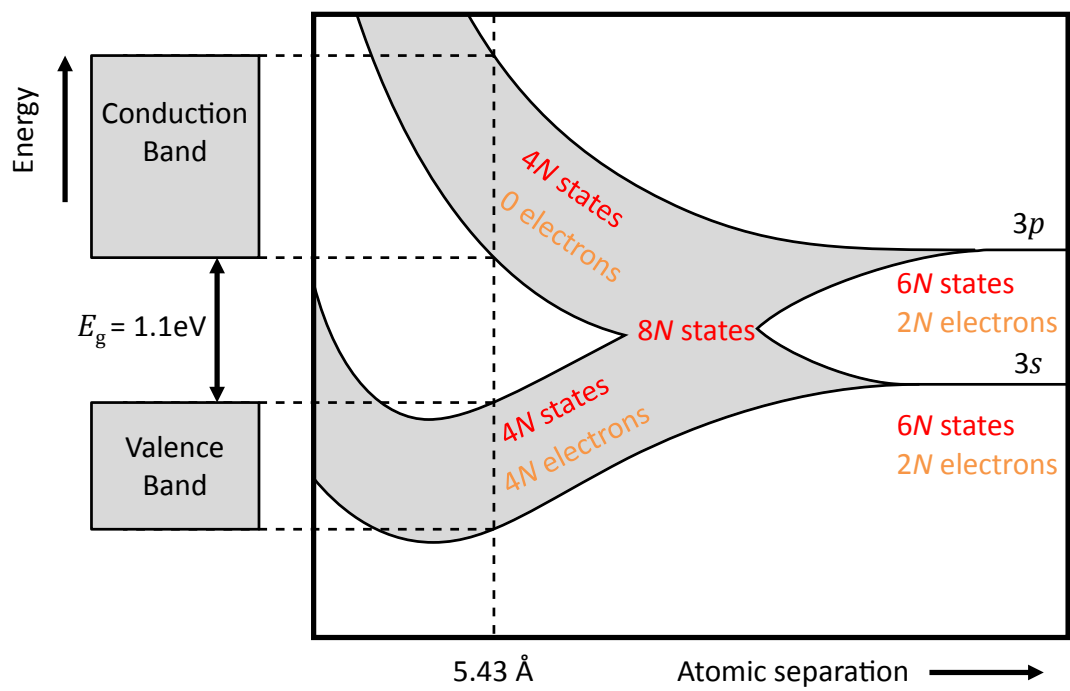


Figure 2.5: Energy levels in silicon - Energy band of silicon crystal. An initial 3s and 3p orbitals in a single atom are transformed into a conduction band and valence band with $4N$ electrons each when the lattice separation closes.

2. BACKGROUND KNOWLEDGE AND LITERATURE REVIEW

point at 5.43 \AA , where it has $4N$ states in the valence band (which is completely filled with electrons) and $4N$ states in the conduction band (with no electrons under neutral conditions).

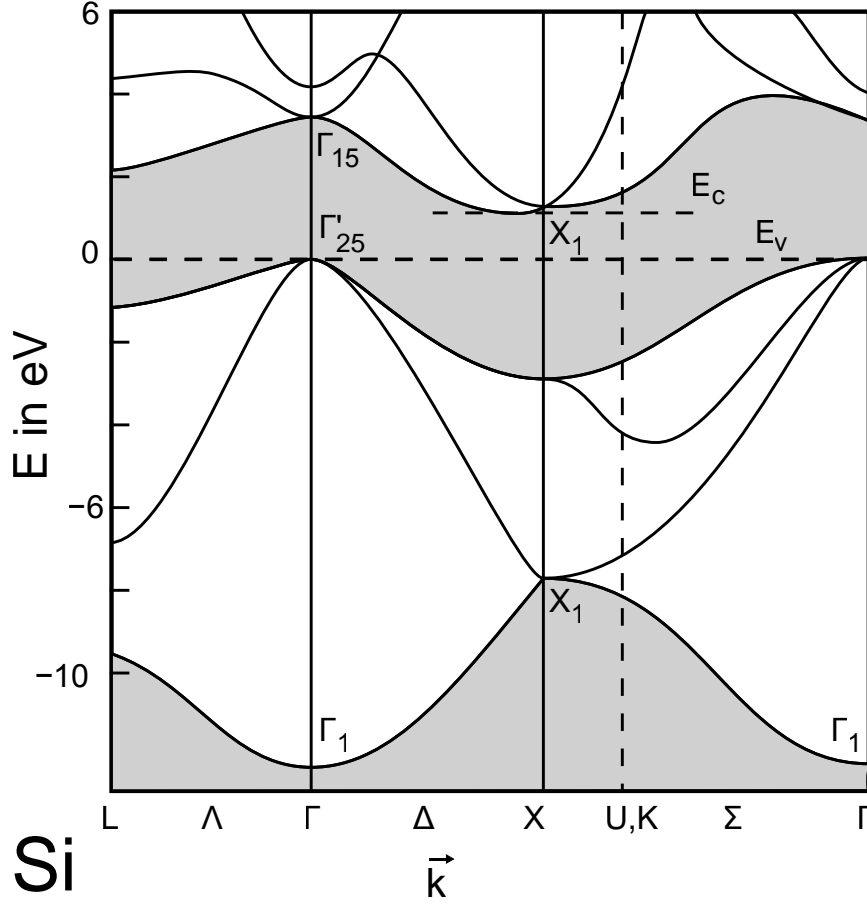


Figure 2.6: Band structure of bulk silicon in k-space - Conduction band minima, E_C and valence band maxima, E_V , are shown at Γ_{25} and near X_1 point respectively. Source: Chelikowsky *et al.* [90]

Silicon is known to be an indirect bandgap material. The conduction band minima and the valence band maxima do not lie at the same momentum in k-space, see Figure 2.6. The recombination of electrons and holes requires an extra momentum, which absorbs (emits) phonons from (into) the silicon crystal. This

2.3 Silicon Device Physics

property means that silicon is not an ideal material for light-emitting diodes.

2. BACKGROUND KNOWLEDGE AND LITERATURE REVIEW

2.3.2 Silicon-based MOS Devices

By stacking layers of metal, oxide and semiconductor (MOS), a 2D conducting plane can be created at the oxide-semiconductor interface by varying the metal potential. MOS technologies are widely used in today's semiconductor industry. Silicon MOS field effect transistors (MOSFETs) are also the dominant devices for building integrated circuits.

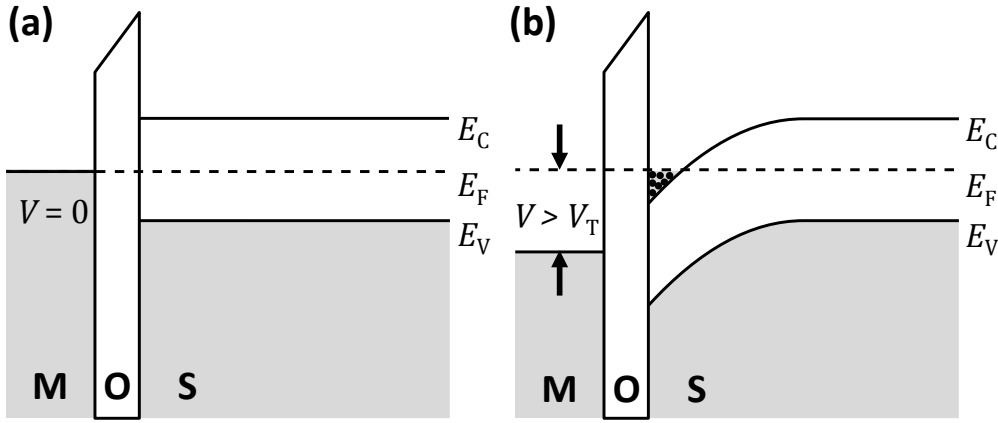


Figure 2.7: Band diagram of MOS device - (a) The metal gate potential is aligned with the Fermi level, with no electrons in the conduction bands (above E_C). (b) When the gate potential exceeds a certain threshold voltage V_T , E_C near the interface is pulled below the Fermi level E_F and electrons are accumulated in the conduction band.

Figure 2.7 is a band diagram of a typical MOS device. Assuming the temperature is 0 K, electrons can only exist above the Fermi level, E_F . When the metallic gate potential is set to 0 and aligned with the Fermi level of the semiconductor, electrons fill the valence band and no electron can exist in the conduction band, as shown in Figure 2.7 (a). By applying a positive voltage to the gate, the band structure near the interface between the oxide and semiconductor is tilted. At a certain voltage, the conduction band is tilted strongly, until E_C is below E_F , as

2.3 Silicon Device Physics

shown in Figure 2.7 (b). In this situation, the electrons have enough energy to fill the empty states near the interface, and they can move freely in the x and y directions, forming a thin conducting layer. The voltage required to accumulate electrons in the conduction band is called the threshold voltage, V_T . The value of V_T depends on the physical conditions of the MOS, including oxide thickness, oxide quality, trap charges, substrate doping density and work function of the metallic gate.

The electron-filled conducting layer is often referred to as a ‘2DEG’ (two-dimensional electron gas). The metal of the MOS device can be patterned to create different shapes of 2DEG, including small quantum wells. In this thesis, all structures are MOS devices with aluminium (Al) as the metal, and silicon dioxide (SiO_2) as the oxide. Section 3.1 demonstrates the advantages of such materials for fabricating artificial QDs using MOS technologies. Similar silicon MOS-based structures have also been realised using global top and back gates [91, 92, 93].

2.3.3 Conduction-band Valleys in Silicon

A bulk silicon crystal has a six-fold degeneracy in the conduction band, located at the six X-points in the Brillouin zone (Δ valleys), and a two-fold degeneracy in the valence band at the Γ point (heavy holes and light holes), see Figure 2.6 and 2.8 (a).

When the silicon crystal is confined in one direction, the degeneracy of the valleys is lifted. In a typical silicon MOS device, which relies on operating the 2DEG at the interface between the silicon and the oxide, the z-direction valleys (perpendicular to the interface) are brought down to the Γ point. This creates two degenerate Γ valley eigenstates that have a lower energy compared to the

2. BACKGROUND KNOWLEDGE AND LITERATURE REVIEW

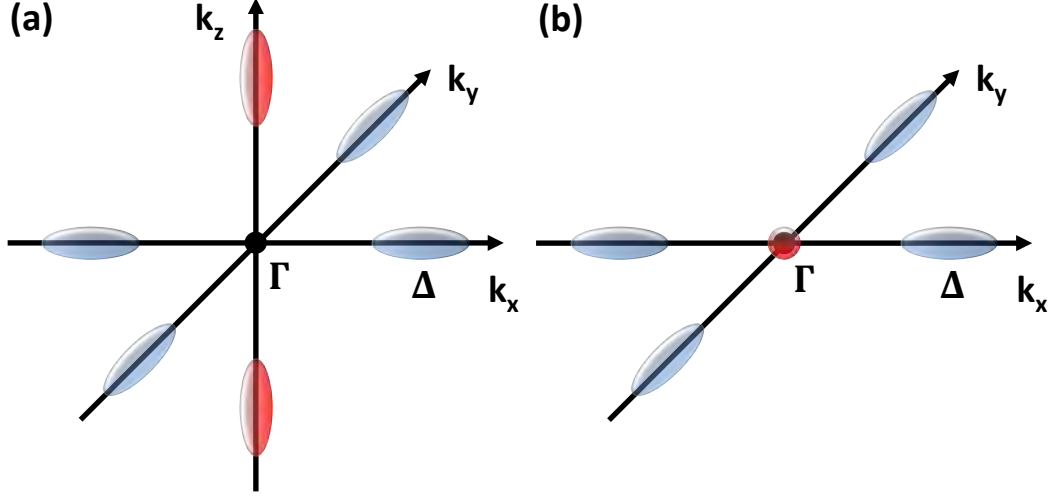


Figure 2.8: Valley composition in silicon - (a) Six degenerated valleys illustrated in k -space, located on the Δ axes in all six directions. (b) Along the z -interface, the two valleys on k_z are pushed onto the Γ point, lifting the valley degeneracy.

original x - and y -direction Δ valleys, as shown in Figure 2.8 (b). The eigenstates can be expressed as:

$$E_{V+,V-} = \frac{1}{\sqrt{2}}(k_{z+} \pm e^{i\theta} k_{z-}) \quad (2.8)$$

Where θ is the valley phase that can differ in QDs and changes the way how QDs couple to each other [94, 95].

In a silicon MOS QD in the few-electron regime, electrons fill the two Γ valleys because the energy is not sufficient to reach the higher valleys, which have energies around 30 meV above the ground state [66].

With the presence of a vertical electric or magnetic field, the two Γ valleys' eigenstates can be separated further. This energy difference is caused by the narrow wavefunction envelope in the z -direction, see Figure 2.14 (b). This energy is referred to as the valley-splitting energy ΔE_{VS} in a silicon QD.

2.4 Silicon Quantum Dot Physics

2.4.1 Electron Confinement in a Quantum Dot

Unlike atoms and molecules, which have strong confinement from the nucleus to trap charges, QDs rely on material boundaries or external electric fields to create an artificial band level confined in all three spatial dimensions. In an MOS-type QD, electron motion in the z-direction is confined by the oxide-semiconductor interface, and motion in the x,y-direction is laterally confined by the metallic gates' potential. This QD behaves more like a 2D quantum well because the z-direction is tightly bound.

Quantum-state initialisation and readout often requires loading and unloading electrons to/from the QD, such as spin readout relying on spin-to-charge conversion. Tunnel coupling the QD to a 2DEG reservoir allows the electron occupancy to be tunable in the QD, while maintaining the conduction band level between them above the Fermi level, where this region is referred to as the 'barrier'. Even though the barrier forbids classical particle movement from the reservoir to the QD, quantum tunnelling can still occur if the barrier is transparent enough. The tunnel rate (that is, how quickly an electron can move through this barrier) depends on the width and band-energy level of the barrier; increasing these two properties decreases the tunnel rate exponentially.

The second condition necessary for quantum tunnelling to occur is the existence of a quantum state in the QD with an energy level equal to or below the 2DEG Fermi level. The quantum state in the small confined QD is quantised, meaning that electrons can only exist at certain energy levels. Thus, to load an additional electron into the QD, both the Coulomb charging energy (E_C) and the

2. BACKGROUND KNOWLEDGE AND LITERATURE REVIEW

quantum confinement energy (ΔE) must be overcome.

2.4.2 Coulomb Blockade

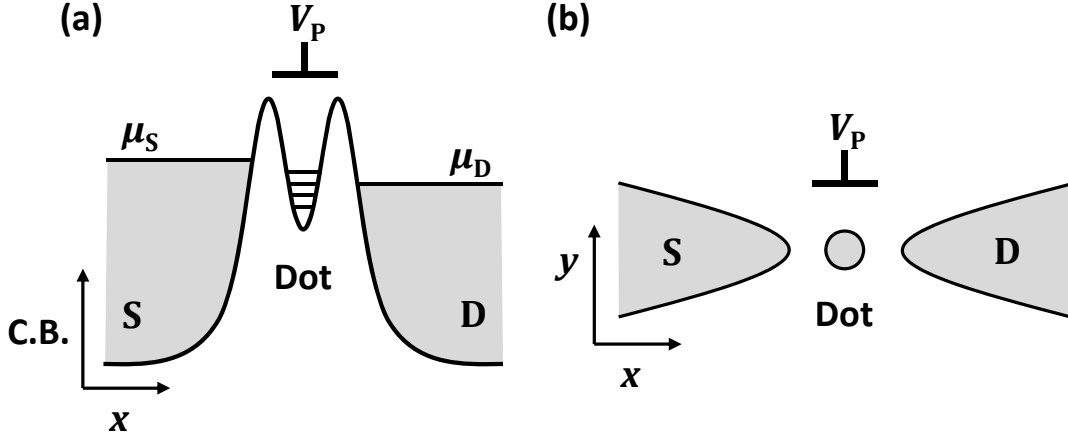


Figure 2.9: Schematic of a single QD - (a) Conduction band profile of a single QD, with connected source-drain bias. (b) Top view of the source-drain reservoir and the QD.

Figure 2.9 shows a QD connected to two 2DEG reservoirs from two sides. The electron reservoirs can be connected to ohmic contacts and become both the source and the drain in the MOSFET device. Applying a source-drain bias allows electrons to flow through the QD and produce a current.

As described in Section 2.4.1, electrons can only tunnel into the QD when an appropriate state is available, in terms of both quantum mechanics and energy conservation. The term ‘Coulomb blockade’ describes these regions where electrons are forbidden to travel through the QD. With a change in the QD potential via a plunger gate (V_P), the current is usually blocked, except at periodic Coulomb peaks, as shown in Figure 2.10 (a). A special current dependency on V_P and source-drain bias (V_{SD}) is shown in Figure 2.10 (b). Electron

2.4 Silicon Quantum Dot Physics

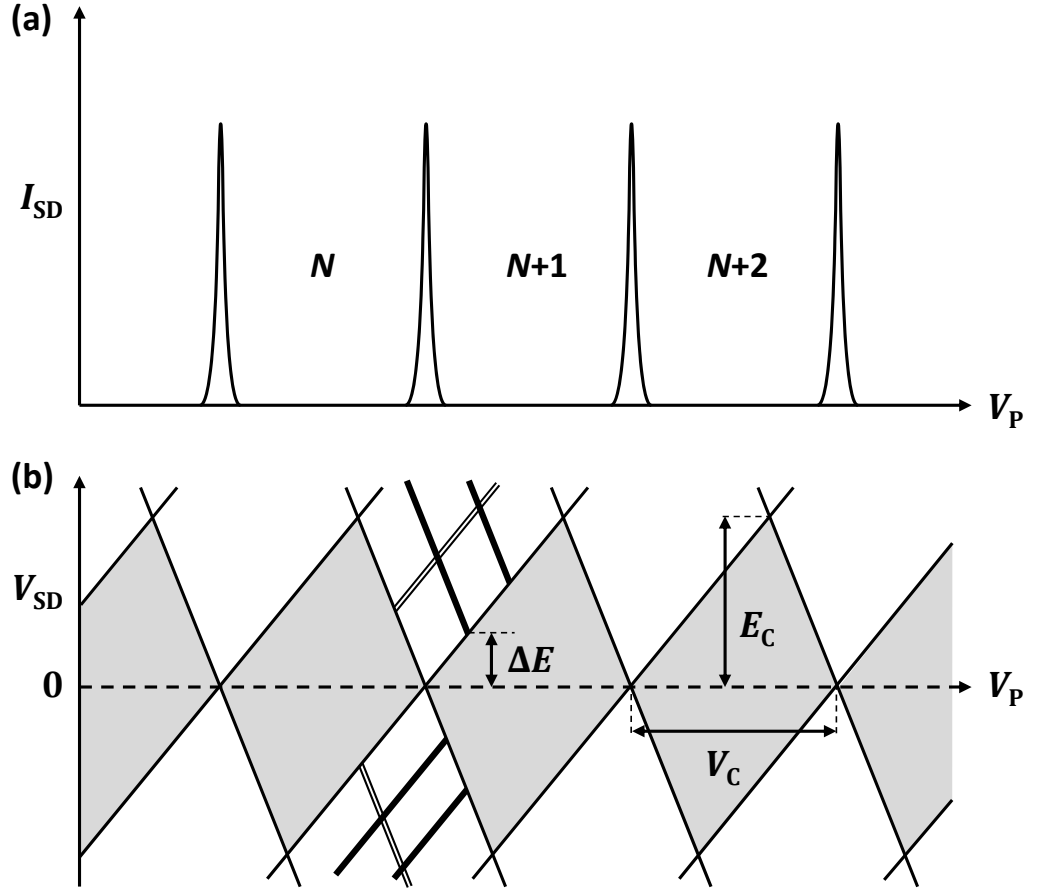


Figure 2.10: Transport current Coulomb peaks and diamonds in a single QD - (a) Transport current against V_P - Coulomb peaks occurs when the QD electrochemical potential sits between the source-drain Fermi level. (b) Stability diagram with V_{SD} against V_P , showing how Coulomb diamonds are formed with the Coulomb blockaded regime. Excited states create current resonance outside the diamonds.

2. BACKGROUND KNOWLEDGE AND LITERATURE REVIEW

currents are Coulomb blocked in continuous diamond-shaped regions referred to as ‘Coulomb diamonds’.

This type of device, where currents can flow only when the QD potential is sitting on a Coulomb peak, is referred to as a ‘single-electron transistor’ (SET). the SET is the main device structure used throughout this thesis, including the single-dot devices (Chapter 4 and 5) and charge detectors (Chapter 5, 6 and 7).

2.4.3 Single Electron Transport through a Quantum Dot

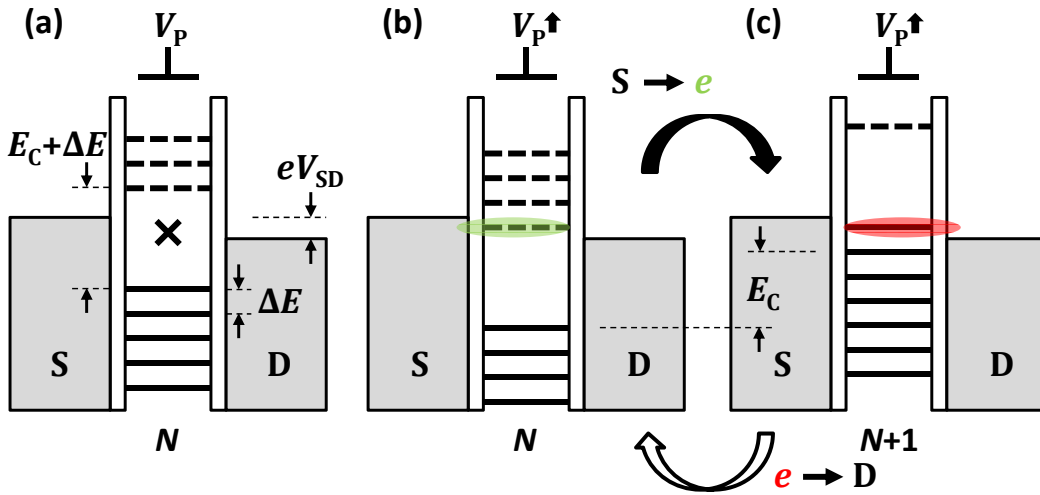


Figure 2.11: Transport through a single QD - (a) The potential configuration of a Coulomb blockade regime - there is no possibility for an additional electron to move in or out of the QD. (b) An electron state between the source-drain Fermi levels μ_S and μ_D is available for an electron to tunnel in from the source, shown by the green ellipse. (c) The potential configuration after the electron tunnels into the QD. The electron is now available to tunnel to the drain, shown by the red ellipse. Afterwards, the QD potential returns to (b).

This section describes how electrons tunnel through a QD at zero temperature [96]. Figure 2.11 (a) is the energy configuration in the Coulomb blockade regime. In order to load an additional electron in the QD, additional energies E_C and ΔE

2.4 Silicon Quantum Dot Physics

are required, as described in section 2.4.1. The available potential is higher than the electrochemical potential of the QD, $\mu(N)$ by the addition energy $\mu(N+1) - \mu(N) = E_C + \Delta E$, and is also higher than the Fermi level of the 2DEG, $\mu(N+1) > \mu_S, \mu_D$. Hence, there is no electron in the 2DEG permitted to tunnel into the QD.

If the potential V_P is increased, $\mu(N)$ decreases, as shown in Figure 2.11 (b). The available potential is now lower than the source Fermi level, $\mu(N+1) < \mu_S$, and an electron is able to tunnel from the source to the QD, as described by the green ellipse. When the electron tunnels into the QD, the Coulomb field brings all the preoccupied electrons' energies up by E_C only, as shown in Figure 2.11 (c), and the electron number from N to $N+1$. The new electrochemical potential, $\mu(N+1)$, of the QD is now replaced by the preloaded available potential level, but remains higher than the drain Fermi level, $\mu(N+1) > \mu_D$. Hence, an electron can again tunnel from the QD to the drain, described by the red ellipse, and return to the Figure 2.11 (b) state, restoring the previous QD electrochemical potential and reverting to N electrons. By repeating the process in Figure 2.11 (b, c), a current is produced via electron tunnelling through the QD, while the available state in Figure 2.11 (b) sits within the source-drain bias window, eV_{SD} , so that $\mu_S > \mu(N+1) > \mu_D$.

If more than one available energy level exists in the source-drain bias window, $\mu_S > \mu(N+1), \mu(N+1) + n\Delta E > \mu_D$, electrons can also tunnel through these excited states, where their energies are $n\Delta E$ higher than the ground state ($n \in \mathbb{N}$, assuming ΔE is uniform for all N electron occupied). Figure 2.12 shows two different methods of tunnelling through the QD via the excited state. In Figure 2.12 (a) the excited state exists where $\mu_S > \mu(N+1) + \Delta E > \mu_D$, and

2. BACKGROUND KNOWLEDGE AND LITERATURE REVIEW

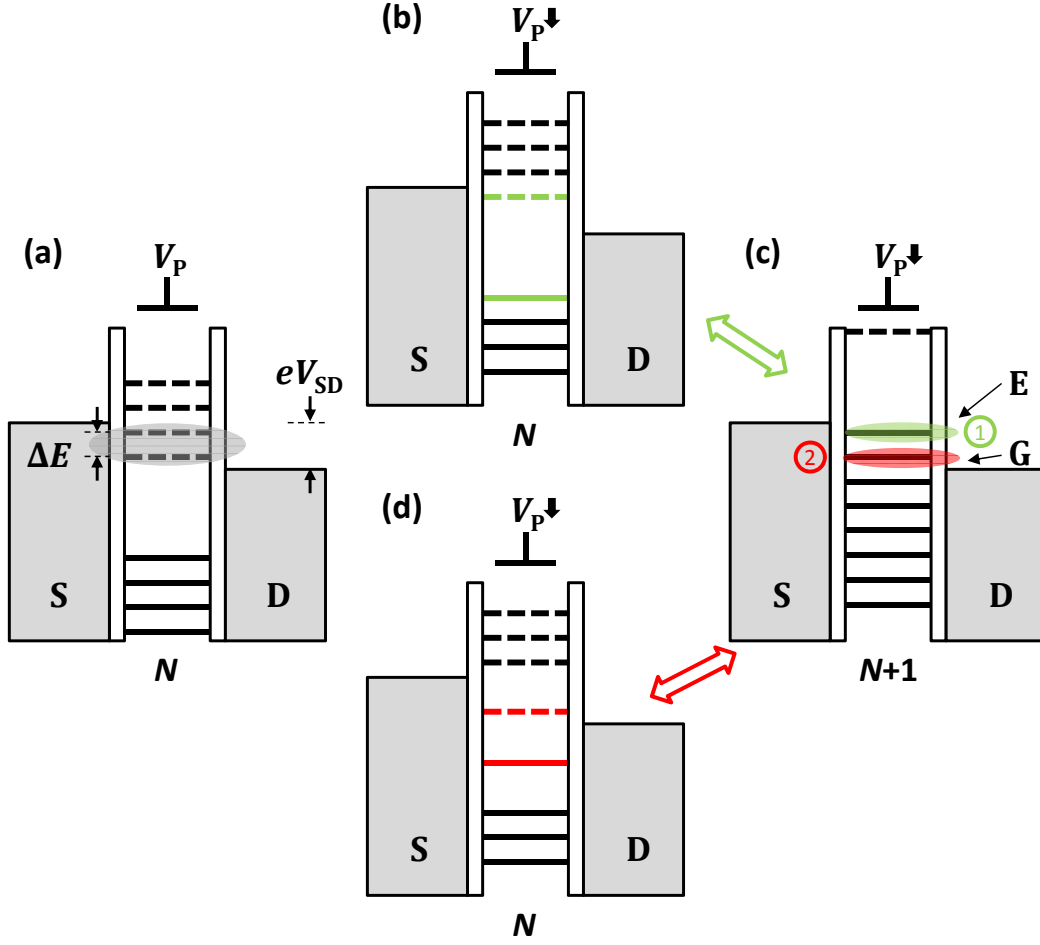


Figure 2.12: Transport through a single QD with excited states - (a) Two states are available for the additional electron to tunnel through. (b,d) An alternative method of tunnelling through excited states, with V_P lowered. In (c), if scenario 1 occurs (green ellipse), the potential levels will become (b), but if scenario 2 occurs (red ellipse), the potential levels will become (d). Both (b, d) will return to (c) once an electron tunnels back to the QD from the source.

2.4 Silicon Quantum Dot Physics

the electron can simply choose one of the two states to tunnel through. This excited-state tunnelling path corresponds to the solid lines shown in Figure 2.10 (b), with the quantum states being above the $\mu(N + 1)$ ground state.

The alternative method of tunnelling through the QD is shown in Figure 2.12 (b, c, d). In Figure 2.12 (b), there is only one ground state available for an electron to move from the source to QD. Figure 2.12 (c) shows that, once the electron tunnels in, two electrons exist with a potential higher than the drain, $\mu(N + 1), \mu(N + 1) - \Delta E > \mu_D$. Assume the electron at $\mu(N + 1)$ tunnels out to the drain from the green ellipse, the configuration returns to Figure 2.12 (b). In contrast, if the electron at $\mu(N + 1) - \Delta E$ tunnels out first (from the red ellipse), the configuration becomes Figure 2.12 (d). Depending on which scenario occurs in Figure 2.12 (c), the potential configuration is shown by either Figure 2.12 (b) or (d), which then returns to Figure 2.12 (c). These tunnelling paths correspond to the double lines shown in Figure 2.10 (b), in which the preoccupied quantum states are below the $\mu(N + 1)$ ground state.

2.4.4 Pulsed-Gate Spectroscopy Measurements

While electron transport through a QD can reveal the electron occupancy and quantum states of the QD (Figure 2.10), an alternative way to probe the QD is to use a nearby charge detector, without relying on transport current running through the QD. A charge detector has a sensitive transconductance region so that a nearby single-electron charge movement can affect its current. By monitoring the charge-detector transport current, the change of electron occupancy of the QD can be determined.

By applying a two-level pulse, it is possible to shuffle an electron in and out

2. BACKGROUND KNOWLEDGE AND LITERATURE REVIEW

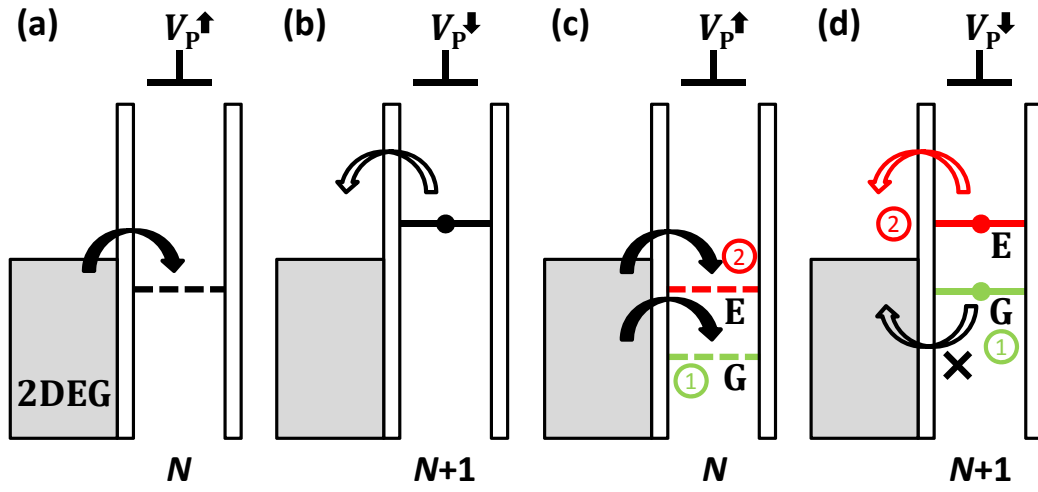


Figure 2.13: Energy-selective tunnelling from reservoir - (a) An electron can be loaded into the QD when its energy is below the Fermi level, while V_P increases. (b) An electron can be unloaded when its energy is above the Fermi level, while V_P decreases. (c) An electron can be loaded into either the ground state (scenario 1) or the excited state (scenario 2). (d) If the electron is loaded into the ground state (scenario 1 in (c)), while V_P decreases, its energy is still below the Fermi level and it cannot tunnel out. In scenario 2, the excited-state electron can tunnel out from the QD

2.4 Silicon Quantum Dot Physics

of a QD, as shown in Figure 2.13 (a, b). When the pulse on V_P is high, an electron can jump into the QD, causing a current change in the nearby charge detector (Figure 2.13 (a)); at the low-level pulse, an electron hops off the QD and the charge detector returns to the original current level (Figure 2.13 (b)). This two-level pulsing measurement can be used to find the electron transitions in the QD and the tunnel rate of the QD.

The excited states of the QD could also be measured using this technique. In Figure 2.13 (c), once the ground state is predetermined, the pulse level on V_P can be increased, allowing more available states sitting below the Fermi level. The electron could choose to tunnel into the ground state (green), or into an excited state (red). Now, if V_P is pulsed until the excited state is above the Fermi level but the ground state is still below it, the tunnelled-in electron could only hop out at the excited state (green). By using multilevel pulsing on the plunger gate, the quantum states of individual electrons can be distinguished, enabling reading of a single-electron spin. The lifetime of the excited state can also be extracted via this technique by varying the pulse-time width.

In Chapters 6 and 7, the applications of such a pulsing technique are discussed in more detail.

2.4.5 Quantum Dot Excited States

An excited state has a higher energy compared to the ground state, which has the lowest energy in an isolated system. While a 2D QD can be thought of as particles in a 2D box, the trivial excited states are the orbital levels that have different wavefunctions. In Figure 2.14 (c), the red quantum state can be seen as the third harmonic eigenstate, which generally has higher energy than the green

2. BACKGROUND KNOWLEDGE AND LITERATURE REVIEW

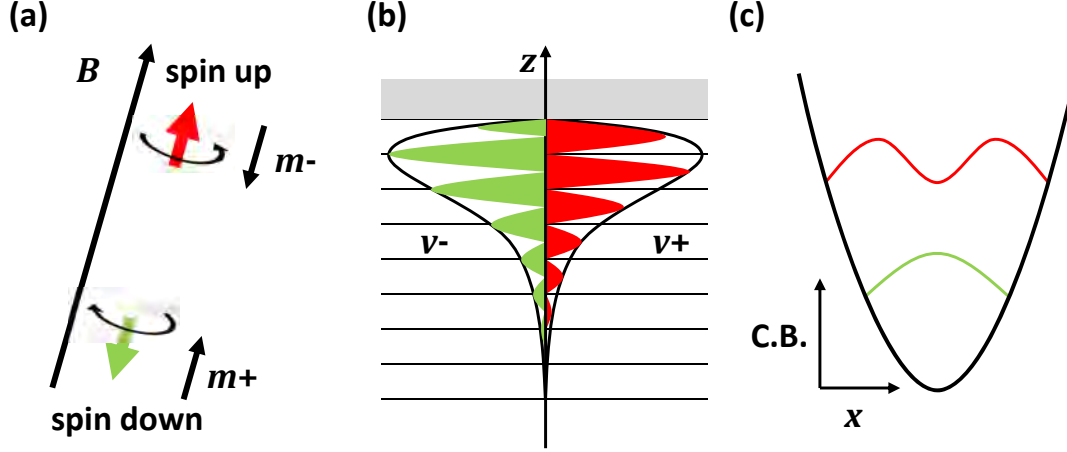


Figure 2.14: Origin of excited states in a QD - (a) Zeeman splitting of spins, within a magnetic field. (b) Valley splitting from lattice spacing and altered wave function under the same envelope. (c) Traditional orbital energies of the conduction band energy.

state (first harmonic). The orbital states are often related to the size of the QD: as the size increases, the orbital separation decreases (see Figure 2.15).

In a silicon QD that contains electrons as particles, the possible quantum states are more than the orbital levels alone. The spin of an electron has two states: spin-up and spin-down. These spin states are degenerate when no external magnetic field exists, and the energy separation varies linearly with the magnetic field (see Figure 2.14 (a)). Spin states are the core information in a spin-based quantum computation system, and also the main properties being measured and studied throughout this thesis.

Figure 2.15 (a) demonstrates how the spin of an electron reacts with an external magnetic field, \vec{B} . As bulk silicon has a g -factor greater than 0 ($g = 2$), a spin-up electron gains an extra Zeeman energy, $\Delta E_Z = g\mu_B|\vec{B}|$, while it has a magnetic moment antiparallel to \vec{B} . The energy of the spin-down electron de-

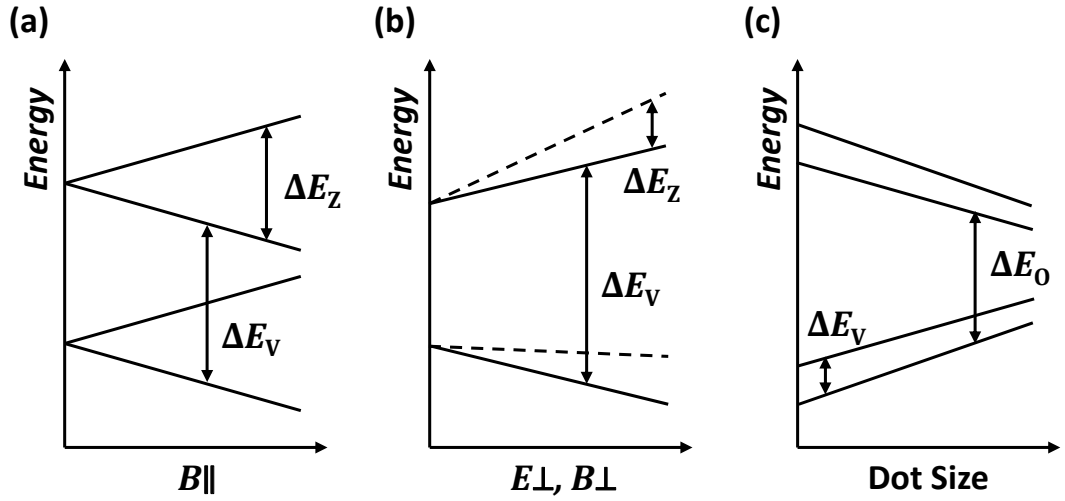


Figure 2.15: Change of excited-state energies under changing conditions
- (a) An in-plane magnetic field causes Zeeman-splitting energy $\Delta E_Z = g\mu_B B$.
(b) Varying the envelope wavefunction with perpendicular electric and magnetic fields causes a change in valley-splitting energy ΔE_{VS} . Additional Zeeman-splitting is introduced using a magnetic field.
(c) Changing the QD size with any lateral confinement or electron occupancy affects the orbital excited-state energy ΔE_O , as well as the valley-splitting energy, as a result of the change in the wavefunction envelope.

2. BACKGROUND KNOWLEDGE AND LITERATURE REVIEW

creases, $\Delta E_Z = g\mu_B|\vec{B}|$, and has its magnetic moment parallel to \vec{B} . Notice that the electron-spin direction is opposite to the magnetic moment, as electrons are negatively charged. The g -factor could be a different value, or even a negative value, using different materials - for example, bulk GaAs has a typical g -factor = 0.44.

The third class of excited states in a silicon QD is the valley eigenstates. As described in Section 2.3.3, there are two degenerate Γ valley eigenstates that have much lower energies compared to the other Δ valley states. Figure 2.14 (b) shows that the two-valley eigenstates' wavefunctions are out of phase with respect to the z -direction lattice spacing: the green and red wavefunctions have the same envelope but accumulate different integrated volumes. The valley-splitting energy between these two states can vary with the z -direction electric or magnetic field because the envelope of the wavefunction in z -direction varies, as shown in Figure 2.15 (The magnetic field also varies the Zeeman-splitting energy.)

In Chapter 6, we discuss how these three types of quantum excited states can be identified with both electric- and magnetic-field manipulation.

Chapter 3

Experimental Methods

This chapter provides an overview of the fabrication and experimental methods used. A list of equipment and fabrication recipes, and details on how to pattern the silicon MOS QD devices, is also presented. The basic techniques and instruments required to perform experiments under cryogenic condition are given.

The devices were fabricated within the Australian National Fabrication Facility (ANFF) at the University of New South Wales (UNSW), and the measurements were performed in the National Magnet Laboratory (NML) at UNSW.

3. EXPERIMENTAL METHODS

3.1 Device Fabrication

3.1.1 Optical Patterning of Ohmic Contacts and Oxide Growth

The silicon substrate is prepared in the microfabrication laboratory, with lightly *n*-doped phosphorus (resistivity $> 10 \text{ k}\Omega \text{ cm}$). The field oxide is grown in a single-walled furnace using a wet oxidation process. An oxide thickness of 200 nm can be grown at 1000 °C. The gate oxide is grown in an ultra-dry triple-walled furnace. In order to grow high-quality gate oxide, dichloroethylene (DCE) is introduced during the process. A gate oxide thickness of 5 nm is grown at 800 °C.

The ohmic contacts are heavily doped with phosphorus at a concentration of 10^{20} cm^{-3} . Phosphorus is predoped at 950 °C for 30 minutes. This is followed by a deglaze process carried out to remove the excess unreacted dopant glass using a hydrofluoric acid (HF) etch. Channel stoppers to prevent source-drain leakage are also implemented within the chip, where they are doped with boron. The doping patterns are conducted via photolithography using chromium masks exposed under ultraviolet (UV) light. The resolution supported by the photolithography is $1.5 \text{ }\mu\text{m}$.

3.1.2 Electron Beam Lithography of Gates and Alignment Markers

The main electron beam lithography (EBL) machine used for fabricating the devices in this thesis is FEI XL30. It was used to both write and image the nanostructures. The patterning software programs used are DesignCAD and Nanometer Pattern Generation System (NPGS). DesignCAD provided the main

3.1 Device Fabrication

environment for drawing gate patterns and alignment markers, and NPGS provided additional support for patterning parameters such as drawing sequences, drawing directions and area dose, and controlling the EBL writing process. The EBL system allows a minimum gate width of 20 nm.

Polymethyl-methacrylate (PMMA) resists are used for patterning. For standard gates, PMMA A4 is spun onto the wafer at 7500 rpm for 30 seconds, resulting in a 150 nm resist thickness. For gates that are required to cross over other gates (typically plunger gates), PMMA A5 is spun at 5000 rpm for 30 seconds, resulting in a 280 nm resist thickness. The resists are baked for 90 seconds at 180 °C.

An electron-beam energy of 15-30 kV is used for writing the patterns. A dosage of 500-650 $\mu\text{C cm}^{-2}$ is used for nanoscale gate structures, and 400 $\mu\text{C cm}^{-2}$ is used for fan-out bond pads. Alignment marks are used for multilayer gate alignment; they are coated with titanium before the gate patterning. Each device is manually aligned with the XL30 machine, ensuring that the nanostructures are aligned properly even with flawed (partially missing or difficult to detect with the beam) alignment markers.

The development process is performed in a solution of 1:3 methy-isobutyl-ketone (MIBK): Isopropyl alcohol (IPA) for 20 seconds, followed by a 20-second IPA rinse and nitrogen gas blowdry. The sample is then put into a Lesker thermal electron-beam evaporator. The aluminium gates are deposited at a rate $\sim 5 \text{ \AA s}^{-1}$ at a pressure $\leq 5 \times 10^{-6}$ torr. Finally, the metal lift-off process is performed in NMP solvent (1-methyl-2-pyrrolidone) at 80 °C for a few hours, followed by 10 seconds of ultrasonic agitation.

An additional short oxygen plasma-ashing process (3 minutes) under low pressure (110 mTorr) is used to remove organic residues (mainly the PMMA) left

3. EXPERIMENTAL METHODS

behind on the chip surface.

3.1.3 Annealing and Packaging

To terminate the dangling bonds and charge traps between the silicon and SiO_2 interface of the chip, forming gas annealing is performed. The chip is loaded into a furnace preset to 400 °C for 15 minutes. The forming gas consists of 95% nitrogen gas (N_2) and 5% hydrogen gas (H_2). The annealing process also improves performance of ohmic resistance and threshold voltage [14].

The fabrication of the devices on the chip is now complete. In order to mount the devices onto the measurement equipment, the devices are packaged in a standard 20-pin Charntec. Usually, the chip is diced into smaller pieces, each of which holds 2×2 or 3×2 devices, for ease of pin bonding.

The Kulicke & Soffa aluminium wedge bonder was used to bond the chip metallisation pads to the contacts of the Charntec. Not all the devices can be bonded with 20 pins at the same time; therefore, to measure the unbonded device, it is necessary to take off the bonds of the previous device. The packages are kept in a Gel-Pak conductive box to prevent electrostatic discharge before they are loaded into the measurement setup.

3.2 Design of Device Structures

In this thesis, all devices in the following chapters are fabricated with silicon MOS with multilayer $\text{Al-Al}_x\text{O}_y\text{-Al}$ gate stack. The original concept is presented in Angus et al., where a QD can be formed with two layers of aluminium gates. The main advantage of this structure is the potential of the QD barriers, and the fact that the reservoirs can be controlled independently, providing the ability

3.2 Design of Device Structures

to maintain the channel conductance and the barrier height while the QD sits within the few-electron regime [15].

3.2.1 Multi-layer Gate Structure

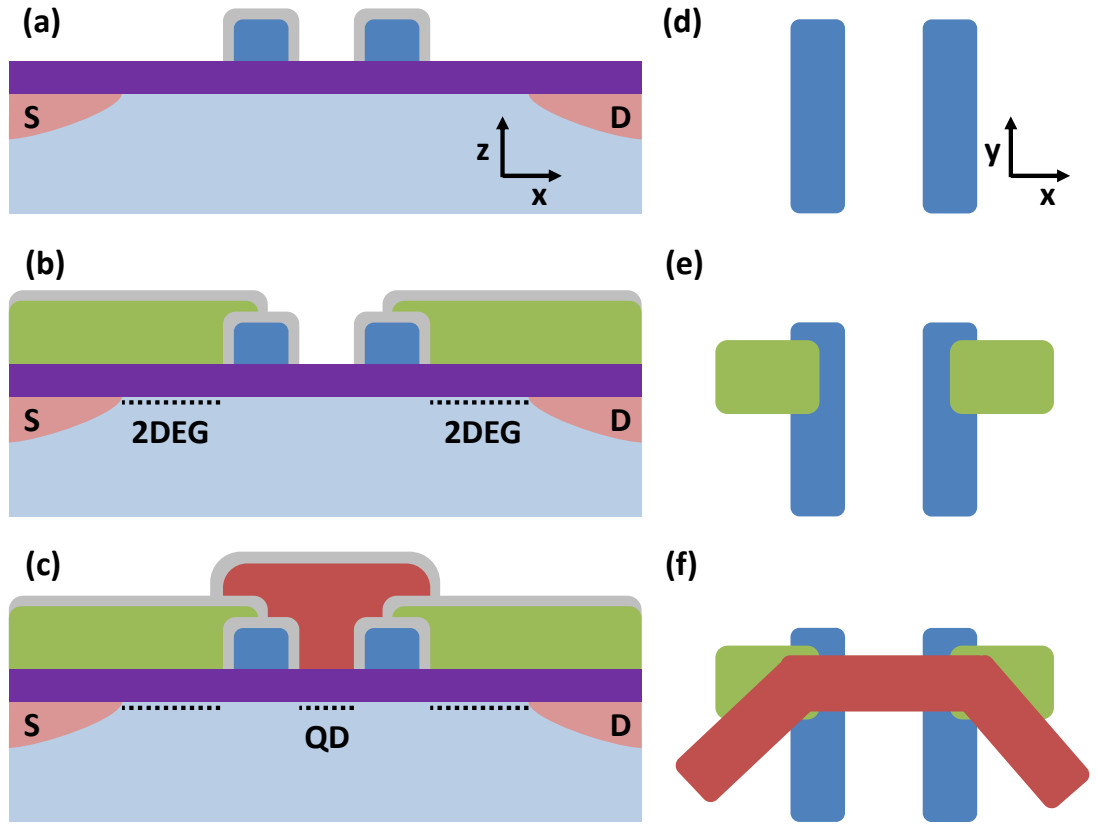


Figure 3.1: QD with triple-layer gate stack structure - Schematics of stacking up the triple-layers, cross-section and top views. (a, d) Barrier gates (blue) are placed as the first layer. (b, e) The lead gates (green) connect the source and drain all the way to the barrier gates, creating the 2DEG reservoir. (c, f) The plunger gate (red) is placed as the last layer, inducing an independently controlled QD.

To realise the QD described above, a triple-layer gate stack is required. The first layer of the aluminium gates is the barrier gates, as shown in Figure 3.1

3. EXPERIMENTAL METHODS

(a, d). The barrier gates typically operate at a lower potential than the plunger (controlling the QD potential) and the lead gates (inducing the 2DEG reservoir), or even at a negative potential if no electron tunnelling is required (see Chapters 6-7). One reason to place the barrier gates first is to obtain a lower pinch-off voltage. The height of the barrier gates is ~ 30 nm.

The second layer is the lead gates, connecting the ohmic contact channels all the way to the barrier gates (see Figure 3.1 (b, e)). If independent control of the QD is not required (for example, to realise a charge sensor), the lead gates can go over the barrier gates and connect the two channels. Before the second layer is fabricated, the device is put into an oven at 180°C for 10 minutes to ensure that a layer of Al_xO_y insulator exists between the two layers. The Al_xO_y grown is typically 4-5 nm extracted from XTEM [97], allowing up to ~ 4 V difference between the two layers before voltage breakdown. The height of the lead gates are ~ 40 to 70 nm - slightly higher than the barrier gates to ensure it is possible to cross over them.

The final layer is the plunger gates to control the QD potential. The same process is performed to grow the Al_xO_y (See Figure 3.1 (c, f)). In order to cross over the previous two layers of gates, the final layer is much higher - typically 70-120 nm (depending on the height of the previous layer).

With these three layers of aluminium gates, a fully electrostatically controllable QD device is fabricated. This architecture permits the last electron in Chapter 4 to be reached while maintaining a sufficient readable current through the QD.

3.2.2 Integrated SET Charge Sensor

An alternative way to count the number of electrons in a QD is to rely on a charge detector (see Chapter 5). A charge detector must be close to the QD in order to have the maximum capacitive coupling. In this silicon MOS structure, aluminium gates can only be defined laterally; hence, the charge sensor can only sit beside the QD laterally.

Figure 5.1 demonstrates how a SET charge sensor is fabricated next to the QD. The SET structure is very similar to the QD with two leads, except that the extra plunger gate is optional because entering the few-electron regime is not desired. The two barriers are placed first, followed by the top gate, which acts as both the plunger gate of the SET island and the lead gate to induce the 2DEG reservoir. The distance between the QD and island of the SET in the following chapters is 100-150 nm, a range that gives sufficient SET current signal to detect electron transitions in the main QD.

3.2.3 Extension to Multiple Dots and Qubits

By extending this architecture, we can fabricate a double QD device [97] using three barriers and two separated QD plunger gates. The devices described in Chapters 6 and 7 were planned to create a double QD system with charge sensor. The next stage is to perform coherent experiments, which may involve the integration of an ESR line to rotate the spin of an electron. The idea would be to place the ESR line at the empty left side of the device shown in Figure 7.1 to obtain a maximum magnetic field microwave acting on the QD, using a similar ESR design to that used by Pla *et al.* [20].

3. EXPERIMENTAL METHODS

3.3 Measurement

All the device measurements are performed under cryogenic conditions, where a 4 K liquid helium Dewar is used for device function pretesting, and a 20 mK base temperature dilution refrigerator with the least possible thermal noise is used for the main experiment.

3.3.1 4 K Dewar Measurements

The Charntecs onto which the devices are bonded is mounted on a dip rig and dipped into the 4 K liquid helium Dewar. The other end of the Dewar has Bayonet Neill-Concelman (BNC) connector pins that are terminated with ground connectors except during measurements, to protect the devices from electrostatic discharge. The major objective of using this 4 K Dewar is to do a leakage test, including gate to source-drain leakage, shorted gates and other possible defects of the device. The leakage test is performed using a source-measure unit (SMU) instrument, allowing the use of a current cap to protect the device from explosion. Basic turn-on and barrier-gate pinch-off measurements are also performed, to ensure that all the gates and QD characteristics behave normally.

The cryogenic phenomena of a QD are already visible at this temperature, such as oscillation of the source-drain current that represents Coulomb oscillations, and the ability to detect charge movements with a charge sensor using clever filtering techniques. Once the device performance is at an appropriate standard, the device is transferred to the dilution refrigerator for further experiments that require an even lower temperature.

3.3.2 Dilution Refrigerator Measurements

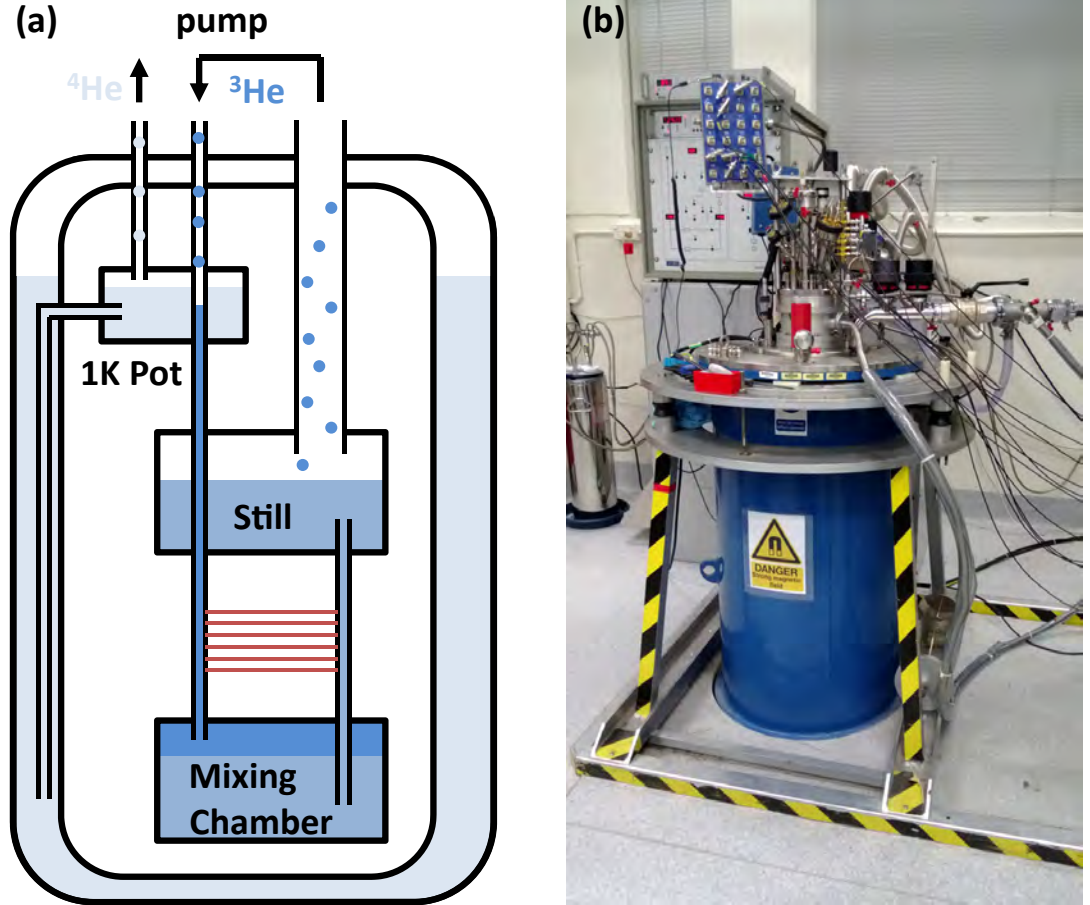


Figure 3.2: Dilution refrigerator - (a) Schematic of a dilution refrigerator, where the sample is attached beside the mixing chamber (red lines indicate heat exchange). (b) The Kelvinox K100 dilution refrigerator at NML with instruments attached.

The $^3\text{He}/^4\text{He}$ dilution refrigerator has the cooling power of $15\text{--}200\mu\text{W}$ to reach a base temperature as low as 20 mK. Figure 3.2 (a) shows a simple schematic of a dilution refrigerator. At $T = 0$, ^3He is lighter than ^4He hence the ^3He (pure phase) will float on top of the ^4He in the mixing chamber. The binding strength between two ^3He atoms is weaker than $^3\text{He}\text{--}^4\text{He}$, where ^3He tends to dissolve into

3. EXPERIMENTAL METHODS

the ^4He bath (diluted phase). At equilibrium, there will be around 6.4% of ^3He in the diluted phase. By heating the still where it contains the diluted ^3He , the equilibrium ^3He concentration is reduced to approximately 2% and the excess ^3He is vaporised. The pressure then causes the pure ^3He in the mixing chamber to migrate into the diluted phase; this process absorbs heat and is the main cooling mechanism that brings the mixing chamber down to mK range. An 1 K pot that pumps ^4He is used to re-cool the ^3He gas that has vaporised from the still.

An Oxford Instruments' Kelvinox K100 dilution refrigerator system (see Figure 3.2 (b)) was used for mK measurements. The device is mounted at the bottom of the dip rig and thermally coupled to the mixing chamber via a copper plate, providing excellent thermal conductivity between them. Loom lines (DC) and flexible cables (AC) that come from the top of the insert to the device are wired in a way to maximise their contact with the copper parts of the insert, to ensure the hot temperature in the lines do not reach the mixing chamber; Additional thermal/frequency filters are also installed for the flexible cables. Two fridges were used in the following works: one is a direct-current (DC) fridge where DC or low-frequency measurements are performed; the other is the RF2 fridge that uses fast-pulsing gates and a microwave line. The device remains in the fridge for weeks or months (unlike the Dewar, which is used mainly for testing purposes), depending on the type of experiment. Regular helium-bath and nitrogen-trap refilling is required to maintain the dilution refrigerator at mK. The electron temperature running through a typical SET in the fridge is typically 300 mK, extracted from it's Coulomb peak width, where the peaks are much sharper compared to the ones in 4 K Dewar.

3.3.3 Electronic Measurement Equipment

This section describes the electronic devices commonly used in the experiments. All the instruments can be controlled remotely and monitored by a computer via a general purpose interface bus (GPIB) connector, which allows measurements to be carried out in batches and with complex calculations. GPIB cables also optically isolate the computer from the instruments, shielding the computer from electronic noise. This includes the Kelvinox remote operating system and the superconducting magnet within the fridge.

The Stanford Research Systems Isolated Voltage Source (SIM928) is the main voltage source for the source drain and gates. To protect the device from possible electric shock as a result of battery failure, all the pins are connected with resistive voltage dividers (1:5 dividers). This has the added advantage of offering a finer potential control over the gates. Some gates are even connected with additional dividers for further resolution (1:50 dividers).

Even though most measurements are performed under DC conditions, Stanford Research Systems SR830 lock-in amplifier generates an alternating-current (AC) excitation on the source-drain bias, and measures the conductance of the channel with a frequency range of a few hundred Hz. A 1:10000 divider is connected from the SR830 to the source-drain bias. The advantage of using an AC lock-in conductance measurement is that the background noise can be greatly reduced. The combination of the isolated voltage source and the lock-in amplifier can perform measurements including transport, stability plots and charge sensing.

A FEMTO current amplifier [98] at room temperature offers a significantly

3. EXPERIMENTAL METHODS

reduced noise level, and does not generate a ringing effect, allowing a source-drain current in a pA order of magnitude to be probed. Other instruments such as an arbitrary waveform generator, a digital oscilloscope and digital filters are also used in various experiments in the following chapters.

Chapter 4

Spin Filling of Valley-Orbit States

In this chapter, we report the demonstration of a low-disorder Si MOS QD containing a tunable number of electrons from zero to twenty-seven. The observed evolution of addition energies with parallel magnetic fields reveals the spin filling of electrons into valley-orbit states. We find a splitting of 0.10 meV between the ground and first excited states, consistent with theory and placing a lower bound on the valley splitting. Our results provide optimism for the realisation of spin qubits based on silicon QDs in the near future.

Parts of this chapter have been published in: W. H. Lim, C. H. Yang, F. A. Zwanenburg and A. S. Dzurak, *Nanotechnology* **22**, 335704 (2011).

4. SPIN FILLING OF VALLEY-ORBIT STATES

4.1 Introduction

Semiconductor quantum dots [96] are conduction band islands to which electrons can be added one by one by means of an electric field. Quantum dots provide a promising platform for spin based qubits, with their long coherence times due to the weak coupling of spin to local charge fluctuations. For a quantum dot to be useful as a spin qubit it is essential to understand the details of its excitation spectrum and its spin-filling structure. One powerful method to probe the spin filling is via magnetospectroscopy. This has been applied to both vertical [48] and lateral GaAs/AlGaAs quantum dots [99], showing ground-state spin filling in agreement with Hund's rule.

In this chapter we present the investigation of a Si MOS quantum dot with lower disorder than any studied to date, in which it is possible to analyse the electron occupancy in a manner previously inaccessible. We deduce the spin filling of the first 12 electrons in the dot from ground-state magnetospectroscopy measurements. The formation of a two-electron ($N = 2$) spin-singlet state at low magnetic fields confirms that there is no valley degeneracy present, while the magnetic field dependence of the higher-order Coulomb peaks allows us to deduce the level structure for the first four electrons.

4.2 Device Architecture

In this work, the device is fabricated using a multi-layer Al-Al₂O₃-Al gate stack (see Chapter 3.1). The triple-layer gate stack in our structure (Figure 4.1) provides excellent flexibility for tuning the barrier transparency and the energy levels of the dot independently.

4.2 Device Architecture

The lowest layer of gates is barrier gates (B1 and B2). They are used to define the dot spatially and control the tunnel coupling. The second layer of gates defines the source-drain leads (L1 and L2). The lead gates induce the electron accumulation layers that act as source-drain reservoirs. The plunger gate (P) which extends over the barrier gates, lead gates and the dot island, is used to control the electron occupancy of the dot. The lithographic size of the dot is estimated to be $30 \times 60 \text{ nm}^2$.

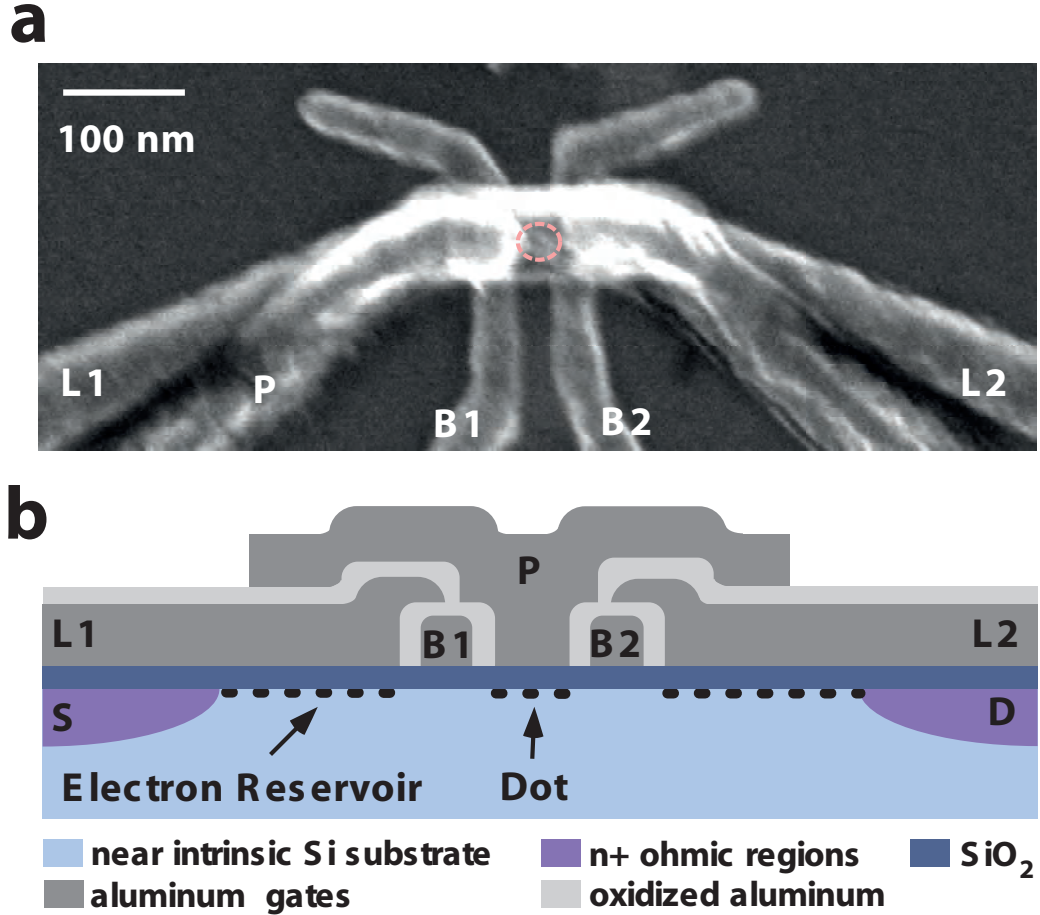


Figure 4.1: Single Dot Device Architecture - a, Scanning electron microscope image and b, Schematic cross-section of a Si MOS quantum dot.

4. SPIN FILLING OF VALLEY-ORBIT STATES

4.2.1 Measurement Configuration

The chip was packaged into a standard 20 pin Charntec package and bonded using an aluminium wedge bonder. Measurements throughout this chapter were performed in a dilution refrigerator with a base temperature of 20 mK. All the gates and source-drain pins are connected with dc loom lines inside the refrigerator. The source-drain conductance was measured using standard ac lock-in techniques described in chapter 3.3.

4.3 Transport Measurements and Bias Spectroscopy

Figure 4.2 is a plot of the differential conductance dI/dV_{SD} of the device versus plunger gate voltage V_P and source-drain voltage V_{SD} , showing the familiar ‘Coulomb diamond’ charge stability map. Before the first charge transition the diamond edges open entirely to a source-drain voltage $|V_{SD}| > 20$ mV, because the quantum dot has been fully depleted of electrons. Our group had previously reported a device with similar gate architecture but an accidental parallel quantum dot created distortion of the charge stability map in the few-electron regime, complicating the interpretation of the dot’s level structure [15]. Here, clear and sharp Coulomb peaks mark the first 27 electrons entering the dot, see Figure 4.3, while the charge stability map of Figure 4.2 shows no distortions from disorder potentials.

As with quantum dots in GaAs/AlGaAs [48], shell filling has been observed in Si/SiGe quantum dots, with a filled shell structure observed for $N = 4$ electrons [89]. The addition spectrum of our Si MOS quantum dot (Figure 4.3) also shows a noticeable peak at $N = 4$. A filled shell at $N = 4$ would be consistent

4.3 Transport Measurements and Bias Spectroscopy

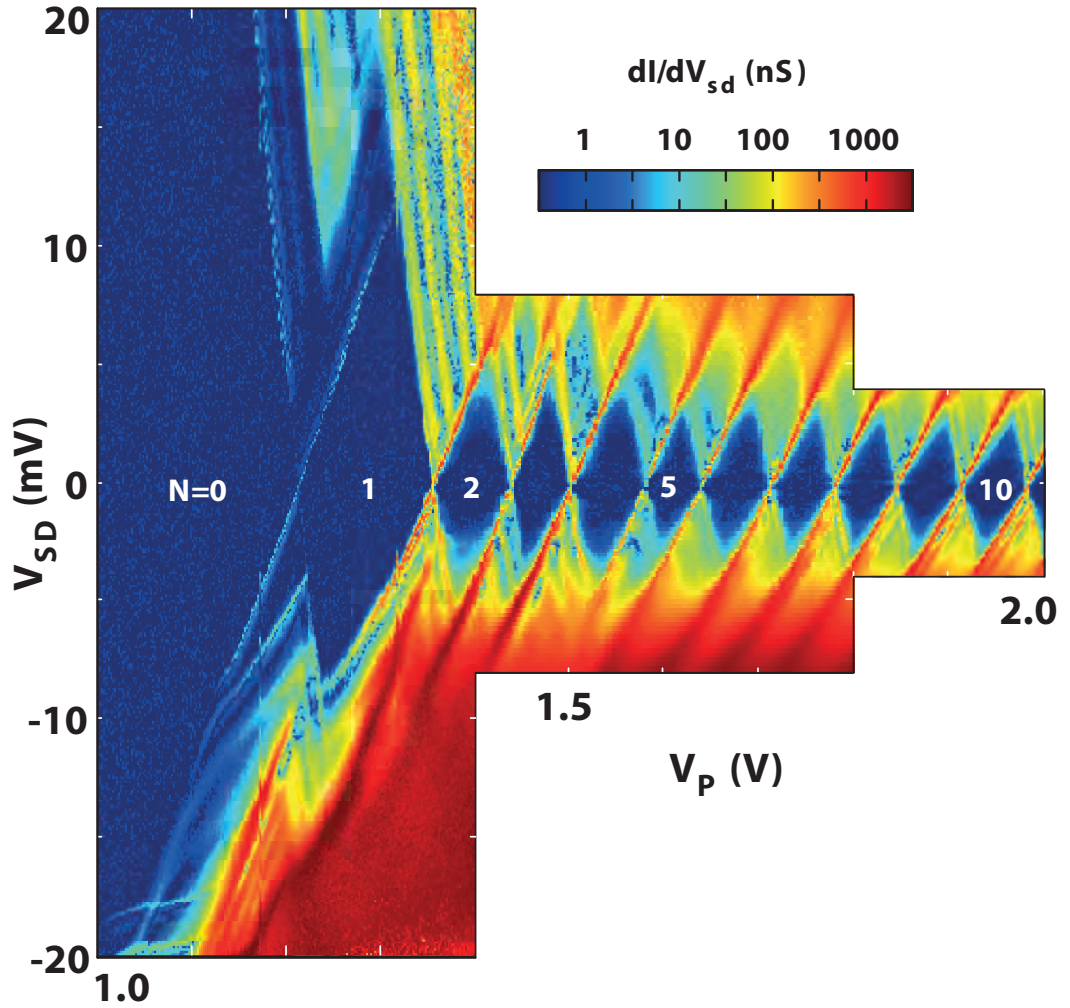


Figure 4.2: Coulomb Diamonds of Single Dot Device - Stability diagram of the device in the few-electron regime. By decreasing the plunger gate voltage V_P , electrons are depleted one-by-one from the dot. The first diamond opens up completely indicating that the first electron has tunneled off the dot.

4. SPIN FILLING OF VALLEY-ORBIT STATES

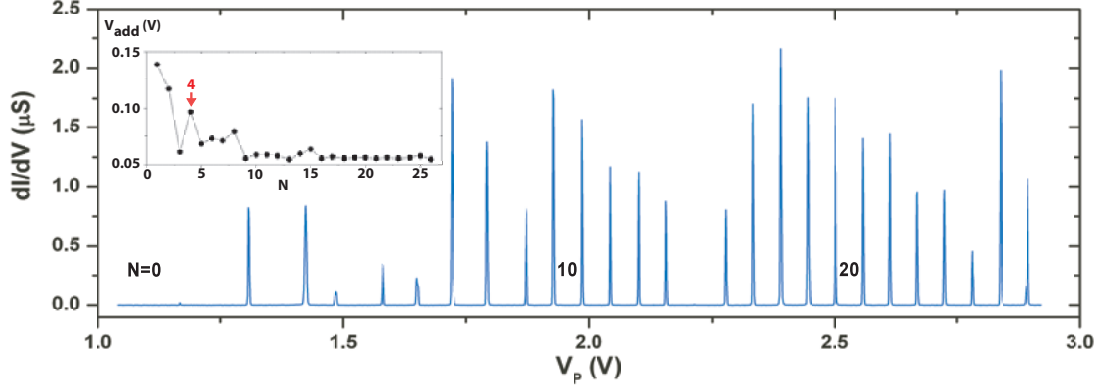


Figure 4.3: Coulomb Peaks from $N = 1$ to 27 - Coulomb oscillations as a function of plunger gate voltage V_P for the first 27 electrons in the dot. V_P is compensated by V_{B2} to suppress the non-monotonic background conductance. Inset: Addition voltage V_{add} versus electron number N calculated as the difference between two consecutive Coulomb peaks in plunger gate voltage.

with the filling of a first orbital state in a two-valley system.

4.4 Spin Filling

4.4.1 Valley-Orbit States

In general, valleys and orbits could hybridise [100], making it inappropriate to define distinct orbital and valley quantum numbers. Depending on the degree of mixing, the valley-orbit levels behave mostly like valleys or like orbits. Instead of referring to a pure valley splitting we therefore adopt the term valley-orbit splitting, $\Delta E_{\text{VO}} = E_{\text{VO}2} - E_{\text{VO}1}$ for the difference in energy between the first two single-particle levels, $E_{\text{VO}1}$ and $E_{\text{VO}2}$. This is sometimes referred to as the ground-state gap [100]. In later chapters, we will discuss how to distinguish and separate the valley and orbital states, using different device structures and

measurement techniques.

4.4.2 Spin State Characterisation via Magnetospectroscopy

Full electrostatic control of the electron number allows us to investigate the spin filling by measuring the magnetic field dependence of the electrochemical potential μ_N , which is by definition the energy required for adding the N^{th} electron to the dot. The slope of $\mu_N(B)$ is given by [101]

$$\frac{\partial \mu_N}{\partial B} = -g\mu_B \Delta S_{\text{tot}}(N), \quad (4.1)$$

where g is the g-factor, the Bohr magneton $\mu_B = 58 \mu\text{eV/T}$ and $\Delta S_{\text{tot}}(N)$ is the change in total spin of the dot when the N^{th} electron is added. The electrochemical potential has a slope of $+g\mu_B/2$ when a spin-up electron is added, whereas addition of a spin-down electron results in a slope of $-g\mu_B/2$. The rate at which μ_N changes with magnetic field thus reveals the sign of the added spin. For the experiments in this work we apply the magnetic field B *parallel* to the Si/SiO₂ interface.

The conductance at the first two charge transitions is plotted as a function of the electrochemical potential energy and the magnetic field in Figure 4.5. Here, the Coulomb peak positions in gate voltage are converted to electrochemical potential μ_N using the lever arm α_P extracted from the corresponding Coulomb diamonds. The blue lines above the Coulomb peaks are guides for the eye with slopes of $\pm g\mu_B/2$, as predicted by equation (1) using $g = 2$ for bulk silicon. Since the first Coulomb peak moves down in energy with increasing magnetic field the peak corresponds to a spin-down electron entering the quantum dot, as expected for the $N = 1$ ground state. For $B \geq 1$ T the second Coulomb peak also falls in

4. SPIN FILLING OF VALLEY-ORBIT STATES

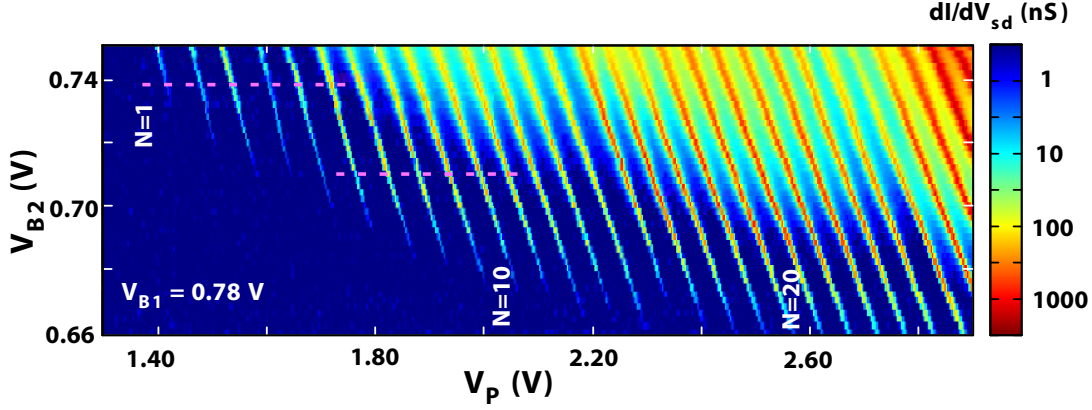


Figure 4.4: Stability Diagram of V_{B2} v.s. V_P - Differential conductance dI/dV_{sd} as a function of barrier gate voltage V_{B2} and plunger gate voltage V_P at $B = 0$ T. The regular parallel Coulomb peaks are a signature of low disorder. The dotted lines point out the regions where spin filling measurements take place.

energy with increasing B at a rate close to $-g\mu_B/2$, however, for low magnetic fields the peak noticeably increases in energy with B , leading to a ‘kink’ (marked 2a) at $B \sim 0.86$ T. This kink (2a) is confirmed by several repeated measurements over positive and negative magnetic field (see supplementary in [88]). These results imply that at low magnetic field (before the kink), the second electron fills the quantum dot with its spin up. As we increase the magnetic field (after the kink), the sign of the second electron spin changes from up to down at $B \sim 0.86$ T.

For $B > 0.86$ T the first two electrons fill two different levels split by $\Delta E_{VO} = 0.10$ meV. We note that the presence of a doubly degenerate ground-state level would demand the two electrons to exhibit parallel spin filling starting from 0 T, since the two electrons would then occupy two different valley states in order to minimise the exchange energy [101].

To assess the degree of valley-orbit mixing we compare the expected values for the orbital level spacing and the valley splitting. As stated above, theoretical

4.4 Spin Filling

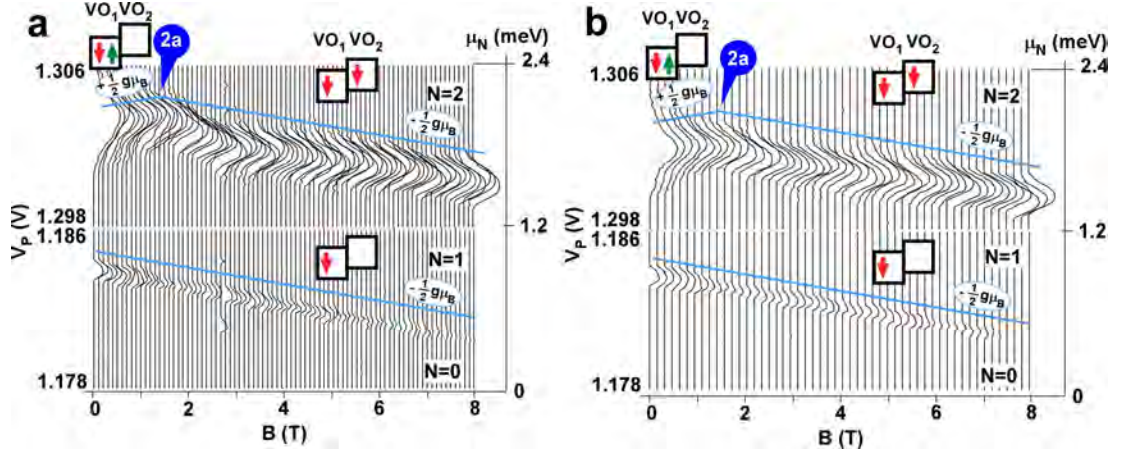


Figure 4.5: Spin filling of $N = 1, 2$ - Magnetospectroscopy of the first two electrons entering the quantum dot. The circle 2a marks a kink in the second Coulomb peak at ~ 0.86 T. (a) and (b) are data sets taken at different time

calculations of the latter predict 0.1–0.3 meV. An estimate of the orbital level spacing in a quantum dot is given by $2\pi\hbar^2/g_v g_s m^* A$ [96], where g_v (g_s) is the valley (spin) degeneracy, m^* the electron effective mass and A the dot area. For non-degenerate valleys, $g_v = 1$ and $g_s = 2$. Using the effective mass of $0.19m_0$, and the lithographic dot area of $\sim 30 \times 60$ nm² we obtain an expected orbital level spacing of 0.7 meV. This value is considerably larger than the lower bound on the valley splitting, suggesting that the first two levels may be valley-like, however, to maintain generality we will continue to refer to the levels as valley-orbit states.

4.4.3 Spin Filling for $N = 2$ to 4 Electrons

We now turn to the spin filling for $N \geq 2$ electrons. Figure 4.4 shows the differential conductance as a function of plunger gate voltage and barrier gate voltage V_{B2} . The highly regular pattern of parallel Coulomb peak lines again demonstrates the low disorder in this device. In order to determine the spin filling for higher electron numbers we investigate the *difference* between successive

4. SPIN FILLING OF VALLEY-ORBIT STATES

electrochemical potentials as a function of magnetic field. The resulting addition energies $E_{\text{add}}(N) = \mu_N - \mu_{N-1}$ have slopes which depend on the spin filling of two consecutive electrons, according to [28]

$$\begin{aligned} \frac{\partial E_{\text{add}}(N)}{\partial B} &= 0 && \text{for } \downarrow, \downarrow \text{ or } \uparrow, \uparrow \\ &= -g\mu_B && \text{for } \uparrow, \downarrow \\ &= +g\mu_B && \text{for } \downarrow, \uparrow \end{aligned} \quad (4.2)$$

where the first (second) arrow depicts the spin of the $(N - 1)^{\text{th}}$ (N^{th}) electron respectively.

Figure 4.6 (a) plots the measured addition energies, $E_{\text{add}}(N) = \mu_N - \mu_{N-1}$, for $N = 2$ to $N = 4$ electrons for magnetic fields B in the range of $-8 \text{ T} < B < 8 \text{ T}$. We see that the data in Figure 4.6 (a) tend to follow $\partial E_{\text{add}}(N)/\partial B = 0, \pm g\mu_B$, as expected from Equation (2). Furthermore, the $E_{\text{add}}(N)$ data is relatively symmetric about $B = 0$, indicating that the trends are real and not measurement artefacts. As a guide to the eye, we also show lines with slopes of *exactly* $0, \pm g\mu_B$ (blue lines in Figure 4.6 (a) that we interpret the $E_{\text{add}}(N)$ to be following. While in regions the match is not exact, we propose that these trend lines are the best qualitative fit to the data. We are thus able to infer spin states for each of the first 4 electrons at all values of magnetic field $|B| < 8 \text{ T}$. These spin states are labelled with red (green) arrows, representing spin down (up), in Figure 4.6 (a).

We now focus on the spin states of these four electrons, $N = 1$ to $N = 4$. At low magnetic fields ($< 0.8 \text{ T}$), the electrons populate the quantum dot ground states with alternating spin directions: $\downarrow, \uparrow, \downarrow, \uparrow$. Conversely, at high magnetic fields ($> 4 \text{ T}$) a configuration with four spin-down electrons has least energy: $\downarrow, \downarrow, \downarrow, \downarrow$. Recently, parallel spin filling in a Si quantum dot was explained as a

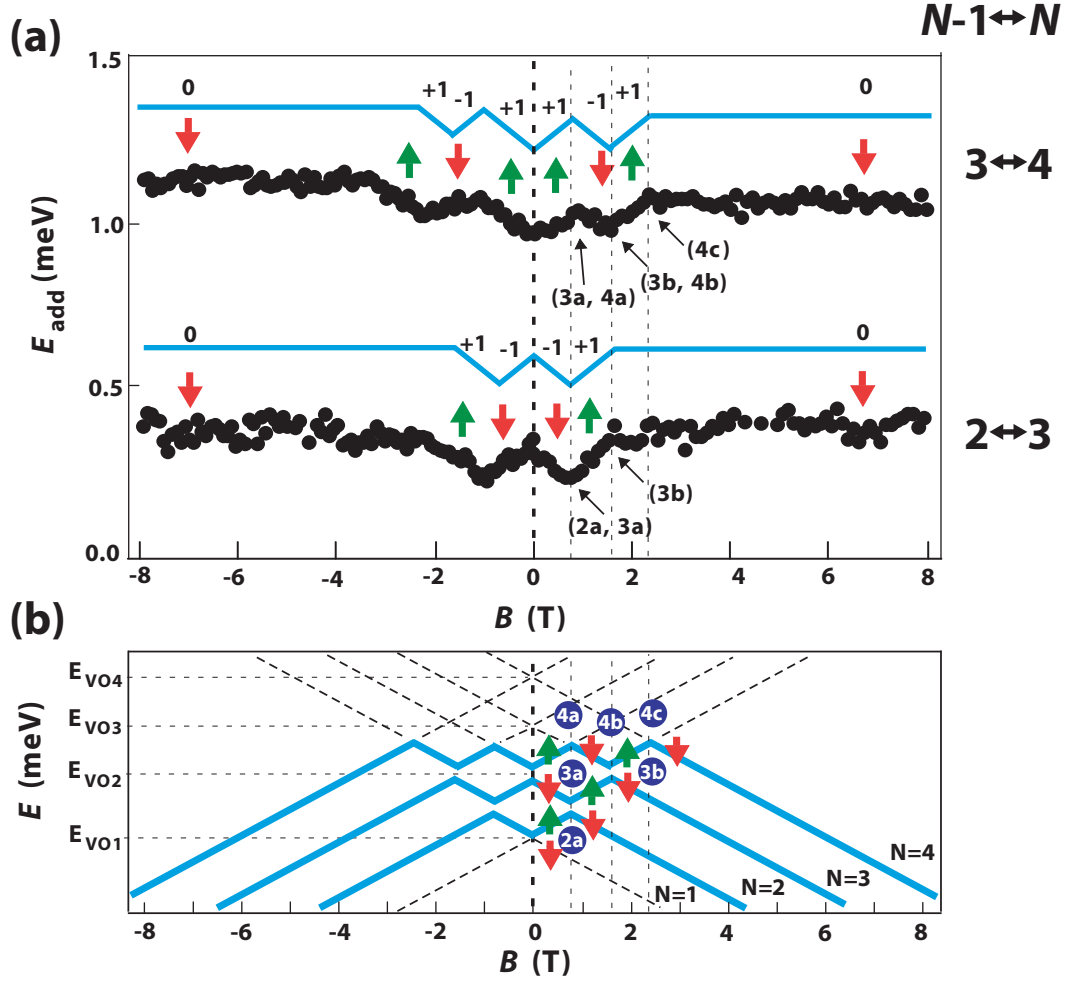


Figure 4.6: Spin filling of $N = 3, 4$ - (a) Addition energies of the 3rd and 4th electrons versus magnetic field. Kinks are reproducible and approximately symmetric over positive and negative magnetic fields. (b) A simple model showing the evolution of single-particle energy levels $E_{\text{VO}i}$ of valley-orbit i assuming only the Zeeman shift. Each level splits into two levels $E_{\text{VO}i} \pm \frac{1}{2}g\mu_B B$ at non-zero magnetic fields. The level crossings fit the kinks observed in the first four Coulomb peaks shown in Figure 4.5

4. SPIN FILLING OF VALLEY-ORBIT STATES

result of a large exchange energy and an unusually large valley splitting of 0.77 meV [91]. When the level spacing is smaller than the exchange energy, it is energetically favoured for two electrons to occupy two consecutive levels with the same spin sign. This is not the case for the device measured here: the anti-parallel spin filling of the first two electrons below 0.86 T is only possible in case of a small exchange energy (less than ΔE_{VO}). This is an unexpected result for a dot of this size where the exchange energy is predicted to be larger than the orbital level spacing [101]. Possibly the Coulomb interaction in the dot is strongly screened by the plunger gate. This is not unlikely since the distance from gate to dot (10 nm) is smaller than the dimensions of the dot itself (30–60 nm).

In Figure 4.6 (b), we illustrate the magnetic-field evolution of four non-degenerate valley-orbit levels by means of an elementary model. Each level splits into spin-up and spin-down levels in finite magnetic field. We assume that the exchange interaction is small in comparison to the level spacing. The level crossings that follow from our model fit the kinks observed in the first four Coulomb peaks. The observed kink positions yield three valley-orbit levels which are 0.10, 0.23 and 0.29 meV above the lowest ground state level. The extracted level spacings for the first four valley-orbit states are then: $E_{\text{VO}2} - E_{\text{VO}1} = 0.10$ meV; $E_{\text{VO}3} - E_{\text{VO}2} = 0.13$ meV; and $E_{\text{VO}4} - E_{\text{VO}3} = 0.06$ meV.

4.4.4 Spin Filling for $N = 5$ to 12 Electrons

Figure 4.7, we plot the addition energies $E_{\text{add}}(N)$ as a function of B for electrons $N = 5$ to 12. Once again, we predominantly observe slopes of $\partial E_{\text{add}}(N)/\partial B = 0, \pm g\mu_B$, as expected from Equation (2). Occasionally, e.g. at $N = 6 \leftrightarrow 7$, a

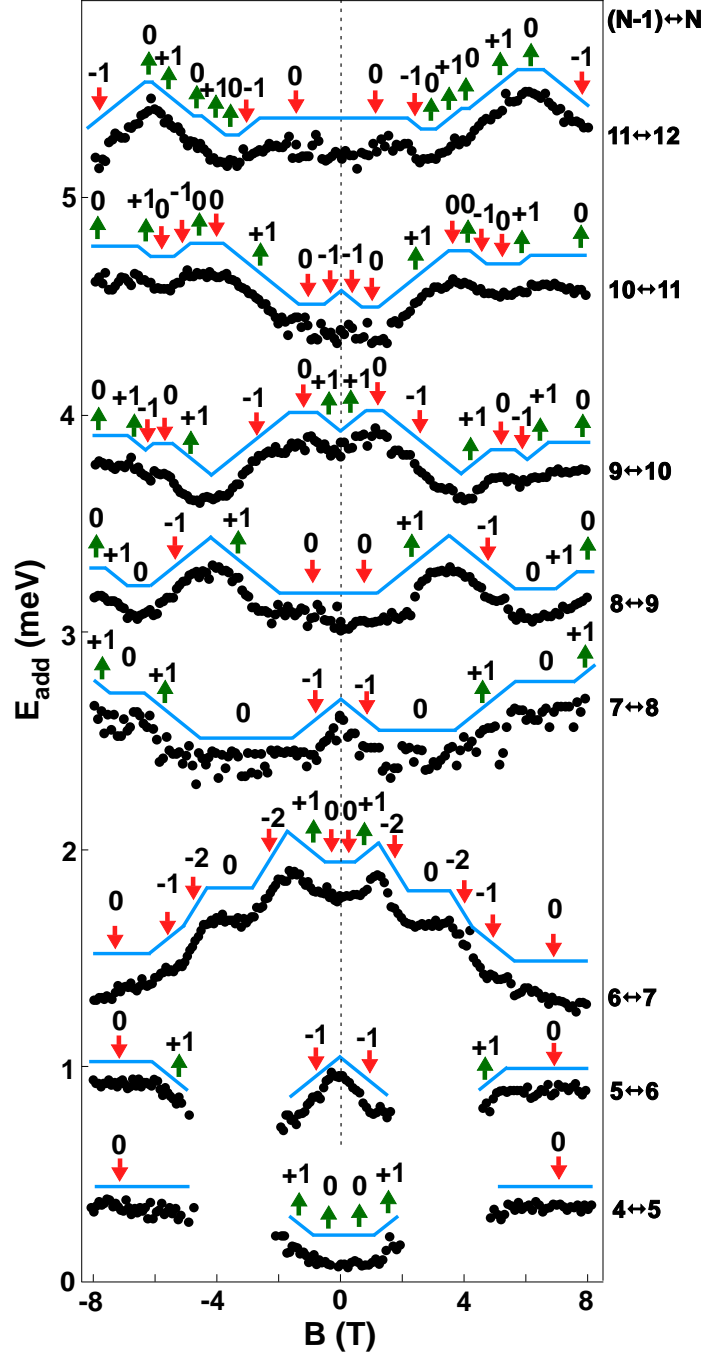


Figure 4.7: Spin filling of $N = 5$ to 12 - Addition energies $E_{\text{add}}(N)$ as a function of B for electrons $N = 5$ to 12.

4. SPIN FILLING OF VALLEY-ORBIT STATES

segment has a slope of $\pm 2g\mu_B$, because the total spin on the dot changes by more than $\frac{1}{2}$. This can occur due to many-body interactions on the dot and lead to spin blockade [102]. The latter phenomenon could also explain the suppression of current in the fifth charge transition at $B = 2\text{--}5$ T [101, 103, 104].

Also, the picture of alternating spin filling below 0.8 T no longer holds for $N > 4$. Unexpectedly, the fifth electron is spin up at low magnetic field, while the lowest-energy configuration predicts a spin-down state. This anomaly could be explained by an extra electron in a dot nearby, which alters the spin configuration of the main dot. Such a small dot can be created at high plunger gate voltages, where the potential well differs from a perfect parabola.

4.5 Conclusions

The results here show that silicon MOS quantum dots can be fabricated with the low levels of disorder necessary to form well-defined electron spin qubits in a host material that can be made almost free of nuclear spins. The excellent charge stability allows the spin states of the dot to be mapped up to $N = 12$ electrons and a valley-orbit splitting of 0.10 meV to be extracted. Theoretical study [66] has shown that a valley splitting of 0.1 meV is sufficient for the operation of a silicon double quantum dot as a singlet-triplet qubit, in analogy with recent experiments in GaAs [11]. Given that the valley-orbit splitting is strongly dependent on the interfacial electric field, it should be possible to further increase the splitting via appropriate device engineering and gate configuration, demonstrated in later chapters. Our results therefore provide real promise for the realisation of low-decoherence spin qubits based upon silicon MOS technology.

Chapter 5

Dynamically Controlled Charge Sensing

This chapter reports charge-sensing measurements of a silicon MOS QD using a single-electron transistor as a charge sensor with dynamic feedback control. Using digitally-controlled feedback, the sensor exhibits sensitive and robust detection of the charge state of the QD, even in the presence of charge drifts and random charge upset events. The sensor enables the occupancy of the QD to be probed down to the single-electron level.

Parts of this chapter have been published in: C. H. Yang, W. H. Lim, F. A. Zwanenburg and A. S. Dzurak, *AIP Advances* **1**, 042111 (2011).

5. DYNAMICALLY CONTROLLED CHARGE SENSING

5.1 Introduction

Non-invasive charge sensing [105] is an invaluable tool for the study of electron charge and spin states in nanostructured devices. It has been used to identify electron occupancy down to the single electron level [51, 60] and has made possible the single-shot readout of single electron spins confined in both quantum dots [106] and dopants [46]. Both quantum point contacts (QPCs) and single electron transistors (SETs) possess high transconductance, making them sensitive to their local electrostatic environment and therefore excellent charge sensors. A QPC can be conveniently integrated with lateral quantum dot structures formed in two-dimensional electron layers in GaAs/AlGaAs [52, 53, 54, 55], Si/SiGe [60, 61] and Si metal-oxide-semiconductor field-effect transistors (MOSFETs) [91, 107]. SETs also have been integrated with quantum dots in a variety of structures including Ge/Si core/shell nanowires [108], carbon nanotubes [109], graphene [110] and Si MOSFETs [111].

In this chapter we demonstrate a silicon MOS quantum dot [14, 15] integrated with a nearby SET charge sensor [112], using a dynamic feedback technique to maintain constant charge sensitivity over a wide operating range. The feedback algorithm dynamically adjusts the gate-voltage of the SET to ensure that it operates at a constant output current. In this configuration the SET optimally responds to changes in the local electrostatic environment, such as electron tunnelling events. In contrast with previous sensing measurements, the dynamic feedback employed here allows the SET sensor to recover from random charging events that would otherwise reduce the sensitivity of the sensor. This enables high-sensitivity measurements to be obtained over many hours, even in the pres-

5.2 Device Architecture and Measurement Set-up

ence of random and large charge upset events.

5.2 Device Architecture and Measurement Set-up

Figure 5.1 shows a scanning electron microscope (SEM) image and schematic of the structure used for these experiments. In this structure, the roles of the quantum dot and SET charge sensor are interchangeable. Here, we operate the lower device as the quantum dot while the upper device acts as the charge sensor.

Ten gate electrodes are used to electrostatically define the two devices, which can be independently measured. Positive voltages on the gates are used to induce electron accumulation layers below the Si-SiO₂ interface. Barrier gates B1-B4 produce tunnel barriers in the electron layers, as shown in Figure 5.1 (b). In both devices the dot (or SET island) electron occupancy is controlled by a ‘plunger’ gate, labelled PD for the dot and PS for the SET, while ‘lead gates’ L1-L4 are used to induce the four source and drain electron reservoirs for the two devices.

We operated the quantum dot with an ac excitation voltage V_{sd} of 100 μeV at 87 Hz and the SET with V_{sd} of 400 μeV at 133 Hz. The lead gates of both dot and SET were fixed at $V_{L1,L2,L3,L4} = 3.0$ V to induce the electron reservoirs. The barrier gates were operated in the range $V_{B1,B2,B3,B4} = 0.6\text{--}0.7$ V.

The spacing between the quantum dot and the island of the SET charge sensor was ~ 120 nm. We also studied devices separated by 1 micron, where an additional metallic antenna was used to enhance the capacitive coupling from the dot to the SET island [108, 109, 113]. In those devices the electron accumulation

5. DYNAMICALLY CONTROLLED CHARGE SENSING

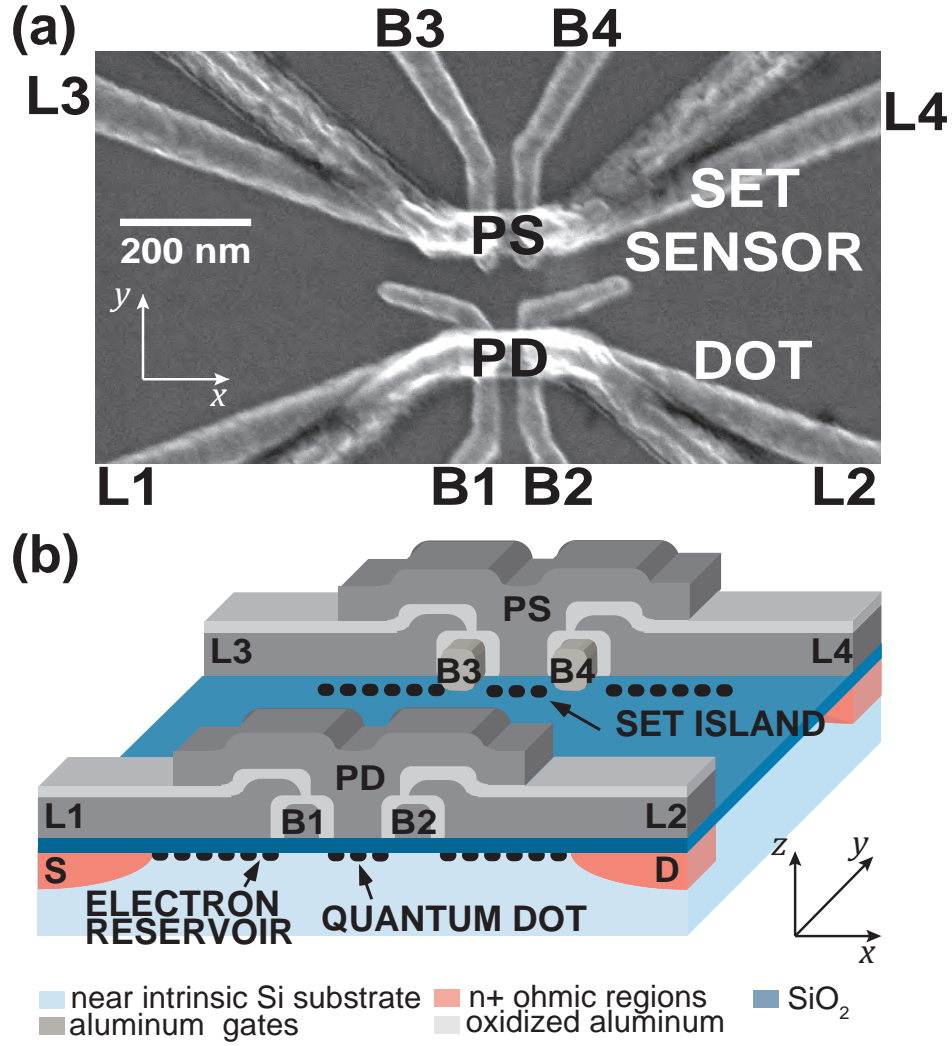


Figure 5.1: Single Dot with Charge Sensor - (a) SEM image of the silicon MOS device, the bottom one operating as the dot and the upper one as the charge sensor. (b) The 3D schematic model of the device.

5.2 Device Architecture and Measurement Set-up

layer in the leads strongly screened the capacitance from antenna to both islands, preventing effective charge sensing. We therefore found that a directly coupled device, as shown in Figure 5.1, was the most effective.

Charge sensing of the quantum dot by the SET is performed by measuring both devices simultaneously, as depicted in Figure 5.2(a). Using the SET plunger gate PS we tune the current I_S of the SET to the edge of a Coulomb peak, where the transconductance dI_S/dV_{PD} is high, thus enabling the detection of single-electron transfers in the quantum dot, the latter controlled using its plunger gate PD.

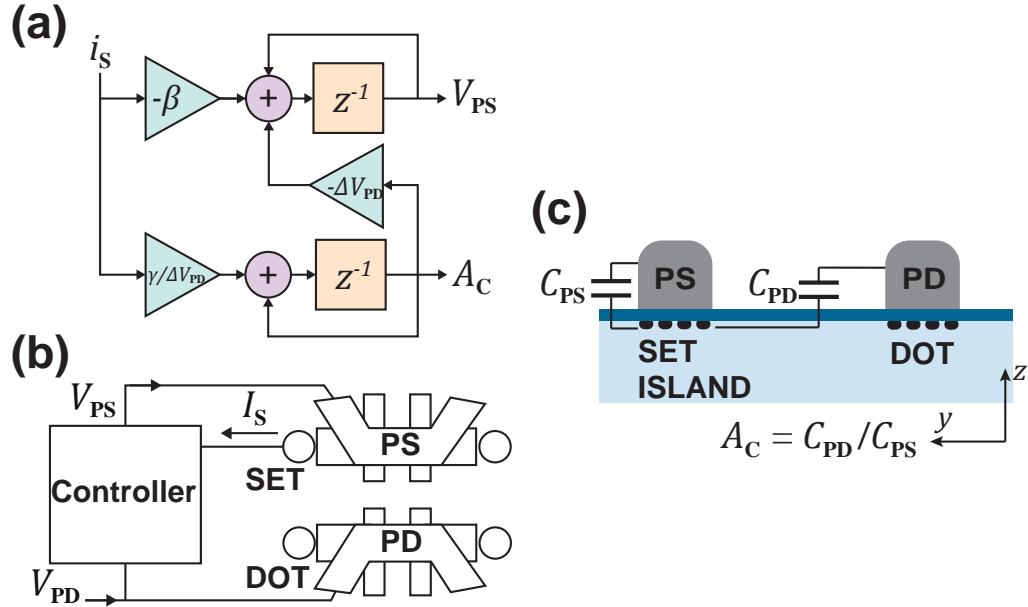


Figure 5.2: Feedback Controller Block Diagram - (a, b) Block diagram of the second-order feedback control system used to ensure stable and continuous charge sensing of the quantum dot by the SET sensor. (c) Physical interpretation of mutual capacitance ratio, $A_C = C_{PD}/C_{PS}$.

5. DYNAMICALLY CONTROLLED CHARGE SENSING

5.3 Charge Sensing Results for a Single QD

Figure 5.3(a) shows the correlated signals of the quantum dot current I_D (black line) and the sensor current, I_S , with both uncompensated (magenta) and fixed compensated (dark blue) sensor control. When there is a single-electron transfer in the quantum dot (corresponding to a Coulomb peak in I_D), an abrupt change appears in the sensor current trace I_S (uncompensated). As we reduce V_{PD} , I_S will gradually shift away from the Coulomb peak edge because the sensor island is capacitively coupled to the dot plunger. Hence, this does not give a uniform single-electron transfer detection signal.

Fixed compensation improves the sensitivity of the charge sensing technique, leading to the dark blue trace in Figure 5.3(a). Here, we adjust the sensor gate voltage by ΔV_{PS} , in proportion to ΔV_{PD} at a fixed ratio. The sensor current I_S now operates within a fixed range, keeping approximately the same position near the edge of the Coulomb peak. The transconductance dI_S/dV_{PD} of the sensor current, obtained numerically, is plotted as an orange trace in Figure 5.3(a). Each time the occupancy of the quantum dot changes by one electron it produces a sharp negative peak in dI_S/dV_{PD} . The sensor also detects an additional charge movement near $V_{PD} = 1.46$ V, whereas I_D does not show any corresponding transport current through the dot.

We are able to distinguish the main (gate-defined) quantum dot from other unintentional (disorder-induced) dots or traps by observing the difference in amplitudes and the positions of the charge sensing signals. Arrow in Figure 5.3(a) indicate the detection of a charge upset outside the main dot. The Coulomb peaks in I_D have a regular pattern, whereas the observed ‘trap’ charging signal is between

5.3 Charge Sensing Results for a Single QD

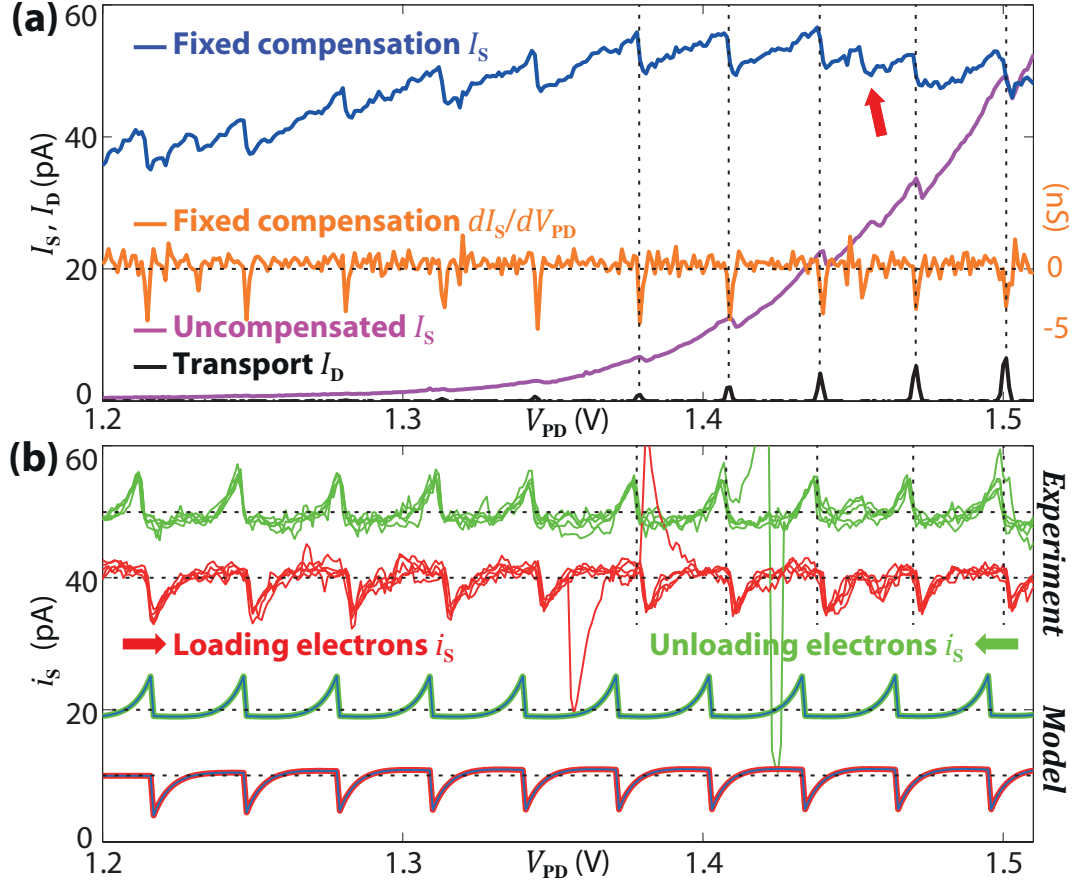


Figure 5.3: Charge Sensor and Transport Currents - (a) SET sensor current I_S without compensation (magenta) and dot transport current I_D (black). Fixed compensation is applied by linearly adjusting the sensor gate potential V_{PS} and the compensated I_S (dark blue) then operates within a fixed range, with a corresponding transconductance dI_S/dV_{PD} (orange). (b) Sensor error current i_S with dynamic feedback compensation applied while ramping V_{PD} up (red) and down (green), with 5 overlaid traces. And modelled i_S for the same range of experimental parameters. I_S operating point is set to $I_0 = 50$ pA and the traces have been offset for clarity. Here, $\beta = 4$ M Ω and $\gamma = 80$ k Ω .

5. DYNAMICALLY CONTROLLED CHARGE SENSING

two Coulomb peaks and is not visible in I_D . The ability to distinguish the origin of charge movements makes SET or QPC sensing a valuable characterisation tool for the study of quantum dots and has motivated its use in many experiments discussed earlier [33, 46, 51, 52, 53, 54, 55, 60, 61, 91, 107, 108, 109, 110, 111].

Despite its utility, fixed compensation of the charge sensor suffers from two significant problems: (i) the effect of slow charge drifts; and (ii) sudden and random charge upset in the environment that cause significant changes in the sensor current and which cannot be compensated for. Maintaining the stability of the charge sensor output over a long period of time is therefore difficult without some form of feedback. Here, dynamic feedback is used to control the charge sensor and correct for both of the fore-mentioned problems. A computer-controlled second-order feedback algorithm adjusts the plunger gate PS of the charge sensor, by taking I_S as the feedback signal and re-tuning V_{PS} for each sample x being measured.

Figure 5.2 (a) shows the block diagram for this dynamically-controlled charge sensor, which can be described by the following equations:

$$V_{PS}[x+1] = V_{PS}[x] - \beta i_S[x] - \Delta V_{PD} A_C[x] \quad (5.1a)$$

$$A_C[x+1] = A_C[x] + \frac{\gamma}{\Delta V_{PD}} i_S[x] \quad (5.1b)$$

Here, ΔV_{PD} is the dot-plunger-gate step size and $A_C = C_{PD}/C_{PS}$ is the mutual capacitance ratio between the dot-plunger PD to sensor island and the sensor-plunger PS to sensor island (see Figure 5.2(c)). The parameter β controls the first-order feedback, which governs the decay rate of the error current, $i_S = I_S - I_0$, where I_0 is the sensor ac operating point. Note that when we apply

5.3 Charge Sensing Results for a Single QD

fixed compensation we have $\beta = 0$ and A_C is constant. In practice, A_C can also experience sudden changes in the presence of charge upset and the parameter γ governs the decay rate of A_C back to its steady-state value after an upset. Both β and γ are chosen to give a feedback system with good stability and a reasonable response time, while ensuring that I_S operates at the desired operating point I_0 .

Charge sensing results with dynamic feedback control are shown in Figure 5.3(b). Five overlaid traces for two opposing gate sweep directions are shown. When we increase the dot-plunger voltage V_{PD} (red traces), the charge sensor detects electrons loading into the quantum dot, and a sudden decrease in i_S occurs for each loading event. This drop triggers the feedback system to increase V_{PS} in order to pull I_S back to the operating point I_0 . In contrast, when we increase the dot-plunger voltage V_{PD} (green traces), an electron moving out of the dot causes a sudden increase in i_S . The feedback mechanism then gradually decreases I_S back to I_0 . Figure 5.3(b) also shows the modeled values using the same parameters as the controller and the measured physical properties of the device. Good agreement between the model and the experimental results confirms that the feedback system is working as designed.

In the experimental data of Figure 5.3(b) we observe a large upset event in the up-sweep (red trace) at $V_{PD} \sim 1.35$ V, corresponding to what must have been a large and random charge upset in the device. Significantly, the feedback control enabled the sensor current I_S to return to its optimal operating point I_0 after this event, meaning that charge sensing could then continue. With only fixed compensation applied, such a dramatic upset would most likely have shifted the sensor to a near zero current and charge sensing would have been significantly impeded. This demonstrates the utility of the dynamic feedback compensation

5. DYNAMICALLY CONTROLLED CHARGE SENSING

for charge sensing over long time periods, which is often necessary in order to fully characterise a quantum dot system or other nanostructures.

In order to further assess the robustness of the technique we studied the charge state of the quantum dot by mapping the sensor error current i_S as a function of the dot plunger gate V_{PD} and one of the dot barrier gates V_{B2} – see Figure 5.4(a). The interlaced positive (negative) sweeps of the plunger gate voltage produce dips (peaks) in i_S , thus mapping the charge transitions in the quantum dot. We set the grey scale in the map in such a way that loading (unloading) of an electron appears as a white (black) pixel in Figure 5.4(a). Randomly occurring white and black pixels corresponds to charging and ionisation of charge traps. This data was obtained over 10 hours and the level of sensitivity and sensor operating point remained constant over this entire period, despite the occurrence of a number of upset events.

Several interesting features are observed in Figure 5.4(a). The main quantum dot contains no electron on the far left side of the plot, since there are no more charge transitions. The first two transition lines have a different slope to the other regular ones. We believe that at low V_{PD} , the shape of the potential well in the quantum dot may have deformed due to the presence of local disorder. This changes the coupling of the dot-plunger gate to the quantum dot resulting in a different slope. Another feature observed is the hysteresis present when loading/unloading the first two electrons, with the loading and unloading events occurring at different values of V_{PD} . The red arrows show the intersections of the main transitions and a line where hysteresis occurs. The origin of this hysteresis is most likely related to non-equilibrium charge coupling between the main dot and a nearby charge trap.

5.3 Charge Sensing Results for a Single QD

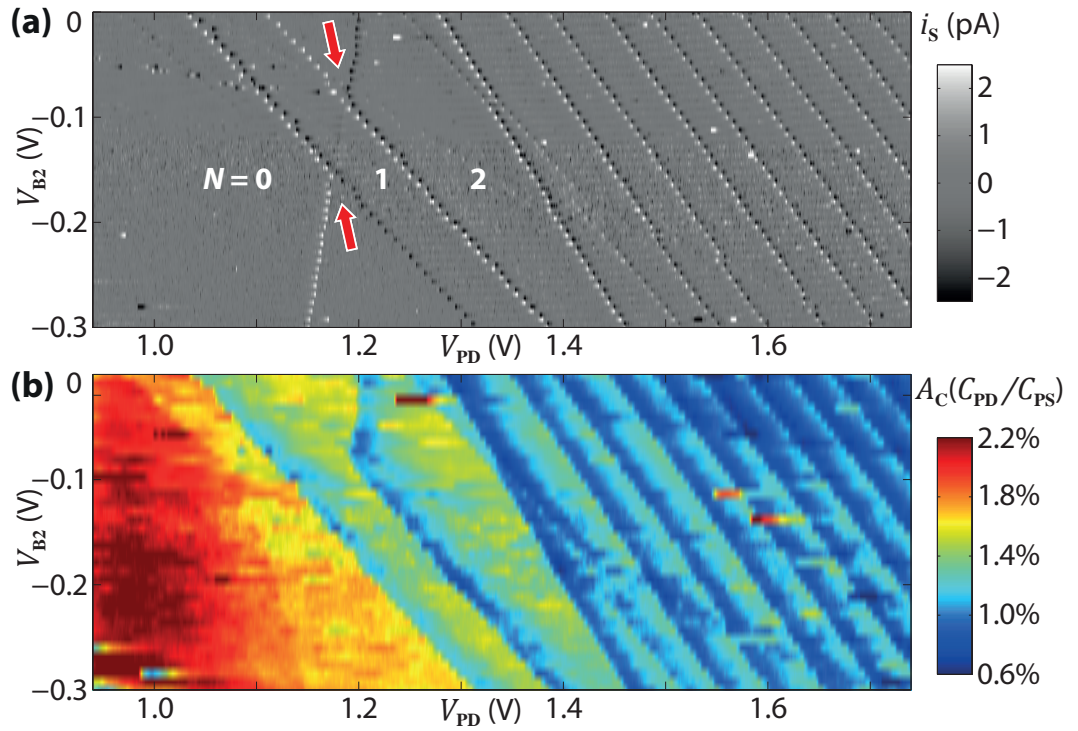


Figure 5.4: Stability Diagram with Charge Sensor - (a) Stability diagram of I_S showing the charge transitions. I_S now has an operating point I_0 of 80 pA. (b) Mutual capacitance ratio A_C (C_{PD}/C_{PS}), with positive sweeping only, showing the change in A_C when charge movement occurs.

5. DYNAMICALLY CONTROLLED CHARGE SENSING

The mutual capacitance ratio A_C calculated by the feedback control system provides an additional parameter to aid understanding of the quantum dot system. It represents the change in C_{PD} with different electron occupancy, assuming C_{PS} stays constant. Figure 5.4(b) plots A_C , obtained simultaneously with the data in Figure 5.4(a), and supports the assignment $N = 0$ for the electron occupancy at low gate voltages. When $N = 0$, C_{PD} increases significantly, due to the absence of the capacitive screening effect of the electrons in the dot.

We note that a similar SET architecture by Angus *et al.* [112] demonstrated the capability of radio-frequency charge detection with sensitivities of better than $10 \mu e / \sqrt{\text{Hz}}$. Hence, we expect that our SET structure and digital feedback system should be able to perform time-averaged sensing at MHz bandwidth. However in this experiment, the electrical setup is designated for low-frequency measurements only.

5.4 Conclusions

In conclusion, we have used a silicon single electron transistor to demonstrate charge sensing of a nearby silicon MOS quantum dot. We observed single electron occupancy of the dot and demonstrated the benefits of dynamic feedback control. The control algorithm is highly robust against charge drifts and random charge upset events, enabling measurement stability for long periods (up to hours) and over a wide range of gate biases. This device architecture and sensing technique has excellent potential for future experiments such as single-shot electron spin readout and charge sensing in double quantum dots.

Chapter 6

Excited State Spectroscopy of Orbital and Valley Levels

Understanding interactions between orbital and valley quantum states in silicon nanodevices is crucial in assessing the prospects for spin-based qubits. In this chapter, we study the energy spectra of a few-electron silicon MOS QD using dynamic charge sensing and pulsed-voltage spectroscopy. The occupancy of the QD is probed down to the single-electron level using a nearby single-electron transistor as a charge sensor. The energy of the first orbital excited state is found to decrease rapidly as the electron occupancy increases from $N = 1$ to 4. By monitoring the sequential spin-filling of the dot, we extract a valley-splitting of $\sim 230 \mu\text{eV}$, irrespective of electron number. This indicates that favourable conditions for qubit operation are in place in the few-electron regime.

Parts of this chapter have been published in: C. H. Yang, W. H. Lim, N. S. Lai, A. Morello and A. S. Dzurak, *Physical Review B* **86**, 115319 (2012).

6. EXCITED STATE SPECTROSCOPY OF ORBITAL AND VALLEY LEVELS

6.1 Introduction

In order to assess whether a quantum device shows valley splitting compatible with use in spin-based quantum computing, orbital and valley spectra must be extracted. In particular, it is of interest to probe the relative magnitude of the valley and orbital energy spacing to determine the degree of mixing of these states [100] and ultimately identify the most appropriate strategy for qubit operation [114].

In this work, we use pulsed-voltage spectroscopy to investigate the excitation energy spectra of a nearly-closed silicon metal-oxide-semiconductor (MOS) QD in the few-electron regime ($N \leq 4$). In a magnetic field we observe Zeeman shifts of the ground state, valley excited state, and first orbital excited state that allow us to determine the sequential spin filling of the N -electron states. Interestingly, the energy of the first orbital excited state is seen to decrease rapidly as the dot occupancy increases, whereas a valley splitting of $\sim 230 \mu\text{eV}$ is found not to depend on electron number. This has the significance of guaranteeing the existence of a well-defined spin-1/2 qubit Hilbert space, sufficiently separated from higher-energy excitations.

6.2 Device Architecture and Measurement Setup

Figure 6.1 shows a scanning electron microscope (SEM) image of a device identical to the one under study; in the experiments presented here, only the (false) coloured gates are used. A quantum dot is formed between the left and right barrier gates (LB, RB) and is independently controlled by the plunger gate (P). By applying a positive voltage on the lead gate (LD), an electron accumulation

6.2 Device Architecture and Measurement Set-up

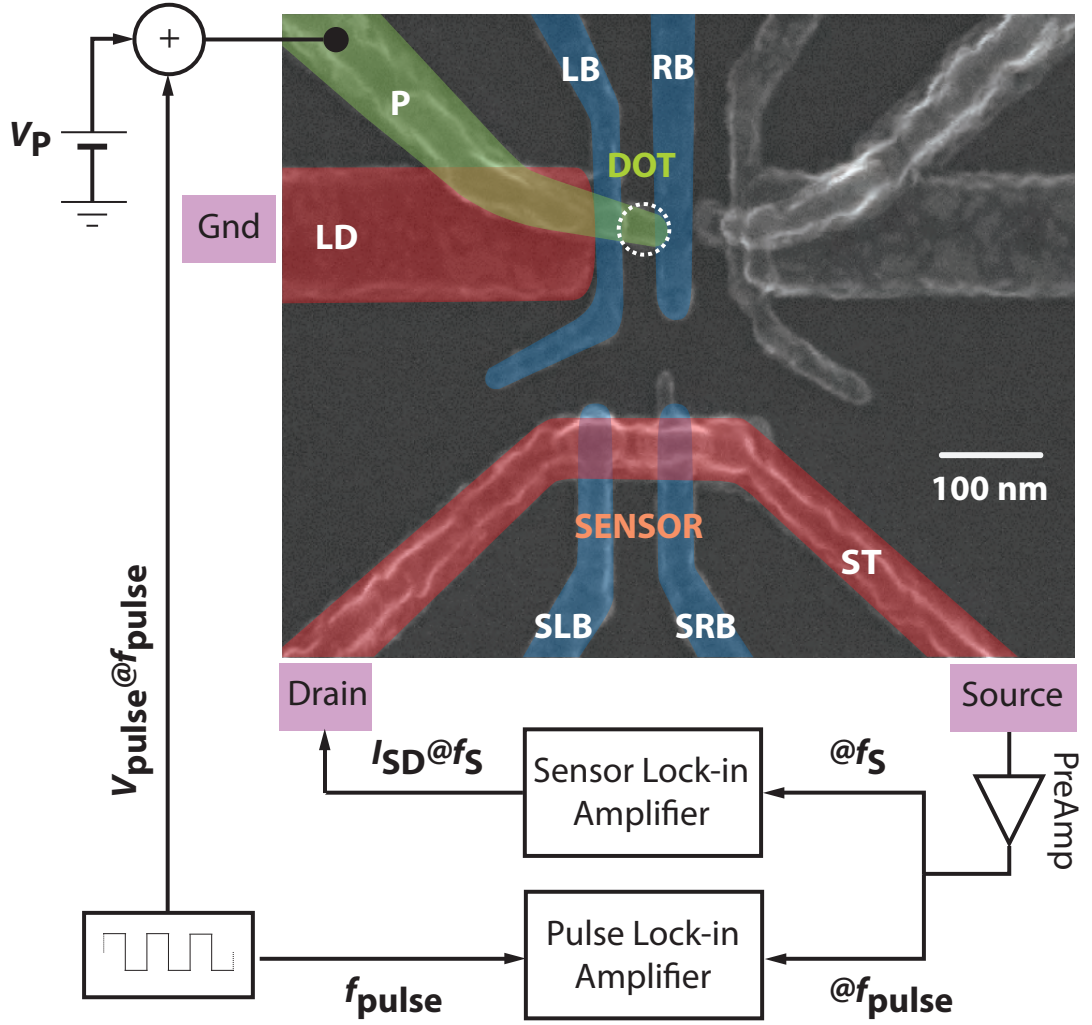


Figure 6.1: Single Dot with Charge Sensor - SEM image of a quantum dot integrated with a SET and the measurement set-up. Only colored gates are used in the experiments.

6. EXCITED STATE SPECTROSCOPY OF ORBITAL AND VALLEY LEVELS

reservoir is induced at the Si/SiO₂ interface. Electrons from the reservoir can then tunnel on and off the quantum dot through the left barrier. Next to this single-lead quantum dot is a single-electron transistor (SET) sensor (S) which is used to detect the electron tunneling events to/from the quantum dot. The SET top gate (ST) forms an electron channel from source to drain and the two underlying barrier gates (SLB, SRB) create tunnel barriers, forming an electron island in between.

In order to characterise the excitation spectrum [115] of the QD, we make use of the technique developed by Elzerman and co-workers [106] which combines charge detection and gate pulsing. We apply an *ac* excitation voltage of 200 μV at $f_S=173$ Hz to the drain of the SET and monitor the sensor current I_S locked-in to f_S at the source through a low-noise room temperature preamplifier. Simultaneously, a train of voltage pulses with amplitude V_{pulse} is applied to gate P, in addition to its dc voltage V_P , shifting the energy levels of the dot up and down. This pulse train modulates the sensor current via a cross-capacitance at a frequency f_{pulse} and the resulting current I_{pulse} at this frequency is measured with a second (*Pulse*) lock-in amplifier, as shown in Figure 6.1. In order to maximise charge sensitivity in the detector, we employ dynamic compensation, as described in Yang *et al.* [116]. We first tune the SET so that the sensor lock-in current I_S is at the edge of a Coulomb peak, where the transconductance dI_S/dV_{ST} is high (2 nS). We then monitor the charge state of the quantum dot using the sensor signal I_S while the SET gate voltage V_{ST} is dynamically adjusted in order to maintain an approximately constant sensor signal I_S . This makes our read-out signal virtually unaffected by slow charge drifts and random charge rearrangements, which would otherwise prevent optimal bias.

6.3 Quantum Dot Occupancy and Measurement of Excited States

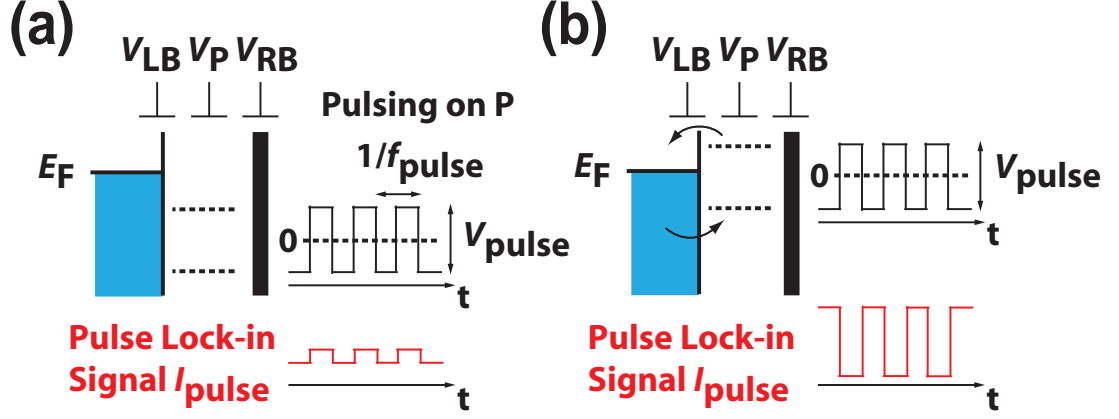


Figure 6.2: Pulsing Schematic - (a)(b) Schematic energy diagrams during pulsing of gate P with two different V_P offsets.

Figure 6.2(a)(b) show schematic energy diagrams of electrons loading and unloading the quantum dot through the left barrier while the right barrier is raised high to completely cut off the channel. The electron tunnel rate is independently controlled by the left barrier gate voltage V_{LB} . In (b), both the high and low phase of the pulse are below the Fermi level E_F of the electron reservoir. Hence, there is no change in electron occupancy of the dot and the pulse lock-in detection signal I_{pulse} is small, due only to capacitive coupling between the plunger gate and the sensor. Conversely, in (c), an electron can tunnel into the quantum dot from the reservoir during the high phase of the pulse (low in potential) and tunnel off when the pulse phase is low (high in potential). This change of electron occupancy in the dot induces a much larger lock-in detection signal I_{pulse} .

6. EXCITED STATE SPECTROSCOPY OF ORBITAL AND VALLEY LEVELS

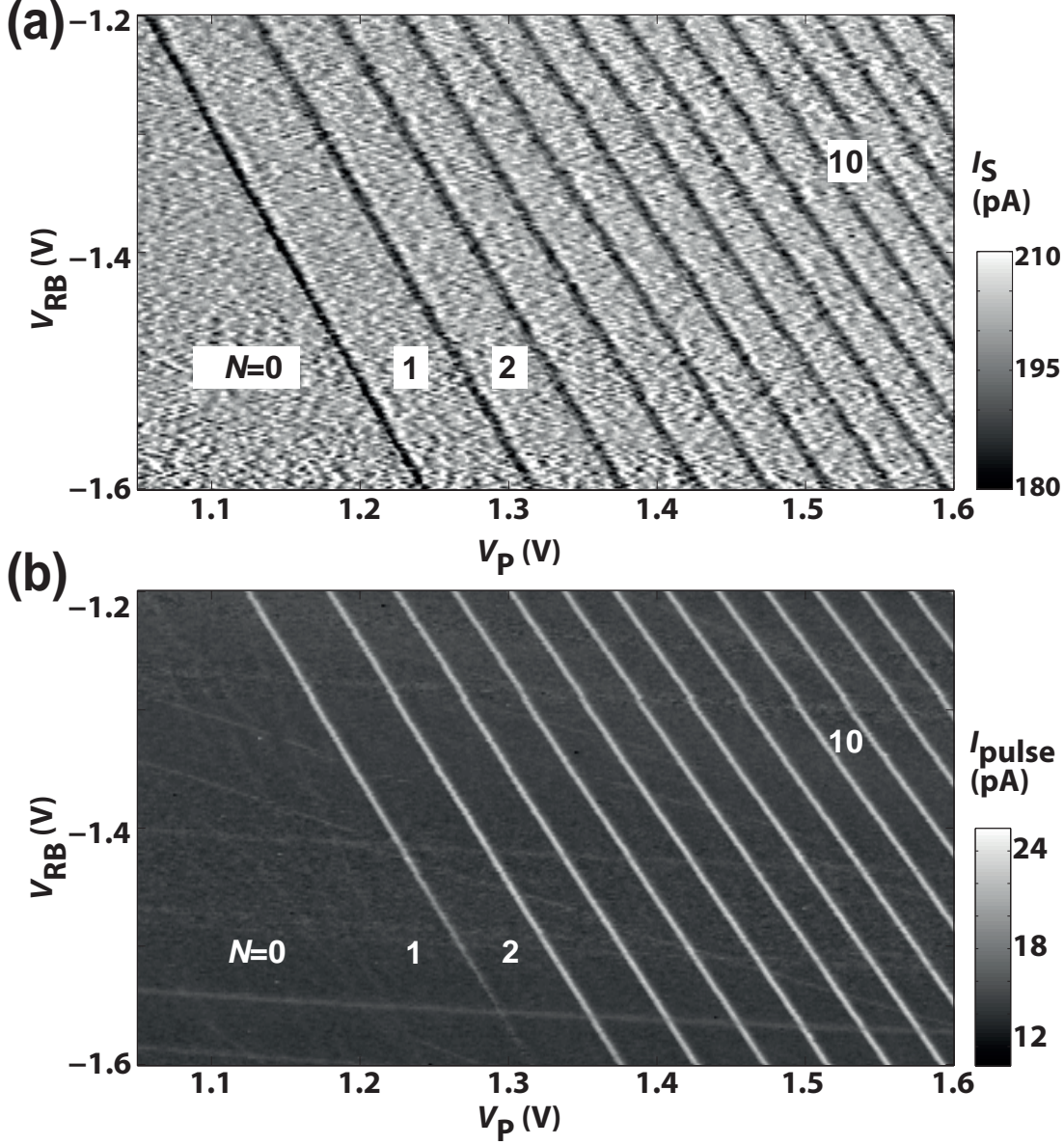


Figure 6.3: Charge Stability Diagram via Charge Sensor - (a) SET sensor lock-in current I_S vs. V_P and V_{RB} , mapping out the charge stability plot of the quantum dot. Dynamic compensation is applied to the SET sensor. (b) Measured pulse lock-in signal I_{pulse} from SET sensor with a symmetric square wave of peak-to-peak voltage $V_{\text{pulse}} = 2$ mV applied to dot plunger P at $f_{\text{pulse}} = 487$ Hz. The first charge transition is not visible because the tunnel rate into/out of dot is too low with respect to f_{pulse} .

6.3 Quantum Dot Occupancy and Measurement of Excited States

6.3 Quantum Dot Occupancy and Measurement of Excited States

Figure 6.3(a) shows the measured QD charge stability map as a function of right barrier gate voltage V_{RB} and plunger gate voltage V_P . As we reduce V_P , the number of electrons in the quantum dot is reduced one by one until we observe no more charge transitions in the stability map. The charging energy of the dot is around 10 meV for high occupancy and increases significantly (up to 20 meV) in the few-electron regime. This indicates that the dot size is dramatically affected by the number of electrons at low N and strongly suggests that we have achieved the few-electron regime. In light of this, we believe that the last transition observed is likely to be ascribed to the last electron ($N = 0$). Simultaneously, we measure the pulse lock-in detection signal I_{pulse} when a symmetric square wave with V_{pulse} of 2 mV and $f_{\text{pulse}}=487$ Hz is applied to gate P, and the resulting stability map is plotted in Figure 6.3(b). Identical charge transitions are detected using I_{pulse} , but with an improved signal-to-noise ratio compared with the sensor signal I_S plotted in Figure 6.3(a). This allows us to detect a number of extra transitions which are believed to originate from charge impurities nearby the sensor. Indeed, these features have different slopes with respect to the main ones and their signal strength is significantly reduced. This indicates that the originating charge displacement is elsewhere located in the substrate with respect to the gate-defined QD.

Towards the one-electron limit, as the dot potential well becomes shallower and the tunnel barrier widens, the tunnel rate decreases. Here, the tunnel rate for the first electron falls significantly below 974 Hz ($2 \times f_{\text{pulse}}$ Hz) and so the

6. EXCITED STATE SPECTROSCOPY OF ORBITAL AND VALLEY LEVELS

$N=0 \leftrightarrow 1$ transition is not visible in Figure 6.3(b). Although electron tunneling is allowed energetically (see Figure 6.3(a)), the high pulsing frequency used does not provide an electron with sufficient time to tunnel onto/off the dot. In this case, the tunneling time is longer than 1 ms.

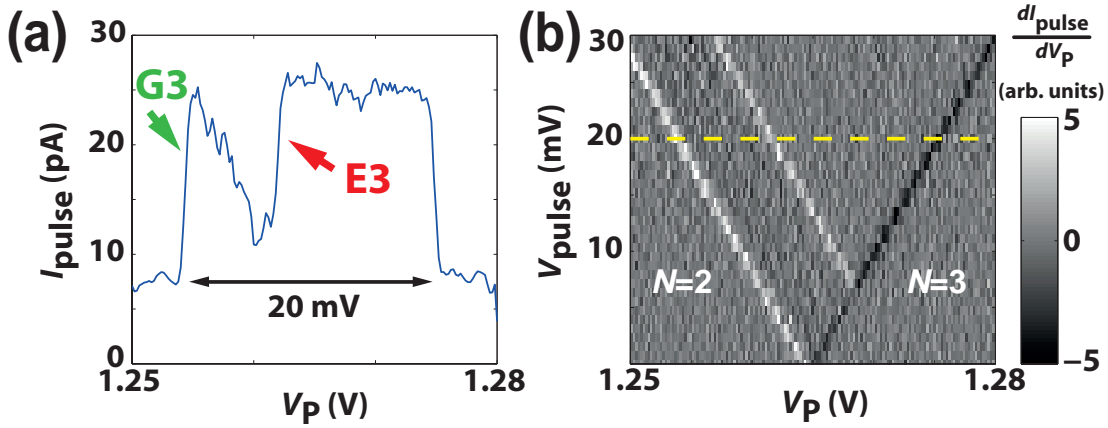


Figure 6.4: Observation of Excited state via Charge Sensor - (a) Lock-in detection signal, with $V_{\text{pulse}} = 20$ mV, at $f_{\text{pulse}} = 444$ Hz for $N = 2 \leftrightarrow 3$ transition, extracted along the yellow dashed line in (d) at $V_{\text{pulse}} = 20$ mV. The red arrow indicates the orbital excited state. (b) Derivative of the detection signal with respect to V_P . Orbital ground and excited states are observed at the loading edge as white parallel lines.

In order to observe the excited states of the dot, we increase V_{pulse} to 20 mV as shown in Figure 6.4(a, b) for the $N = 2 \leftrightarrow 3$ transition. The pulse lock-in signal I_{pulse} increases as soon as the three-electron ground state is pulsed below E_F (green arrow in Figure 6.4(a)). The signal then decays slowly with increasing V_P indicating a decrease in tunnel rate as the ground state moves away from resonance with the Fermi level. When the three-electron excited state is pulsed below E_F the tunnel rate rises rapidly again, resulting in a second increase in the detection signal (red arrow in Figure 6.4(a)). When we increase V_P further, so $N = 3$ at both pulse levels, the signal falls low again since the tunneling events

6.4 Orbital State Spectrum

are energetically forbidden due to Coulomb blockade. Figure 6.4(b) shows the derivative $dI_{\text{pulse}}/dV_{\text{P}}$ of the pulse lock-in detection signal as a function of V_{pulse} and V_{P} . The left white line represents the ground-state loading edge. The second white line in parallel with the ground state is the excited state loading edge, while the unloading edge appears as a black line. Here by loading (unloading) edge we refer to the potential configuration for which an electron can start to occupy an energy level in the upper phase of the pulse (not) being allowed to empty it during the lower phase.

6.4 Orbital State Spectrum

We next study in detail the orbital excited states for the first few electrons by increasing V_{pulse} to 40 mV and plotting the charge stability diagram of the dot as a function of V_{LB} and V_{P} in Figure 6.5(a). We identify these excited states as orbital states, as opposed to valley states, because their energies are much larger than the valley splitting in our device ($\sim 230 \mu\text{eV}$), as we shall show in the next section. In Figure 6.5(a), we have converted the pulse lock-in signal I_{pulse} to a corresponding average change of electron occupancy ΔN in the dot using a simple linear map. We identify $\Delta N = 1$ as the level where I_{pulse} saturates, which occurs when the tunnel rate significantly exceeds the pulse frequency f_{pulse} , as seen in Figure 6.4(a) at V_{P} beyond the E3 riser. Note that $\Delta N = 2$ where two transitions overlap, as the pulsing level exceeds the charging energy allowing occupancy to change by two electrons. The ground states and the orbital excited states of the first four electron transitions are highlighted by green and red lines, respectively. We also observe a decrease in tunnel rate as we decrease V_{LB} (thus

6. EXCITED STATE SPECTROSCOPY OF ORBITAL AND VALLEY LEVELS

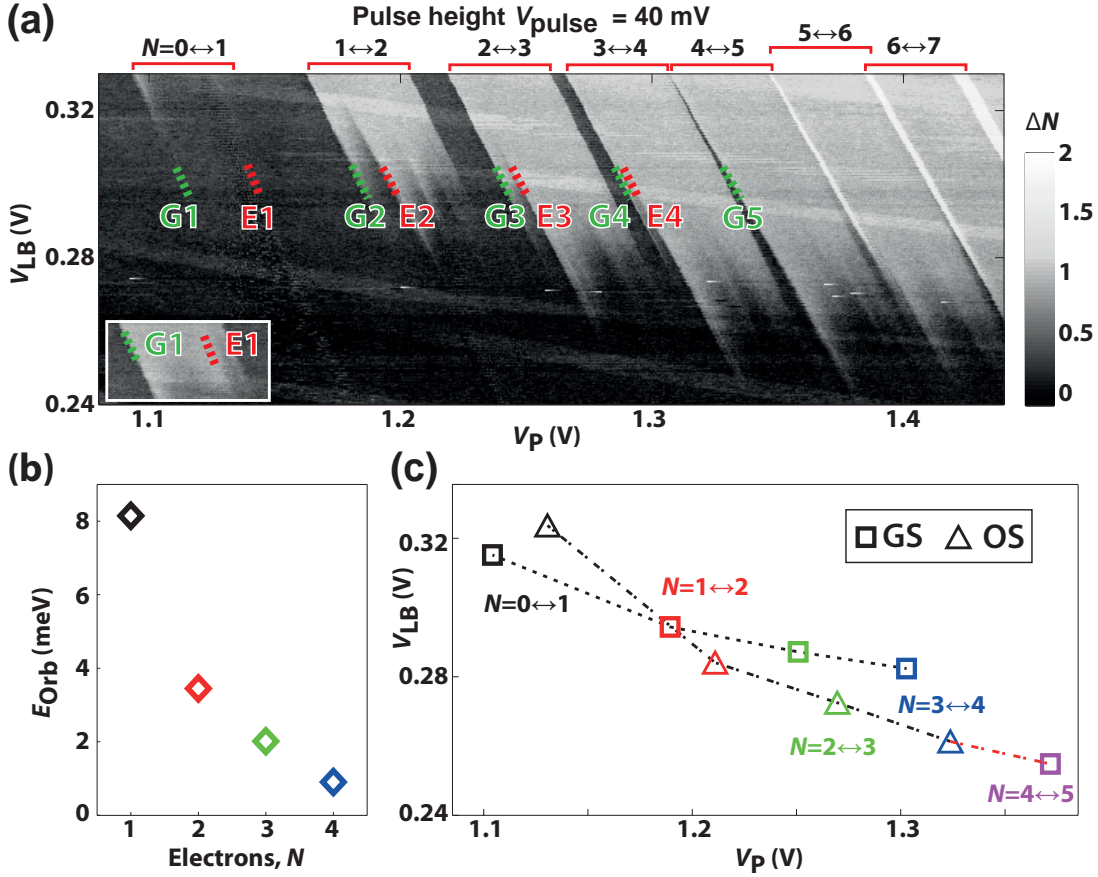


Figure 6.5: Excited state observation through pulse lock-in - (a) Lock-in signal from sensor S with $V_{pulse}=40$ mV at $f_{pulse}=487$ Hz applied to gate P, as a function of V_P and V_{LB} . Here we apply a linear scaling of the lock-in output to directly indicate the excess electron occupancy ΔN on the dot. INSET: different region focusing on the first transition shown to enhance visibility of both excited state and unloading edge. (b) Orbital excited-state energy of the first 4 electrons at $V_{LB}=0.3$ V. (c) Positions of $\Delta N = 0.5$ for ground states (GS) and first excited states (OS). These points are extracted from panel (a) where the tunnel rate from the reservoir to the dot is around 974 Hz.

6.5 Spin and Valley Level Filling

increasing the barrier height), resulting in $\Delta N \rightarrow 0$ as the tunnel rate falls below f_{pulse} . In Figure 6.5(b), we plot the first orbital excited state energy E_{Orb} with respect to the electron number N , extracted from Figure 6.5(a). Note that the energy conversion factor, $\alpha \sim 0.3 \text{ eV/V}$, is derived from considerations relevant to valley splitting measurements, as discussed next. As V_P is reduced, the dot becomes smaller leading to an increase in the orbital level spacing from 1 meV for $N = 4$, to 8 meV for $N = 1$.

In Figure 6.5(c), we plot the positions in gate voltage space (V_{LB} ; V_P) corresponding to $\Delta N = 0.5$ for the ground and orbital excited states $N = 1$ to 5. These are the points where the tunnel rates are comparable to the pulse frequency f_{pulse} . As the dot occupancy increases, a greater barrier height (or lower V_{LB}) is required to maintain a constant tunnel rate. We note that both the ground states (GS) and the orbital excited states (OS) follow regular trend lines, except for the $N = 5$ ground state, which appears more like an orbital excited state. This is due to the ground orbital levels being full with electrons and starting to fill the next orbital.

6.5 Spin and Valley Level Filling

We now study the spin filling of the first four electrons into the valley states of the quantum dot by examining the Zeeman shifts of the ground and excited states in a magnetic field parallel to the oxide interface in the range $-6 \text{ T} < B < 6 \text{ T}$, as shown in Figure 6.6(a). Here we set $V_{\text{pulse}} = 20 \text{ mV}$ and plot the derivative of the pulse lock-in current, dI_{pulse}/dV_P . The data reveals a number of levels, including spin ground and excited states, for what appear to be two distinct valley levels,

6. EXCITED STATE SPECTROSCOPY OF ORBITAL AND VALLEY LEVELS

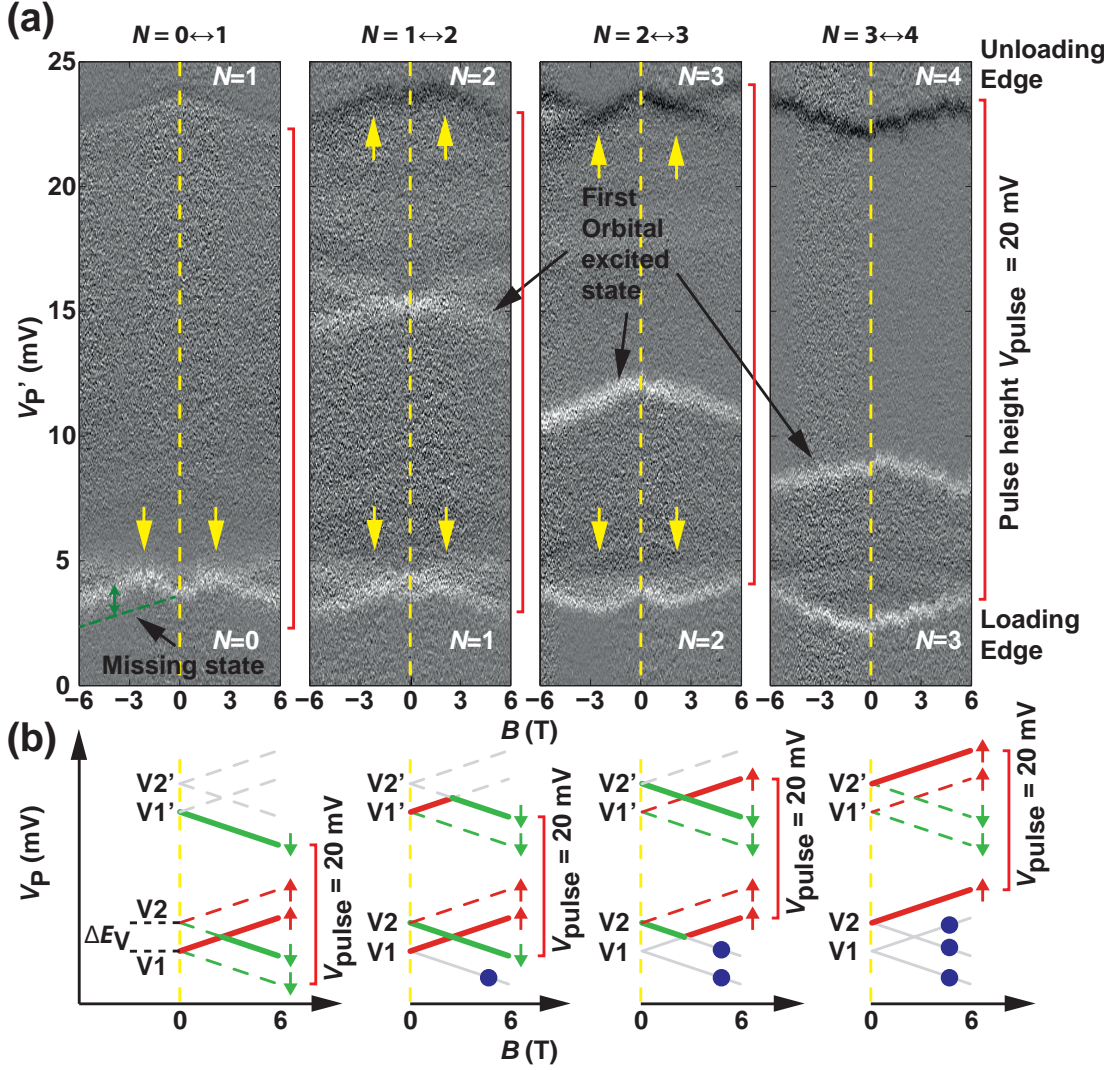


Figure 6.6: Magneto-spectroscopy of the first 4 electrons - (a) Grey-scale plot of the QD differential occupancy ($\Delta^2 N$) in magnetic field for the first 4 electron transitions at $V_{\text{pulse}} = 20$ mV and $f_{\text{pulse}} = 487$ Hz. Orbital excited states, Zeeman splittings and valley-orbit splitting are observed. V_p' represents arbitrarily shifted V_p . (b) Schematic of the evolution of two non-degenerate valley eigenstates for positive B -field. V_1 (V_1') and V_2 (V_2') represent loading (unloading) edge states. Each valley state Zeeman splits into two levels at finite B -fields. The blue dots represent already-occupied electron states.

6.5 Spin and Valley Level Filling

as we explain below.

We first consider the unloading edge of the charge transitions, which appear as dark lines in Figure 6.6(a). For the first transition ($N = 0 \leftrightarrow 1$), the unloading edge moves towards less positive V_P with increasing magnetic field $|B|$, indicating that the first electron is spin-down $|\downarrow\rangle$. Assuming that the g-factor = 2 for electrons in silicon and using the Zeeman energy equation $\frac{1}{2}g\mu_B B$, where μ_B is the Bohr magneton, we fit the energy change of the unloading edge. This results in a plunger gate voltage to energy conversion factor, $\alpha \sim 0.3$ eV/V. This is consistent with values for a similar quantum dot reported in Ref. [15]. Note that the evaluation of the α -factor from the Zeeman splitting is a robust approach in Si-based systems. Because of the weak spin-orbit coupling [117], only very small deviations (less than 1%) of the g-factor from the free-electron value are observed in Si, as opposed to the case of III-V semiconductors where much larger deviations are found. Next, we analyze the unloading edge of the second transition ($N = 1 \leftrightarrow 2$). The energy level first increases with magnetic field for $|B| < 2$ T, indicating that a spin-up electron was unloaded, and then decreases with $|B|$ above ~ 2 T. This indicates that the $N = 2$ ground state changes from a singlet $\frac{1}{\sqrt{2}}(|\downarrow\uparrow\rangle - |\uparrow\downarrow\rangle)$ at low B , to a triplet $|\downarrow\downarrow\rangle$ for $|B| > 2$ T. A similar kink at $|B| \sim 2$ T (marked by a yellow arrow) is observed for the third transition ($N = 2 \leftrightarrow 3$), although here the unloading edge moves downwards at low $|B|$ and then upwards at high $|B|$. Finally, the unloading edge of the fourth transition ($N = 3 \leftrightarrow 4$) rises linearly with $|B|$, consistent with a spin-up electron unloading for all magnetic fields up to 6 T.

In order to explain these data, we use a model based on two non-degenerate valley states (V_1, V_2) whose spin-states depend on B field according to the Zeeman

6. EXCITED STATE SPECTROSCOPY OF ORBITAL AND VALLEY LEVELS

energy equation (Figure 6.6(b)). This model relies on the fact that bulk silicon has six degenerate valleys, but when confined to two dimensions, such as a Si/SiO₂ interface, these separate into four valleys with high effective mass and two lower-energy Γ -valleys [87]. The Γ -valleys are also non-degenerate with a splitting $\Delta E_V = E_{V2} - E_{V1}$ that is typically well below 1 meV. In previous ground-state magneto-spectroscopy studies on a similar dot we found $\Delta E_V \sim 0.1$ meV [88], which we note is much smaller than the first orbital excited state energies ($E_{\text{Orb}} = 1\text{--}8$ meV) as long as dot occupancy is kept low ($N \leq 4$). From Figure 6.6(b), we see that the first electron fills the lower valley V_1 as spin-down for all B . When the second electron loads ($N = 1 \leftrightarrow 2$ transition) it will fill V_1 as spin-up at low values of $|B|$, forming a spin singlet $\frac{1}{\sqrt{2}}(|\downarrow\uparrow\rangle - |\uparrow\downarrow\rangle)$, however at large $|B|$, when the Zeeman energy exceeds the valley splitting ΔE_V , it will preferentially load into the upper valley V_2 as spin-down, to form a triplet state $|\downarrow\downarrow\rangle$. Moving to the third electron, we see that it will fill as spin-down in valley V_2 for low $|B|$, and then as spin-up in valley V_1 once the Zeeman energy exceeds ΔE_V . The fourth electron always fills as spin-up in valley V_2 , unless there is a nearby orbital state (within the Zeeman energy), which is likely to be the case for higher dot occupancy than currently reported ($N > 4$). In Figure 6.6(a) we can clearly see the orbital excited states (white lines) between the loading and unloading edges. They predominantly move downwards with the Zeeman energy, implying that they load spin-down electrons.

We find that the level crossings in Figure 6.6 (marked by yellow arrows) occur at $|B| \sim 2$ T for $N = 1..3$, indicating that the valley splitting $\Delta E_V = g\mu_B B \sim 230$ μeV remains approximately constant for small electron occupancy. This value is roughly double the valley splitting we observed in a previous device [88], most

6.5 Spin and Valley Level Filling

likely due to the larger electric fields employed in the present study [118]. The observation of a valley splitting that is independent of electron number confirms the prediction [66] that the valley exchange Coulomb integral is negligible.

The ground-state loading edges (lower white lines in Figure 6.6(a)) for transitions 2 to 4 show the same trends in magnetic field as the unloading edges. However, for the first transition ($N = 0 \leftrightarrow 1$) the ground state (marked by a green dashed line) is not visible. We know this state is present because the distance between the loading and unloading edge must equal $V_{\text{pulse}} = 20$ mV. We believe this is due to a very low (loading) tunnel rate, which we previously observed for low electron occupancy in Figure 6.5(a). Note that the observation of the spin excited state is compatible with the pulse frequency in use which is chosen to be higher than the relaxation rate. Indeed, the relaxation rate in the window of magnetic field applied is expected to be in the range 0.1 - 10 Hz [36, 92], whereas we use pulse sequences of few hundreds of Hz. This accounts for the kink at 2 T formed by the lower valley spin up state and the upper valley spin down state. Finally, we consider the $N = 5$ ground state, which has a tunnel rate that follows the trend for the orbital excited states for $N = 1$ to 4, as shown in Figure 6.5(c). We can now understand this in terms of a shell structure, where the first four electrons fill the spin and valley states of the lowest orbital, and the fifth electron occupies the next available orbital level. This is consistent with a shell structure of $N = 4$ observed in other silicon quantum dots [88, 89].

The origin of orbital and valley states are also described in Figure 2.14. As for the complete shell structure of a 2D QD, see Chapter 7 on descriptions of 2D Fock-Darwin states (Figure 7.3).

6. EXCITED STATE SPECTROSCOPY OF ORBITAL AND VALLEY LEVELS

6.6 Conclusions

In conclusion, we have demonstrated excited state spectroscopy of a nearly-closed silicon quantum dot using charge sensing and a pulsed-gating technique, thus enabling clear identification of the spin, valley and orbital states for the first four electrons. As the occupancy increased from $N = 1$ to 4 electrons, we found that the valley splitting for the lowest orbital level remained approximately constant at $230 \mu\text{eV}$, while the next orbital level energy decreased from 8 meV to 1 meV . Given the increasing interest in quantum information processing using spin and valley states in silicon quantum dots [66], it is important that the multi-valley level structure of these systems is well characterised experimentally.

6.6 Conclusions

6. EXCITED STATE SPECTROSCOPY OF ORBITAL AND VALLEY LEVELS

Chapter 7

Spin-Valley Lifetimes in a QD with Tunable Valley Splitting

This chapter demonstrates that valley separation can be accurately tuned via electrostatic gate control in a MOS QD, providing splittings spanning 0.3 - 0.8 meV. The splitting varies linearly with applied electric field, with a ratio in agreement with atomistic tight-binding predictions. We demonstrate single-shot spin readout and measure the spin relaxation for different valley configurations and dot occupancies, finding one-electron lifetimes exceeding 2 seconds. Spin relaxation occurs via phonon emission due to spin-orbit coupling between the valley states, a process not previously anticipated for silicon QDs.

An analytical theory describes the magnetic field dependence of the relaxation rate, including the presence of a dramatic rate enhancement (or hot-spot) when Zeeman and valley splittings coincide.

Parts of this chapter have been published in: C. H. Yang, A. Rossi, R. Ruskov, N. S. Lai, F. A. Mohiyaddin, S. Lee, C. Tahan, G. Klimeck, A. Morello and A. S. Dzurak, *Nature Communications* **4**, 2069 (2013). Rusko Ruskov and Charles Tahan from the Laboratory for Physical Sciences in Maryland are acknowledged for their development of the detailed theory explaining the spin-valley state mixing presented here in Section 7.4.

7. SPIN-VALLEY LIFETIMES IN A QD WITH TUNABLE VALLEY SPLITTING

7.1 Introduction

In order to define a robust spin- $1/2$ qubit Hilbert space, it is necessary that the energy scale of the two-level system is well separated from higher excitations. In this respect, a major challenge for the use of silicon is represented by the multi-valley nature of its conduction band. The Γ valley degeneracy is generally lifted by a sharp perpendicular potential [65, 118, 119, 120] and the relevant energy separation is termed the valley splitting (VS).

The valley splitting depends on physics at the atomic scale [121, 122, 123] (e.g. roughness, alloy and interface disorder), and so it is not surprising that experiments have revealed a large variability of splittings among devices, ranging from hundreds of μeV [67, 87, 124, 125] up to tens of meV in exceptional cases [68]. At present, the lack of a reliable experimental strategy to achieve control over the VS is driving an intense research effort for the development of devices that can assure robust electron spin qubits by minimising multi-valley detrimental effects [114, 126], or even exploit the valley degree of freedom [127, 128] for new types of qubits.

Another crucial parameter to assess the suitability of a physical system to encode spin-based qubits is the relaxation time of spin excited states (T_1). Spin lifetimes have been measured for gate-defined Si quantum dots (QDs) [92], Si/SiGe QDs [36, 129] and donors in Si [46], reporting values which span from a few milliseconds to a few seconds. Furthermore, the dependence of the spin relaxation rate (T_1^{-1}) on an externally-applied magnetic field (B) has been investigated. Different mechanisms apply to donors and QDs, accounting for observed $T_1^{-1} \propto B^5$ and B^7 dependencies [130], respectively. In principle, $T_1^{-1}(B)$ depends on the

7.2 Quantum Dot Occupancy and Shell Structure

valley configuration and the details of the excited states above the spin ground state. However, until now, no experimental observation of the effects of a variable VS on the relaxation rate has been reported.

In this chapter we show the first experimental demonstration that the valley splitting in a silicon QD can be finely tuned by direct control of an electrostatic gate potential. We find that the dependence of the VS on vertical electric field at the Si/SiO₂ interface is strikingly linear, and show that its tunability is in excellent agreement with atomistic tight-binding predictions. We demonstrate accurate control of the VS over a range of about 500 μeV and use it to explore the physics of spin relaxation for different QD occupancies ($N=1, 2, 3$). We probe both the regime where the VS is much larger than the Zeeman splitting at all magnetic fields and that where the valley and spin splittings are comparable. We observe a dramatic enhancement of the spin decay rate (relaxation hot-spot) when spin and valley splittings coincide. To our knowledge, such hot-spots have been predicted for relaxation involving orbital states [42, 47] (not valley states), but these are yet to be observed. An analytic theory that explains the B -field dependence of the relaxation rates and the details of the relaxation hot-spot in terms of admixing of spin-valley states is presented in Section 7.4. This mechanism is seen to be significantly more prominent than the conventional spin-orbit hybridisation [28].

7.2 Quantum Dot Occupancy and Shell Structure

Our device is fabricated using a multi-level gated metal-oxide-semiconductor (MOS) technology [14](Chapter 3.1), and its architecture is depicted in Fig-

7. SPIN-VALLEY LIFETIMES IN A QD WITH TUNABLE VALLEY SPLITTING

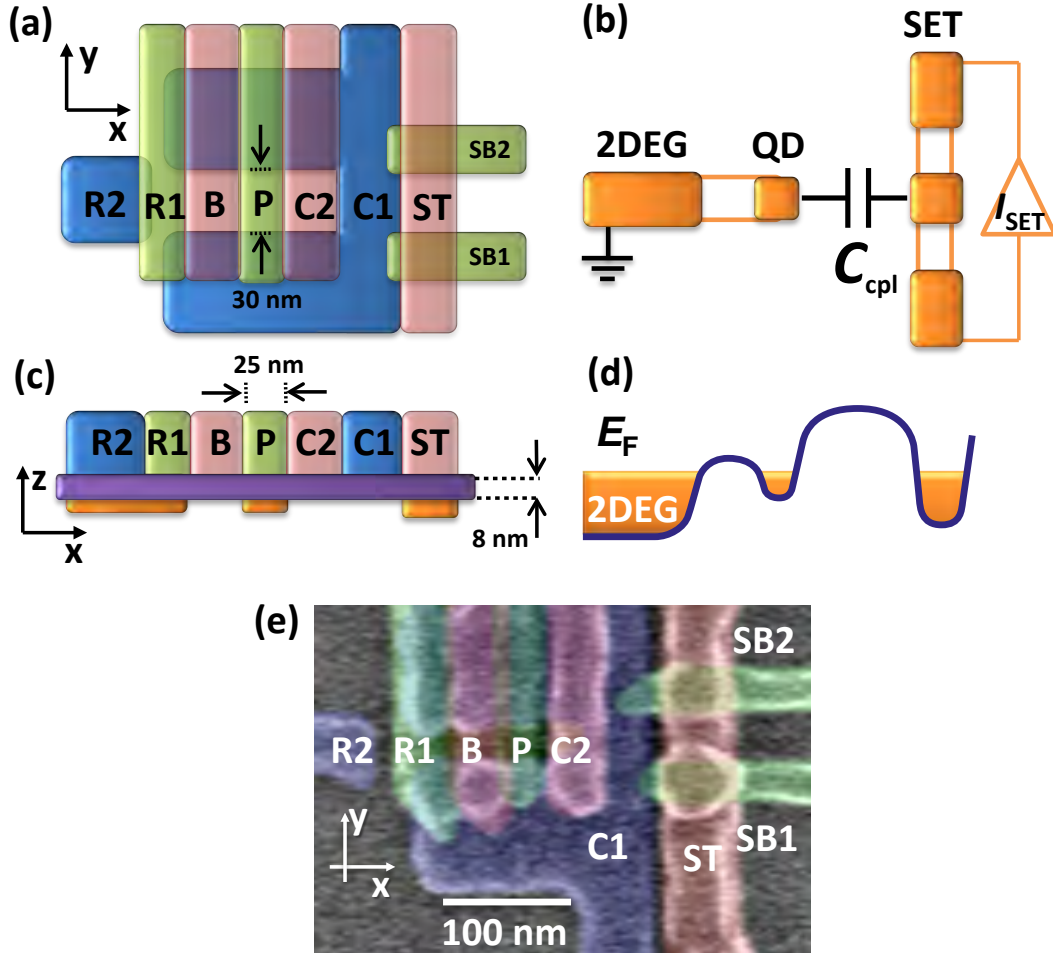


Figure 7.1: Device architecture - (a) Schematic (top view) of the device's gate layout. Different colours represent different layers within the gate stack. (b) Schematic diagram of the single-lead QD (left) and SET detector (right). Regions where an electron layer is formed are coloured in orange. The readout signal (I_{SET}) is sensitive to the QD charge state due to the QD/SET capacitive coupling (C_{cpl}). (c) Device cross-sectional schematic. An electron layer is formed underneath the positively biased gates: R1 and R2 define the QD reservoir; P controls the QD population; and ST the sensor's island. The SiO₂ layer (in purple) thickness and plunger gate width are indicated. (d) Energy diagram showing qualitatively the conduction band profile in the device. Electrons accumulate wherever the gate bias lowers the conduction band below the Fermi level, E_F . (e) Device SEM image with the corresponding color gates.

7.2 Quantum Dot Occupancy and Shell Structure

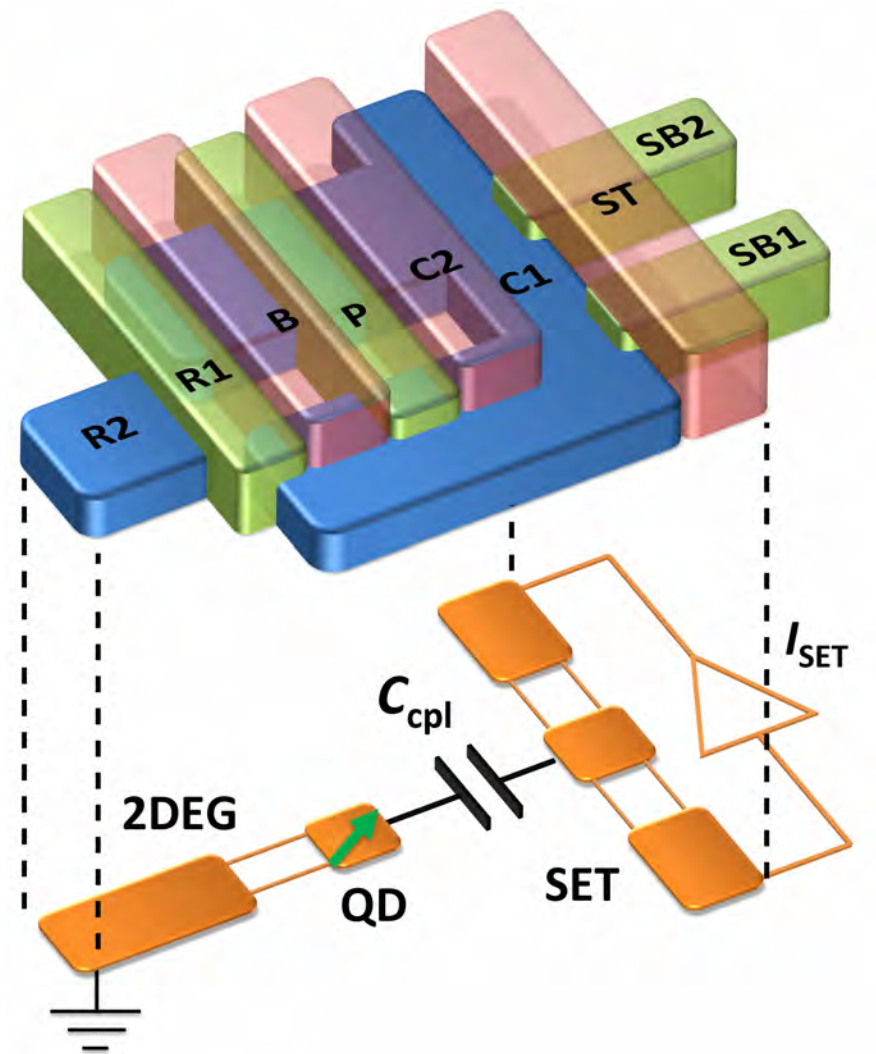


Figure 7.2: Device architecture 3D view - Schematic (3D view) of the device with gates and electron layers.

7. SPIN-VALLEY LIFETIMES IN A QD WITH TUNABLE VALLEY SPLITTING

ure 7.1(a)-(d), and Figure 7.2. A quantum dot is formed under gate P by applying a positive bias voltage to induce an electron accumulation layer. Strong planar confinement for the dot's potential well is achieved by negatively biasing gates B, C1 and C2. A 2DEG reservoir is also induced by positively biasing gates R1 and R2, and the QD occupancy can be modified by inducing electrons to tunnel between this reservoir and the dot. The remaining gates, namely SB1, SB2, ST, are employed to define a single-electron transistor (SET), capacitively coupled to the QD and used as a read-out device. The high flexibility of our design would allow us to use the same device also as a (single-lead) double dot structure by rearranging the gate bias (e.g. dots can be formed under gates B and C2). However, in this work, we only present results relevant to the single-dot configuration.

In order to characterise the addition spectrum of the QD, we make use of a technique previously developed for GaAs-based systems which combines charge detection and gate pulsing [33]. There is no direct transport through the single-lead QD and, therefore, addition/removal of charge is only detected via modifications in the SET current. In particular, charge transitions are detected as current peaks in the SET signal whenever the QD energy eigenstates come into resonance with the reservoir's Fermi level. Note that the SET-QD coupling is merely capacitive (via C_{cpl}) and electrons do not tunnel between them. In order to maximise charge sensitivity in the detector, we employ dynamic voltage compensation [116] on different gates which makes our read-out signal virtually unaffected by slow charge drifts and random charge rearrangements.

Figure 7.3(a) shows the measured stability map as a function of plunger gate voltage, V_P , and barrier gate voltage, V_B . Current peaks in the lock-in signal indicate the occurrence of charge transitions due to tunnelling between the QD

7.2 Quantum Dot Occupancy and Shell Structure

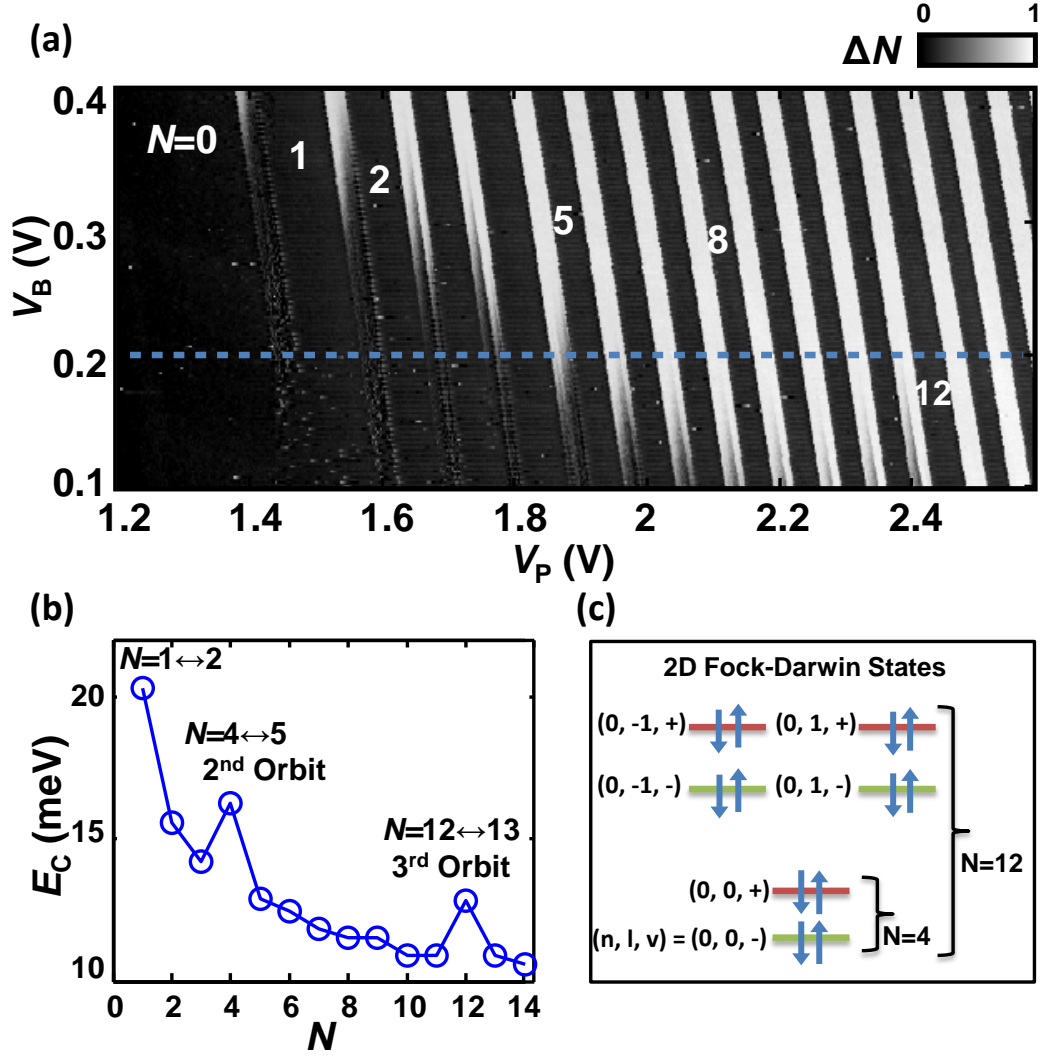


Figure 7.3: Filling energy of the QD - (a) Stability map as a function of plunger gate voltage, V_P , and barrier gate voltage, V_B . Current peaks in the lock-in signal indicate the occurrence of charge transitions due to tunnelling between the QD and the reservoir. (b) Charging energy across the blue dotted line in (a), as a function of electron number. Spikes corresponding to complete 2D shell filling are observed. (c) Schematic of electron filling for two-valley 2D Fock-Darwin states. Each state can hold two electrons of antiparallel spin and is identified by a pair of quantum numbers (n, l) and its valley occupancy (v) .

7. SPIN-VALLEY LIFETIMES IN A QD WITH TUNABLE VALLEY SPLITTING

and the reservoir. We have converted this signal into an average change of occupancy [131], ΔN , which is shown in the grey-scale plot. For each transition, we can also probe the first orbital excited state whenever a slow decrease in the detection signal is followed by a steep rise [131]. We observe charge additions for the first fourteen electrons in the dot. We determine the voltage to energy conversion factor, α , for gate P via temperature dependence measurement on charge transitions and we find $\alpha \approx 0.16$ eV/V.

Figure 7.3(b) illustrates the addition energy spectrum for the first fourteen electron additions to the QD, from the dashed horizontal line where $V_B=0.2$ V. There is very little variation of charging energy (E_C) for high occupancies ($E_C \approx 11$ meV for $N > 9$). However, by decreasing the electron number, the charging energy steadily increases, as expected when the dot size is significantly affected by the electron number. This evidently indicates that the few-electron regime has been achieved. Most interestingly, the energy spectrum shows peaks for the addition of the 5th and 13th electrons. The extra addition energy needed for those transitions can be attributed to complete filling of the first and second orbital shells. As illustrated in Figure 7.3(c), this is consistent with the energy spectrum of two-valley 2D Fock-Darwin states [49], where the first and second orbital shells hold 4 and 8 electrons respectively. This confirms that we can probe the occupancy until the last electron. To our knowledge, such a clear manifestation of two-dimensional shell structure has been observed before only in InGaAs dots [48] and in Si/SiGe dots [89].

7.3 Single-Shot Spin Readout and Spin-Valley Lifetimes for $N = 1$ Electron

7.3 Single-Shot Spin Readout and Spin-Valley Lifetimes for $N = 1$ Electron

In order to measure the spin state of individual electrons in the QD, we use an energy-selective readout technique [106]. In our experiments the B -field is directed along the [110] crystallographic axis. The readout protocol consists of three phases clocked by a three-level pulsed voltage applied to gate P, which directly controls the dot's electrochemical potential (see Figure 7.4 (a)).

Firstly, an electron of unknown spin is loaded into the dot causing a sudden decrease in the sensor current. Next, the potential of the dot is lifted so that the Fermi level of the reservoir lies between the spin-up and spin-down states of the dot, meaning that a spin-up electron can tunnel off the dot while a spin-down electron is blocked. This is the read phase, during which the presence of a spin-up state would be signalled by a current transient (spin-up tunnels out and then spin-down tunnels in) whereas a spin-down electron would lead to no current modification. Finally, the dot's potential is further lifted to allow the electron to tunnel off, regardless of its spin orientation. In Figure 7.4 (b) single-shot traces for both spin-up (in blue) and spin-down (in green) detection are plotted. The longer the system is held in the load phase before performing a read operation, the more likely it is for the spin-up excited state to decay to the spin-down ground state.

Figure 7.4 (c) shows the QD occupancy averaged over 256 single-shot traces for varying read levels at $B=3\text{T}$ (note that the energy scale on the y-axis is the effective shift of the dot's potential). This detection of a spin-up electron transient is seen to extend for about $350\mu\text{eV}$, as expected from the Zeeman equation,

7. SPIN-VALLEY LIFETIMES IN A QD WITH TUNABLE VALLEY SPLITTING

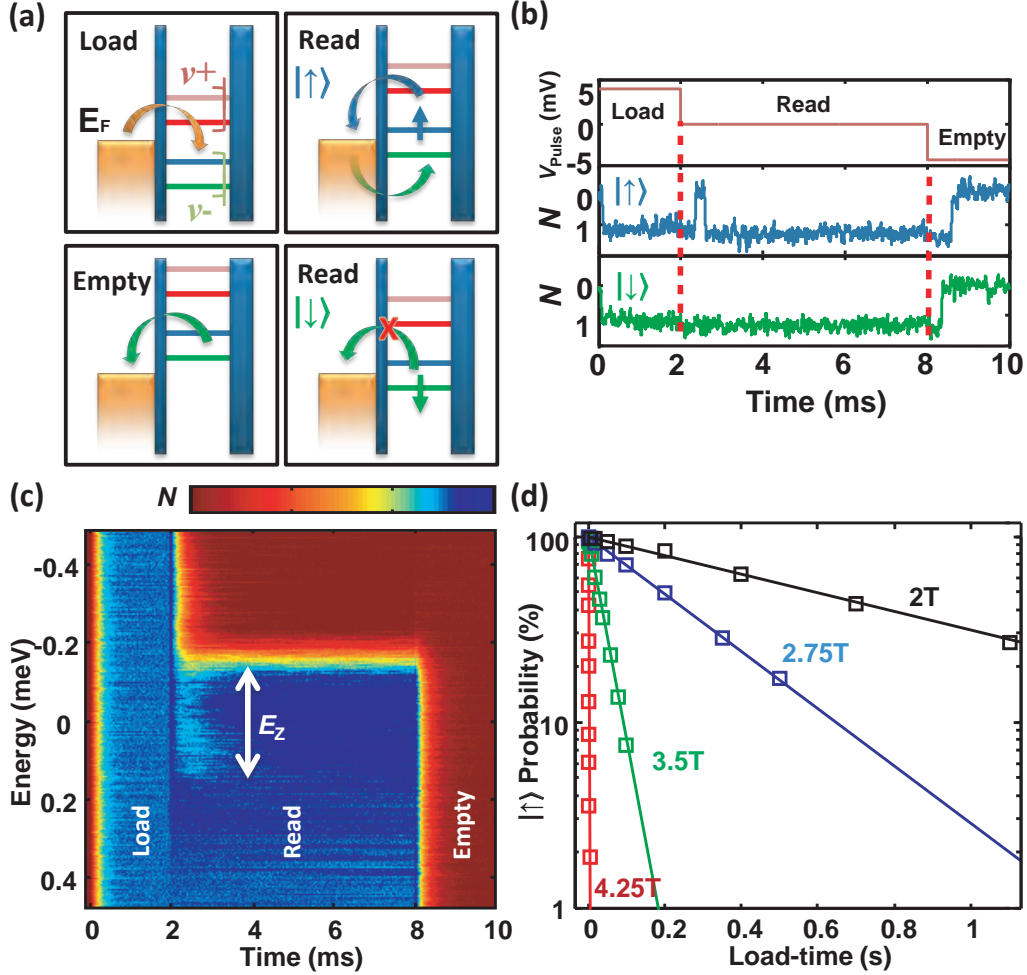


Figure 7.4: Spin readout for single-electron occupancy. - (a) Schematic diagram showing the effect of the 3-level pulse sequence on the electro-chemical potential of the dot. Energy levels in the QD are Zeeman split according to spin polarisation and valley degeneracy is lifted. For clarity, only lower valley states are shown to be loaded/unloaded. (b) Pulsing sequence (top) for the single-shot spin readout and normalised SET signal for spin-up (middle) and spin-down (bottom). (c) QD occupancy averaged over 256 single-shot traces for varying read levels at $B=3T$. (d) Fitted spin-up probability with various B field, then extracted as spin lifetime.

7.3 Single-Shot Spin Readout and Spin-Valley Lifetimes for $N = 1$ Electron

$E_Z = g\mu_B B$, by assuming $g = 2$. The field dependence of the measured $E_Z(B)$ also shows good agreement with the Zeeman equation. This proves that we can reliably load/unload electrons onto spin-split single-particle states. Thus, by varying the length of the load phase and monitoring the probability of detecting a spin-up electron, we can determine [46, 106] the spin lifetime, T_1 , as shown in Figure 7.4 (d).

As shown in Figure 7.5 (b), we observe a wide range of spin lifetimes as a function of magnetic field, with lifetimes as long as 2.6s at the lowest fields studied, $B=1.25\text{T}$. These are some of the longest lifetimes observed to date in silicon quantum dots [130].

A key focus of our experiment was to electrostatically tune the valley energy separation and measure relaxation rates in different valley configurations and QD electron occupancies. *As we show below, our data definitively indicate that excited valley states play a critical role in the spin relaxation processes.* We develop a theory to explain how changes in the valley splitting affects the spin-valley state mixing and leads to the observed relaxation times.

As we detail in Section 7.6, we have attained accurate gate control of the valley splitting, allowing us to tune it over a range of hundreds of μeV . This permits us to conduct experiments in regimes where the valley splitting (E_{VS}) is either larger or smaller than the Zeeman spin splitting (E_Z), depending on the magnitude of the magnetic field (see Figure 7.5 (a)).

Figure 7.5 (b) presents measurements of spin relaxation rates as a function of magnetic field for two valley splitting values at a fixed dot population of $N = 1$. We start by examining a configuration where the valley separation is larger than the spin splitting at all fields (green data set). In other words, we operate in a

7. SPIN-VALLEY LIFETIMES IN A QD WITH TUNABLE VALLEY SPLITTING

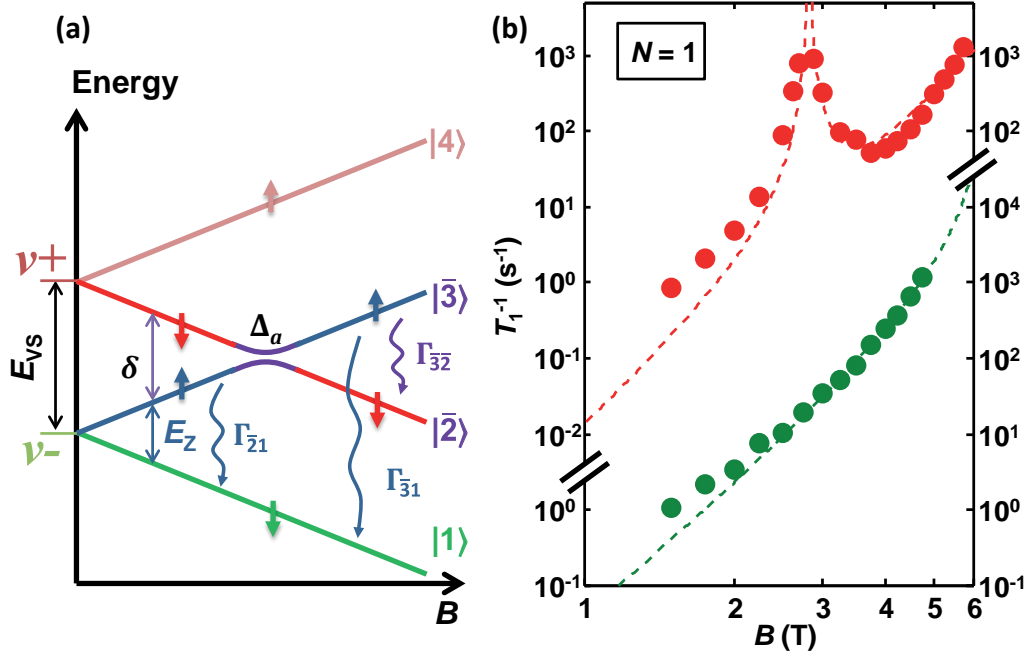


Figure 7.5: Energy spectrum and spin relaxation rates for single-electron occupancy. - (a) Energy diagram of the 1-electron spin-valley states as a function of B -field. Maximum mixing of spin and valley degrees of freedom occurs at the anticrossing point where Zeeman and valley splittings coincide. Relevant relaxation processes are sketched. (b) Relaxation rates as a function of magnetic field for different valley splittings. Data points for $E_{VS} = 0.75$ meV, $E_{VS} = 0.33$ meV are shown as green and red circles, respectively. Dashed lines are the calculated relaxation rates fitted with $r = 1.7$ nm (green), $r = 1.1$ nm (red).

7.4 Theory of Spin-Valley Mixing in a Silicon QD

regime for which

$$E_{VS} > E_Z = g\mu_B B \quad (7.1)$$

where g is the electron gyromagnetic ratio, μ_B is the Bohr magneton and B is the applied in-plane magnetic field.

For $E_{VS}=0.75$ meV (green data in Figure 7.5 (b)), we observe a monotonic increase of the rate with respect to B that becomes increasingly fast as E_Z approaches E_{VS} . In our experimental conditions (B -field parallel to $[110]$), the $T_1^{-1} \propto B^5$ dependences for known bulk-like mechanisms in silicon [43, 132] should not apply, while predicted [44, 47, 129, 130] rates $\propto B^7$ do not explain the experimental data.

By decreasing the valley separation to $E_{VS}=0.33$ meV, we can achieve the condition where the Zeeman splitting matches or exceeds the valley splitting. The red data in Figure 7.5 (b) illustrate the situation where inequality (1) only holds for $B < 2.8$ T. When $E_Z = E_{VS}$ (i.e. for $B=2.8$ T), a spike in the relaxation rate occurs. Relaxation hot-spots have been previously predicted to occur for spin relaxation involving orbital states in single and coupled QDs [42, 47, 133, 134]. To our knowledge, this is the first experimental observation of such a phenomenon, where the valley excited state is dominantly affecting the spin relaxation time around the hot-spot, and creates a more complicated field dependency on T_1 .

7.4 Theory of Spin-Valley Mixing in a Silicon QD

In order to understand the relaxation mechanisms, we developed a model that takes into account the perturbations in pure spin states due to spin-orbit coupling

7. SPIN-VALLEY LIFETIMES IN A QD WITH TUNABLE VALLEY SPLITTING

(SOC), yielding eigenstates which are admixtures of spin and valley states. The four lowest spin-valley states [(see Figure 7.5(a)) are defined as $|1\rangle = |v_-, \downarrow\rangle$, $|2\rangle = |v_-, \uparrow\rangle$, $|3\rangle = |v_+, \downarrow\rangle$, $|4\rangle = |v_+, \uparrow\rangle$. These states are considered to be only very weakly affected by higher excitations, such as orbital levels which are at least 8 meV above the ground state in our device in Chapter 6 [131]. In [37] supplementary note, we detail how mixing to a $2p$ -like orbital state leads to a B^7 dependence in T_1^{-1} and is, therefore, important mainly for high B -fields (above the anticrossing point). At lower fields, the prominent mechanism is the spin-valley admixing, which we now discuss in detail.

The relaxation between pure spin states is forbidden because the electron-phonon interaction does not involve spin flipping. However, in the presence of interface disorder, SOC can mix states that contain both the valley and spin degrees of freedom, thus permitting phonon-induced relaxation. Indeed, in the non-ideal case of QDs with a disordered interface, roughness can perturb the envelope function of both valleys (otherwise identical for ideal interfaces) and allows one to assume non-zero dipole matrix elements connecting the valley states (see [37] supplementary note), such as $\mathbf{r}_{-+} \equiv \langle v_- | \mathbf{r} | v_+ \rangle$, $\mathbf{r}_{--} \equiv \langle v_- | \mathbf{r} | v_- \rangle$, $\mathbf{r}_{++} \equiv \langle v_+ | \mathbf{r} | v_+ \rangle$ (for ideal interfaces these are non-zero only due to a strongly suppressed Umklapp process). By means of perturbation theory, we define renormalised excited states $|\bar{2}\rangle$ and $|\bar{3}\rangle$ that can relax to the ground state $|1\rangle$, as they have an admixture of the state $|3\rangle$ of the same spin projection (see Figure 7.5(a)). The details of the SOC Hamiltonian, H_{SO} , and perturbation matrix are reported in the [37] supplementary note. The leading order wavefunctions are given by:

$$|\bar{2}\rangle^{(0)} = \sin\frac{\gamma}{2} |2\rangle - \cos\frac{\gamma}{2} |3\rangle \quad (7.2)$$

7.4 Theory of Spin-Valley Mixing in a Silicon QD

$$|\bar{3}\rangle^{(0)} = \cos\frac{\gamma}{2} |2\rangle + \sin\frac{\gamma}{2} |3\rangle \quad (7.3)$$

where $\cos\frac{\gamma}{2} \equiv [\frac{1+a}{2}]^{1/2}$, $\sin\frac{\gamma}{2} \equiv [\frac{1-a}{2}]^{1/2}$, and $a \equiv -\delta/\sqrt{\delta^2 + \Delta_a^2}$ is an expression involving the detuning from the anticrossing point, $\delta \equiv E_{VS} - E_Z$, and the energy splitting at the anticrossing:

$$\Delta_a = 2|\langle v_-, \uparrow | H_{SO} | v_+, \downarrow \rangle| = r_- + \frac{m_t E_{VS}}{\sqrt{2}\hbar} (\beta_D - \alpha_R) \quad (7.4)$$

where β_D (α_R) is the Dresselhaus (Rashba) SOC parameter, \hbar is the reduced Planck's constant and $m_t = 0.198m_e$ is the transverse effective electron mass.

By evaluating the relaxation rate via the electron-phonon deformation potentials (proportional to the deformation potential constants, $\Xi_{d,u}$), we obtain the rate below the anticrossing as:

$$\Gamma_{\bar{2}1} = \cos^2\frac{\gamma}{2} \Gamma_{v'v} = \frac{\sqrt{\delta^2 + \Delta_a^2} - \delta}{2\sqrt{\delta^2 + \Delta_a^2}} \Gamma_{v'v} \quad (7.5)$$

where the pure valley relaxation rates are (for longitudinal and transverse phonons):

$$\Gamma_{v'v}^{(\sigma)} [\Delta E_{v'v}, \mathbf{r}] = \frac{\Delta E_{v'v}^5}{4\pi\rho\hbar^6} \frac{r^2}{v_\sigma^7} I^{(\sigma)} \quad (7.6)$$

where ρ is the silicon mass density, v_σ is the speed of sound in silicon, $I^{(l)} = 4[\frac{\Xi_u^2}{35} + \frac{2\Xi_u\Xi_d}{15} + \frac{\Xi_d^2}{3}]$, $I^{(t)} = \frac{16}{105}\Xi_u^2$ are the angular integrals, and $\Delta E_{v'v}$ and \mathbf{r} are the energy difference and the dipole matrix element relevant to the transition, respectively (see also [37] supplementary note). The experimental condition for which the hot-spot occurs (i.e. $E_{VS} = E_Z$) is modelled as an anticrossing point for the mixed states $|\bar{2}\rangle$ and $|\bar{3}\rangle$. At that point, spin relaxation is maximised and $\Gamma_{\bar{2}1}$ approaches the valley relaxation rate, as $\delta \rightarrow 0$ in Equation (7.5).

7. SPIN-VALLEY LIFETIMES IN A QD WITH TUNABLE VALLEY SPLITTING

Above the anticrossing (i.e. $E_{VS} < E_Z$), the relevant relaxation transitions are $|\bar{3}\rangle \rightarrow |1\rangle$ and $|\bar{3}\rangle \rightarrow |\bar{2}\rangle$ (the subsequent decay $|\bar{2}\rangle \rightarrow |1\rangle$ is in the form of a fast inter-valley transition and is, therefore, neglected). The analytical formulations of these contributions read:

$$\Gamma_{\bar{3}1} = \sin^2 \frac{\gamma}{2} \Gamma_{v'v} = \frac{\sqrt{\delta^2 + \Delta_a^2} + \delta}{2\sqrt{\delta^2 + \Delta_a^2}} \Gamma_{v'v} \quad (7.7)$$

$$\Gamma_{\bar{3}\bar{2}} = \sin^2 \frac{\gamma}{2} \cos^2 \frac{\gamma}{2} \Gamma_{v'v} [\Delta E_{v'v}, \mathbf{r}_{--} - \mathbf{r}_{++}] \quad (7.8)$$

The dashed lines in Figure 7.5(b) show the calculated relaxation rates relevant to the two experimental values of E_{VS} discussed, including also B^7 contribution from SOC mixing with the higher orbital state (see [37] supplementary note). We use dipole matrix elements as a single free parameter by assuming $|\mathbf{r}_{-+}| \simeq |\mathbf{r}_{--} - \mathbf{r}_{++}| \equiv r$. A least-square fit to the experimental data is performed by fixing the SOC strength to $(\beta_D - \alpha_R) \approx 45 - 60$ m/s (justified by the high electric field $\approx 3 \times 10^7$ V/m, see References [135, 136]). The fit then extracts a dipole size $r \approx 1-2$ nm for both values of E_{VS} .

The good agreement between the calculations and experiment, as well as the presence of a hot-spot at the point of degeneracy between Zeeman and valley splitting, provide strong evidence of our ansatz that the spin relaxation is predominantly due to a *new mechanism*: that of mixing with the excited valley states via Rashba/Dresselhaus-like SOC in the presence of interface disorder.

Both the splitting at the anticrossing, Equation (7.4), and the intervalley relaxation, Equation (7.6), depend crucially on the size of the dipole matrix element, r , predicting a fast phonon relaxation of $\approx 10^7 - 10^8$ s⁻¹ for $r = 1-3$ nm, at the hot-spot of Figure 7.5(b). This confirms our core findings that when spin-

7.5 Spin-Valley Relaxation for $N = 2$ Electron States

valley states anticross, the inter-valley rates are fast for these samples, with the only available relaxation mechanism being the inter-valley decay. We point out that these relaxation rates are expected to be sample/material-dependent, given the effect of interface disorder on valley mixing.

7.5 Spin-Valley Relaxation for $N = 2$ Electron States

We now examine the case $N = 2$ electrons, and investigate the dependence of the relaxation rate on the magnetic field at a fixed valley splitting ($E_{VS}=0.58$ meV). We note that the energy levels accessible for loading the second electron in the dot, when the $N = 1$ spin-down ground state is already occupied, are either the singlet (S) or the two lower triplets (T_-, T_0), while the higher triplet (T_+) would require a spin-flip and is, therefore, not readily accessible (see Figure 7.6(a)). In general, for triplet states, the antisymmetry of the two-electron wavefunction requires one electron to occupy a higher energy state. For our multi-valley QD (Figure 7.3 (c)), this requirement is fulfilled when the two electrons occupy different valley states [(see Figure 7.6 (a)). For low fields, the ground state is S and the triplets have higher energies. This results in excited states (triplets) that extend over two valleys and relax to single-valley ground state (singlet).

As the magnetic field is increased, S and T_- undergo an avoided crossing ($B \equiv B_{ST}$), and then T_- becomes the ground state. We adjust the levels of our pulsed readout protocol so that, during the load phase only S and T_- are below the reservoir's Fermi energy, while, during the read phase, the Fermi energy is positioned within the singlet-triplet (ST) energy gap. As a consequence, for

7. SPIN-VALLEY LIFETIMES IN A QD WITH TUNABLE VALLEY SPLITTING

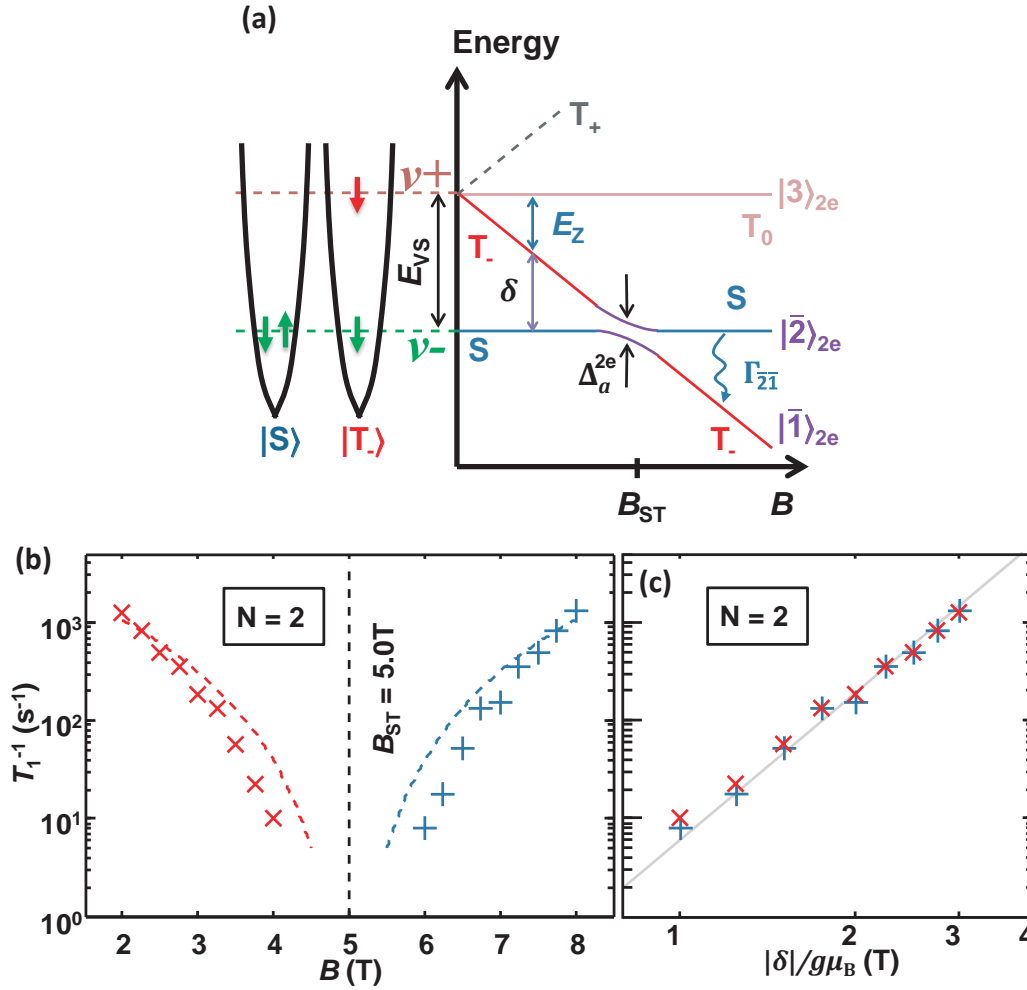


Figure 7.6: Spin-valley relaxation for 2-electron occupancy. - (a) Energy diagrams of the 2-electron spin-valley states in the dot’s potential well (left) and as a function of B -field (right). Dashed line indicates that T_+ is not accessible (see text). (b) Relaxation rate as a function of B -field for $N = 2$ and $E_{\text{VS}} = 0.58\text{meV}$. Red (blue) crosses represent data points at fields smaller (larger) than the anticrossing point. Dashed lines are the calculated rates fitted with $r^{2e}=4.76$ nm. (c) Data from the (b) re-plotted as a function of the modulus of the detuning energy, δ .

7.5 Spin-Valley Relaxation for $N = 2$ Electron States

$B < B_{ST}$ ($B > B_{ST}$) a T_- (S) state would be signalled with a current transient, and relaxation rates can be extracted as for the $N = 1$ occupancy. The experimental relaxation rates in Figure 7.6(b) show a strongly non-monotonic behaviour, approaching an absolute minimum at the anticrossing point ($B_{ST}=5T$). The trend is strikingly symmetric, as can be appreciated when T_1^{-1} is plotted against the detuning energy, as shown in Figure 7.6 (c). This symmetry is reflected in the QD energy spectrum (Figure 7.6(a)), as far as the detuning δ is concerned. For $B < B_{ST}$, the ST energy gap decreases with increasing B , resulting in slower relaxation rates. By contrast, for $B > B_{ST}$, the ST energy gap increases for increasing field, and so does the relaxation rate.

As opposed to the 1-electron case, we note that the 2-electron eigenstates anticrossing leads to a *minimum* in the relaxation rate (*cold-spot*), defined by a splitting at the anticrossing, Δ_a^{2e} , of the same order as that of Equation (7.4) (see Figure 7.6(a) and [37] supplementary note). The occurrence of this minimum does not strictly depend on the nature of the states involved in the decay (spin-like, valley-like, orbital-like or admixtures). It is due to the fact that the avoided crossing takes place between the ground and the first excited state, while for the case $N=1$ it involves the first and the second excited states without affecting the ground state.

To model the 2-electron case, we build the wavefunctions for S and T_- from the single-particle states by considering the Coulomb interaction as a perturbing averaged field. The corresponding states are defined as $|1\rangle_{2e} = |v_-, v_-, S\rangle$, $|2\rangle_{2e} = |v_-, v_+, T_- \rangle$. Next, the additional perturbation given by SOC leads to

7. SPIN-VALLEY LIFETIMES IN A QD WITH TUNABLE VALLEY SPLITTING

renormalised eigenstates which are admixtures of singlet and triplet:

$$|\bar{1}\rangle_{2e}^{(0)} = \sin\frac{\gamma}{2} |1\rangle_{2e} - \cos\frac{\gamma}{2} |2\rangle_{2e} \quad (7.9)$$

$$|\bar{2}\rangle_{2e}^{(0)} = \cos\frac{\gamma}{2} |1\rangle_{2e} + \sin\frac{\gamma}{2} |2\rangle_{2e} \quad (7.10)$$

being similar forms to Equation (7.2) (7.3). As we show in the [37] supplementary note, by evaluating the electron-phonon Hamiltonian matrix element for the transition between these states, one finds that it coincides in its form with its 1-electron counterpart for $|\bar{3}\rangle_{1e} \rightarrow |\bar{2}\rangle_{1e}$. Therefore, we can conclude that the corresponding relaxation rate, Γ_{21}^{2e} , has the same functional form as those derived in Equation (7.8), although the matrix elements for the two cases will be different ([37] supplementary note). Dashed lines in Figure 7.6 (b) represent the calculated rates which are fitted to the experimental data similarly to the case $N = 1$. Once again, the model convincingly reproduces the main features of the experimental trend, in particular the rates for fields away from the anticrossing together with the symmetry of the characteristics with respect to B_{ST} . Further work may be needed to improve the fit in the vicinity of the anticrossing point.

We also measured the relaxation rates for $N = 3$ electrons. When the QD occupancy is set at $N=2$, the lower valley is fully occupied and for low B -fields the ground state is a singlet. In this condition, the readout protocol is adjusted to probe spin relaxation within the upper valley upon loading/unloading of the third electron. By keeping $E_{VS} = 0.58\text{meV}$ and using the same methodology described before, we measure relaxation rates for the third electron spin state. We find that there is no significant difference between the spin relaxation rates for $N = 3$ and $N = 1$, as shown in Figure 7.7. Two main conclusions can be drawn

7.5 Spin-Valley Relaxation for $N = 2$ Electron States

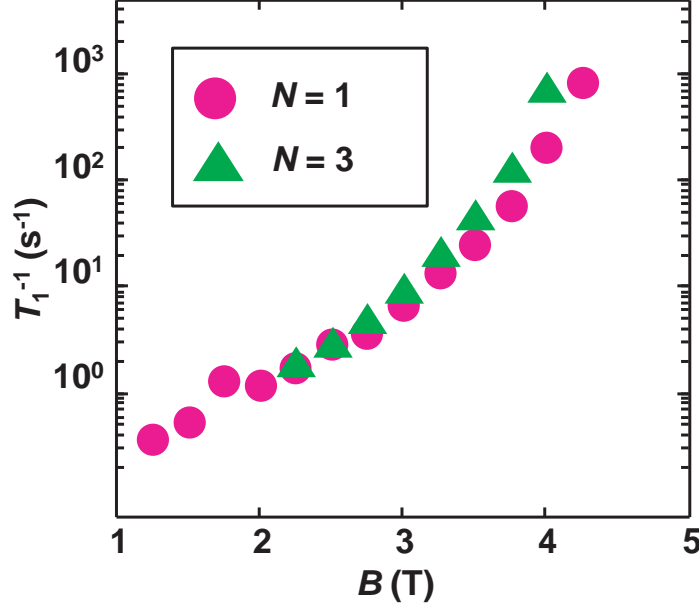


Figure 7.7: Spin-valley relaxation for 3-electron occupancy. - Relaxation rate as a function of B -field for $N = 3$ and $E_{VS} = 0.58\text{meV}$. Results for $N = 1$ are also shown for comparison.

from this. Firstly, we can infer that the effect of electron-electron interactions on the multi-valley spectrum may be negligible [137], which is plausible. Indeed, for valley 3-electron states, two electrons are just ‘spectators’, so that the remaining electron establishes the same energy level structure as in Figure 7.3 (b), and the Coulomb corrections should not affect the valley splitting. Secondly, as we report in Reference [131], in small QDs for higher occupancies a significantly reduced energy separation between the ground state and the first excited orbital state is observed. This would introduce a non-negligible perturbation on the relaxation if this were affected by the orbital degree of freedom. Hence, the similarities in behaviour in terms of decay rates are a further indication that for our QD the dominant relaxation mechanism resides in the degree of spin-valley admixing, as opposed to the spin-orbit admixing relevant for other semiconductor systems [28].

7. SPIN-VALLEY LIFETIMES IN A QD WITH TUNABLE VALLEY SPLITTING

7.6 Valley Splitting Control via Electric Field Tuning

We now turn to the experimental demonstration of accurate control of the valley splitting, E_{VS} , via electrostatic gating. To determine E_{VS} , we use two different experimental approaches. One utilises the rapid increase in spin relaxation at the hot-spot, and is applicable in the low magnetic field regime. The other is based on magnetospectroscopy, and is relevant for high fields.

The first technique stems from the fact that the hot-spot can be reliably detected by monitoring the spin-up probability as a function of magnetic field. In Figure 7.8 (a), we show measurements of the spin-up probability performed with the same method as the one used to evaluate spin lifetimes. We see that the probability of detecting a spin-up electron decreases significantly at some magnetic fields. A sudden drop of the spin-up fraction in a narrow range of field identifies the increase in relaxation rate associated with the hot-spot. Given that valley and Zeeman splittings coincide at the hot-spot, one can extract the valley separation as $E_{\text{VS}} = g\mu_{\text{B}}B_{\text{HS}}$, where B_{HS} is defined as the field at which the hot-spot is observed. For varying gate voltage configurations, we scan B in the range $2.8\text{T} < B < 5\text{T}$, and identify B_{HS} by setting an arbitrary probability threshold (green shaded area in Figure 7.8(a)) below which the hot-spot is assumed to occur. The use of this technique is limited to $B < 5\text{T}$ because the lifetime drop at the hot-spot can be therein confidently assessed. At higher fields the relaxation becomes increasingly fast and its enhancement at the hot-spot is indistinguishable within our measurement bandwidth ($\approx 10\text{ kHz}$).

In order to evaluate E_{VS} at higher magnetic fields, we use a more conventional

7.6 Valley Splitting Control via Electric Field Tuning

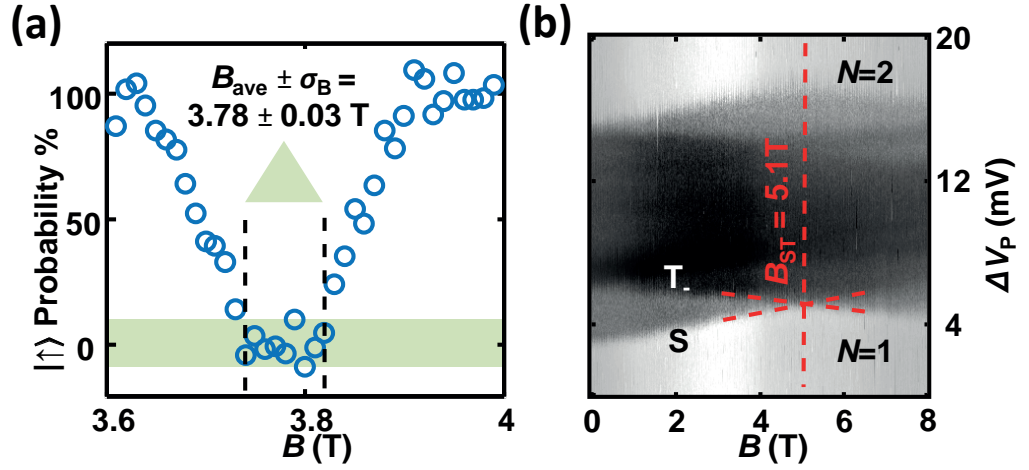


Figure 7.8: Extraction of valley splitting energies. - (a) Spin-up probability as a function of magnetic field for $V_P = 1.59$ V. The occurrence of a hot-spot minimises the spin-up fraction and allows one to extract B_{HS} (shaded area) and, in turn, E_{VS} . (b) Pulsed-voltage magnetospectroscopy showing dI_{SET}/dV_P at $N = 1 \rightarrow 2$ transition. A square pulse of amplitude 16 mV at 287 Hz is applied to gate P. The evolution of the energy difference between the singlet state (light grey) and the triplet state (dark grey) allows one to extract B_{ST} (dashed line) and, in turn, E_{VS} .

7. SPIN-VALLEY LIFETIMES IN A QD WITH TUNABLE VALLEY SPLITTING

magneto-spectroscopic approach, as shown in Figure 7.8 (b). By employing the same gate-pulsed technique used for the charge stability experiments (Figure 7.3 (a)), we focus on the singlet-triplet ground state transition as we load the second electron into the dot (i.e. $N = 1 \rightarrow 2$ transition) in the range $5\text{T} < B < 6.5\text{T}$. This is clearly identified as the point where the S (light grey feature) and T_- (dark grey feature) states cross. Here, $E_{\text{VS}} = g\mu_{\text{B}}B_{\text{ST}}$, as seen in Figure 7.6(a).

The data points in Figure 7.9 represent the measured valley separation as a function of V_{P} , obtained by means of the aforementioned techniques. The solid line fit shows remarkable consistency between the two sets of data and reveals that E_{VS} depends linearly on the gate voltage over a range of nearly $500 \mu\text{eV}$, with a slope of $640 \mu\text{eV/V}$. In order to keep constant the dot's occupancy and tunnelling rates for different V_{P} , a voltage compensation is carried out by tuning gates C1 and B accordingly. We note that we previously reported valley splittings of comparable magnitude (few hundreds of μeV) in devices realised with the same technology [88, 131]. However, to our knowledge, this is the first demonstration of the ability to accurately tune the valley splitting electrostatically in a silicon device.

A linear dependence of the valley splitting with respect to the vertical electric field has been predicted for 2DEG systems via effective mass theory [65, 118, 122]. A similar dependence for MOS-based QDs [138] has also been reported by employing atomistic tight-binding calculations [139]. In order to compare our experimental finding with the theoretical predictions, we simulate the vertical electric field (F_z) in the vicinity of the dot for the range of gate voltages used in the experiments. We employ the commercial semiconductor software ISE-TCAD [140] to model the device electrostatic potential, and thereby the electric

7.6 Valley Splitting Control via Electric Field Tuning

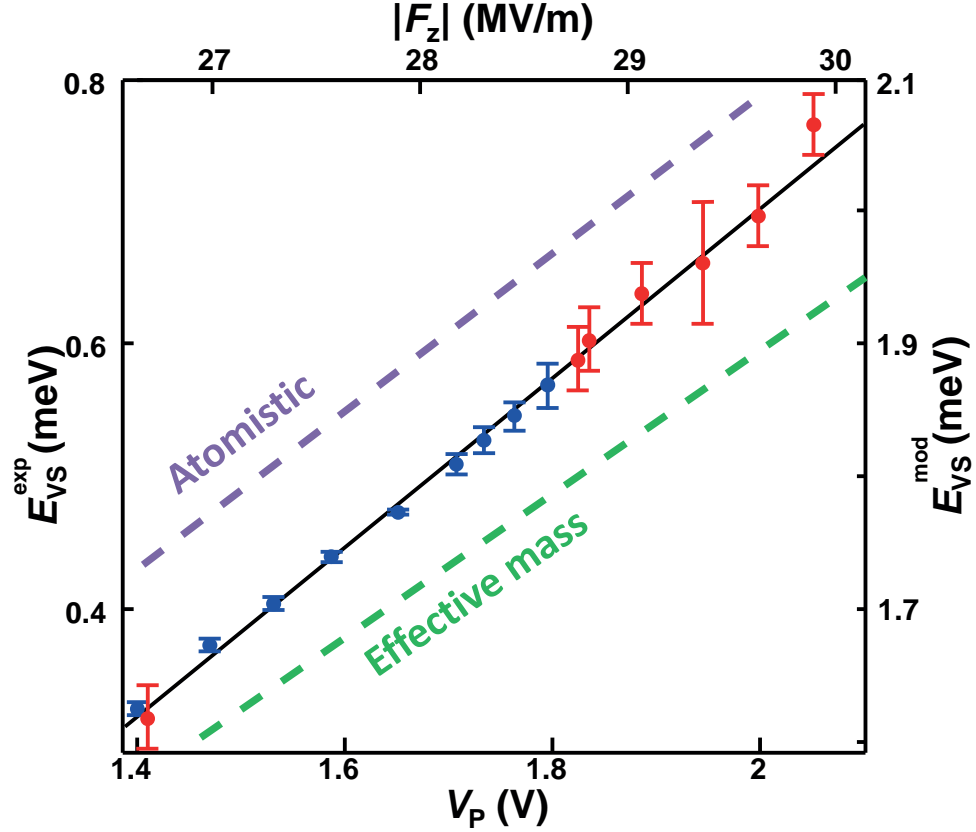


Figure 7.9: Tunability of the valley splitting via gate-voltage control. - Valley splitting as a function of plunger gate voltage (bottom axis) and modulus of interface vertical electric field in the QD (top axis). Blue and red dots show the valley separation (left axis) measured with hot-spot and magnetospectroscopic techniques, respectively. Error bars indicate standard deviations for the measured values. The linear fit (solid line) indicates a valley tunability of 0.640 meV/V. Dashed lines are calculations performed via atomistic (purple) and effective mass (green) methods (right axis, offset for clarity).

7. SPIN-VALLEY LIFETIMES IN A QD WITH TUNABLE VALLEY SPLITTING

fields in the nanostructure. For this purpose, TCAD solves the Poisson equation with an approximation of Newton's iterative method [141] to obtain convergence at low temperatures.

The spatial extent of the dot is identified by regions where the calculated conduction band energy drops below the Fermi level. Note that our calculations are performed on a three-dimensional geometry identical to the real device with the only free parameter being the amount of offset interface charge. This is adjusted to match the experimental threshold voltage of the device ($V_{th}=0.625V$). For further explanation on the TCAD simulation see the subsection 7.6.1.

The computed variation of interface electric field with gate voltage V_P is used to determine the valley splitting according to both the atomistic [138] and effective mass [118] predictions. Dashed lines in Figure 7.9 depict the trends for both approaches, with both exceeding by more than 1 meV the measured values. Despite this offset, the atomistic calculations give a tunability of the valley splitting with gate voltage, $\Delta E_{VS}/\Delta V_P$, in good agreement with the experiments.

Method	$\Delta E_{VS}/\Delta V_P$ (meV/V)
Experiment	0.640
Atomistic	0.597
Effective mass	0.541

Table 7.1: Comparison of experimental and calculated tunabilities.

The calculated value of 597 $\mu eV/V$ agrees with the measured value to within less than 7%. The value of 541 $\mu eV/V$ calculated using the effective mass approach reveals a larger deviation ($\approx 15\%$) from the experiments. The presence of an offset in the computed valley splitting may be due to the contribution of surface roughness that is not accounted for in the models, and is thought to be

7.6 Valley Splitting Control via Electric Field Tuning

responsible for a global reduction of E_{VS} [95, 100, 120, 121, 122, 123]. We emphasise, however, that the gate tunability would remain robust against this effect, which is not dependent on electric field.

7.6.1 TCAD Modelling

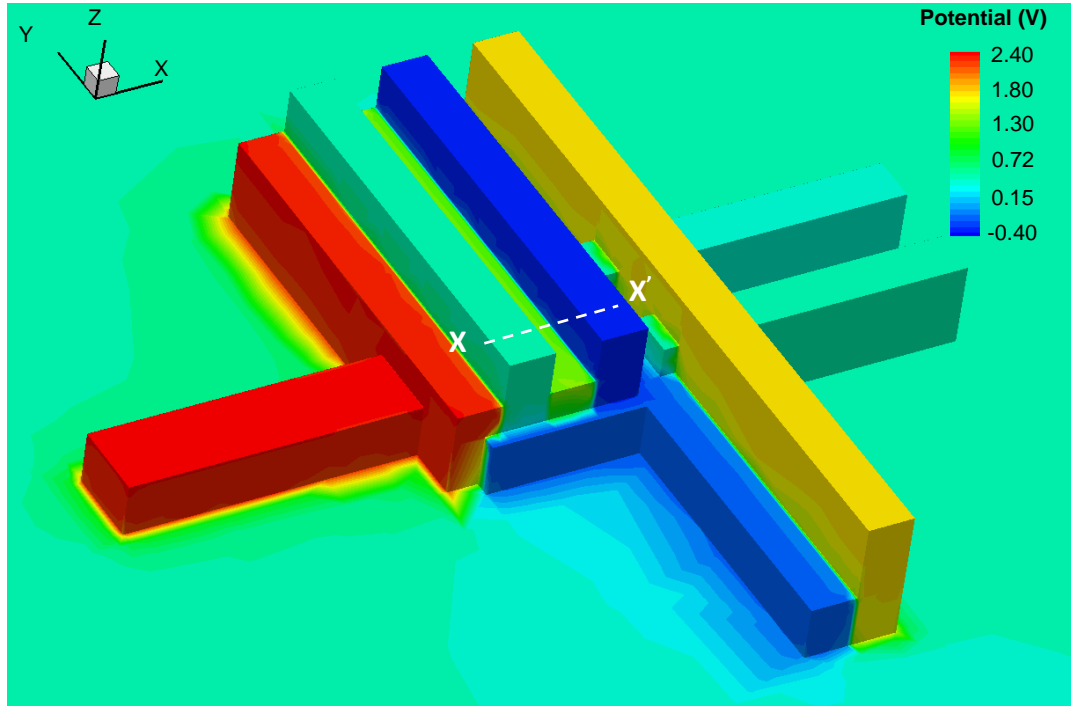


Figure 7.10: TCAD simulation model of the device. - Three-dimensional device layout used for the simulations. Color scale represents the electrostatic potential at each gate for one iteration.

The TCAD model of the real device geometry is shown in Figure 7.10. In our simulations we use the same voltage range as in the experiments and the only free parameter is the Si/SiO₂ interface charge, Q_{ox} . This has been chosen to match the experimental threshold voltage ($V_{th}=0.625$ V).

The vertical electric field profile in the (x, z) plane at $V_P=1.4$ V is shown in

7. SPIN-VALLEY LIFETIMES IN A QD WITH TUNABLE VALLEY SPLITTING

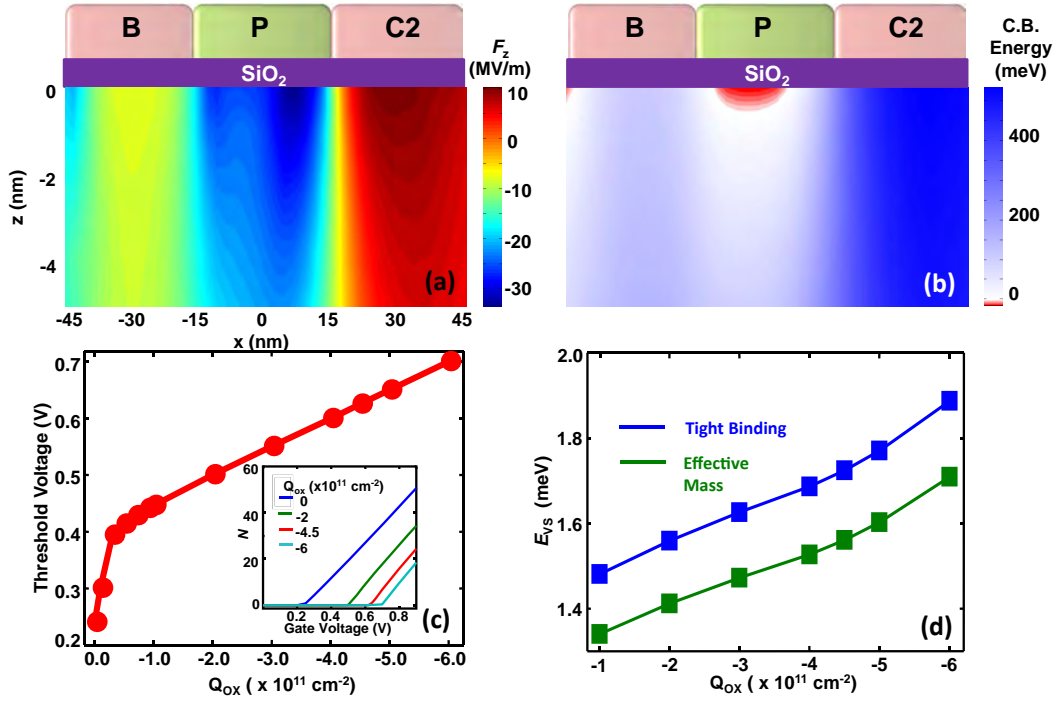


Figure 7.11: Extracted data from TCAD simulation. - (a) Two-dimensional electric field profile at $V_P=1.4\text{V}$. (b) Conduction band energy profile at $V_P=1.4\text{V}$. (c) Calculated threshold voltage as a function of interface charge. The experimental value (0.625V) is obtained at $Q_{ox} = -4.5 \times 10^{11} \text{ cm}^{-2}$. Inset: integrated electron density in the dot vs the voltage applied simultaneously to all gates for different Q_{ox} . Threshold voltage dependence on Q_{ox} can be extracted (main graph). (d) Valley splitting at $V_P=1.4\text{V}$ as a function of interface charge calculated with the atomistic (blue) and effective mass (green) predictions.

7.7 Conclusions

Figure 7.11 (a). Figure 7.11 (b) is the simulation of the conduction band profile at the same V_P , the QD is formed in the region where the conduction band falls below the Fermi energy, so that the vertical interface field therein is the one relevant to calculate the valley splitting. In Figure 7.11 (c) the dependence of V_{th} on Q_{ox} is reported. This has been evaluated by integrating the charge density in a region of the 2DEG near the interface as all the gate voltages are simultaneously swept (see inset). The value of choice is $Q_{ox} = -4.5 \times 10^{11} \text{ cm}^{-2}$. Finally, with the same methodology illustrated previously, the dependence of the valley splitting (at $V_P = 1.4\text{V}$) on the interface charge density has been estimated with both the atomistic and the effective mass theories, and is shown in Figure 7.11 (d). It is of note that the variation of E_{VS} with interface charges is relatively small and cannot account for the large offset between computed and experimental values. Hence, we believe that the main factors that reduce valley splitting in this nanostructure are due to interface effects.

The work in this Subsection 7.6.1 is led by Fahd Mohiyaddin.

7.7 Conclusions

In this chapter, we have shown that the valley splitting in a silicon device can be electrostatically controlled by simple tuning of the gate bias. We used this valley splitting control, together with spin relaxation measurements, to explore the interplay between spin and valley levels in a few-electron quantum dot.

The relaxation rates for a one-electron system exhibit a dramatic hot-spot enhancement when the spin Zeeman energy equals the valley splitting, while for a two-electron system the rates reach a minimum at this condition. We found

7. SPIN-VALLEY LIFETIMES IN A QD WITH TUNABLE VALLEY SPLITTING

that the known mechanisms for spin relaxation, such as the admixing of spin and p orbital states, were unable to explain the key features of the experimental lifetime data, and so introduced a novel approach based on admixing of valley and spin eigenstates. Our theory, which showed good agreement with experiment, implies that spin relaxation via phonon emission due to spin-orbit coupling can occur in realistic quantum dot systems, most likely due to interface disorder.

Our results show that by electrical tuning of the valley splitting in silicon quantum dots, it is possible to ensure the long lifetimes ($T_1 > 1$ s) required for robust spin qubit operation. Despite this, the excited valley state will generally be lower than orbital states in small quantum dots, placing an ultimate limit on the lifetimes accessible in very small dots, due to the spin-valley mixing described above.

Electrical manipulation of the valley states is also a fundamental requirement to perform coherent valley operations. However, the experimental relaxation rate at the observed hot-spot was found to be fast ($T_1^{-1} > 1$ kHz) for our devices, implying a fast inter-valley relaxation rate.

Finally, in the context of realizing scalable quantum computers, these results allow us to address questions of device uniformity and reproducibility with greater optimism. Indeed, our work suggests that issues related to the wide variability of the valley splitting observed in silicon nanostructures to date can shift from the elusive atomic level (surface roughness, strain, interface disorder) to the more accessible device level, where gate geometry and electrostatic confinement can be engineered to ensure robust qubit systems.

Chapter 8

Conclusion

‘We are an impossibility in an impossible universe.’

Ray Bradbury

8. CONCLUSION

8.1 Key Achievements

Feature List	Chapter 4	Chapter 5	Chapter 6	Chapter 7
Stacking layers	3	3	3	3
Number of dot(s)	1	1	1(2)*	1(2)*
Transport through QD	✓	✓	-	-
Magneto spectroscopy	✓	-	✓	✓
SET charge sensor	-	✓	✓	✓
Pulse technique	-	-	✓	✓
Spin readout	-	-	-	✓
Charging energy (meV)	3-10	3-10	10-20	10-20
Orbital split. energy (meV)	0.1 [#]	-	1-8	2-10
Valley split. energy (μ eV)	100 [#]	-	230	300-800
Relaxation time	-	-	-	2.6s

Table 8.1: Comparison between generations of devices

*Potentially 2 quantum dots.

[#]Orbital and valley splitting energies cannot be distinguished.

This thesis demonstrates how to engineer a silicon MOS-based QD, a potential candidate for realising a high-fidelity spin qubit. We successfully obtained a single electron within a QD, and determined its spin behaviour via both transport-current and charge-detection methods. The spin-filling results suggest that the g-factor in a silicon QD is very close to 2. By applying a dynamic feedback control on the gate potential from the sensor current, the charge stability diagram of the QD becomes more robust against noise and random charge moments. By extending this method, the excited states of the QD can be probed via a pulsed-gating technique. The excited states of the QD have also been studied comprehensively, including a demonstration of the QD's true 2D Fock-Darwin states, with a mixture of valley eigenstates. The individual spin of each electron was successfully

read out using a single-shot pulsing technique. It was also discovered that the spin lifetime of the electrons depends not just on the magnetic field, but also on the mixture with the valley states. By rearranging the gate potential configuration, the valley-splitting energy of the QD can be tuned, providing additional control over the QD spectrum. These breakthroughs have demonstrated that the silicon MOS QD architecture is now well positioned for the realisation of a functioning spin qubit.

Summary of the key features and results of generations of devices are presented in Table 8.1, demonstrating how each of milestones has been achieved throughout the whole thesis project.

8.2 Future Work

The research presented in this thesis can be extended in several ways. At this point, experiments based on the results of this thesis are already in progress.

First, a qubit could be realised with a single QD and a microwave control signal. By incorporating an on-chip transmission line, which generates a microwave signal, it is possible to rotate the spin of the electron within the QD. The ESR line could be fabricated in the same way as the patterned aluminium gates, and could be placed close to the QD to achieve maximum signal strength. A fully workable single qubit requires the spin to be rotated around two axes; this could be achieved by delivering an out-of-phase microwave pulses.

Second, an alternate type of qubit could be realised using singlet-triplet states, which require two coupled QDs. Figure 6.1 demonstrates an example: with the right QD on the other side turned on, it is possible to pulse the coupling gate

8. CONCLUSION

between the two QDs in various way to achieve the singlet-triplet qubit.

Finally, the unique property of valleys in silicon may offer new paths for quantum computation. Valleys in silicon QDs is a field yet to be explored, as shown in Chapter 7, which looks into the interplay between spin and valley physics. Although the valley-involved lifetimes are believed to be shorter than spins, this additional degree of freedom in silicon may provide advantages over other platforms, presenting a spin-valley hybrid type of qubit.

References

- [1] G. E. Moore. **Cramming more components onto integrated circuits** (1965). 2
- [2] R. P. Feynman. **Simulating physics with computers.** *International Journal of Theoretical Physics*, **21**(6), 467 (1982). 3
- [3] P. W. Shor. **Algorithms for quantum computation: discrete logarithms and factoring.** In *Foundations of Computer Science, 1994 Proceedings., 35th Annual Symposium on*, pages 124-134. IEEE (1994). 3
- [4] L. K. Grover. **A fast quantum mechanical algorithm for database search.** In *Proceedings of the twenty-eighth annual ACM symposium on Theory of computing*, pages 212-219. ACM (1996). 3
- [5] J. I. Cirac and P. Zoller. **Quantum computations with cold trapped ions.** *Physical Review Letters*, **74**(20), 4091 (1995). 3
- [6] E. Knill, R. Laflamme, and G. J. Milburn. **A scheme for efficient quantum computation with linear optics.** *Nature*, **409**(6816), 46 (2001). 3
- [7] Y. Makhlin, G. Schön, and A. Shnirman. **Quantum-state engineering**

REFERENCES

- with Josephson-junction devices.** *Reviews of Modern Physics*, **73**(2), 357 (2001). 3
- [8] T. Hayashi, T. Fujisawa, H. D. Cheong, Y. H. Jeong, and Y. Hirayama. **Coherent Manipulation of Electronic States in a Double Quantum Dot.** *Physical Review Letters*, **91**(22), 226804 (2003). 3
- [9] J. Gorman, D. Hasko, and D. Williams. **Charge-qubit operation of an isolated double quantum dot.** *Physical Review Letters*, **95**(9), 090502 (2005). 3
- [10] D. Loss and D. P. DiVincenzo. **Quantum computation with quantum dots.** *Physical Review A*, **57**(1), 120 (1998). 3, 15
- [11] J. R. Petta, A. C. Johnson, J. M. Taylor, E. A. Laird, A. Yacoby, M. D. Lukin, C. M. Marcus, M. P. Hanson, and A. C. Gossard. **Coherent Manipulation of Coupled Electron Spins in Semiconductor Quantum Dots.** *Science*, **309**(5744), 2180 (2005). 3, 11, 16, 66
- [12] I. Chiorescu, Y. Nakamura, C. M. Harmans, and J. Mooij. **Coherent quantum dynamics of a superconducting flux qubit.** *Science*, **299**(5614), 1869 (2003). 4
- [13] B. E. Kane. **A silicon-based nuclear spin quantum computer.** *Nature*, **393**(6681), 133 (1998). 4
- [14] S. J. Angus, A. J. Ferguson, A. S. Dzurak, and R. G. Clark. **Gate-defined quantum dots in intrinsic silicon.** *Nano Letters*, **7**(7), 2051 (2007). 4, 21, 44, 68, 99

REFERENCES

-
- [15] W. H. Lim, F. A. Zwanenburg, H. Huebl, M. Möttönen, K. W. Chan, A. Morello, and A. S. Dzurak. **Observation of the single-electron regime in a highly tunable silicon quantum dot.** *Applied Physics Letters*, **95**, 242102 (2009). 4, 45, 56, 68, 91
 - [16] F. Koppens, C. Buizert, K.-J. Tielrooij, I. Vink, K. Nowack, T. Meunier, L. Kouwenhoven, and L. Vandersypen. **Driven coherent oscillations of a single electron spin in a quantum dot.** *Nature*, **442**(7104), 766 (2006). 11
 - [17] K. Nowack, F. Koppens, Y. V. Nazarov, and L. Vandersypen. **Coherent control of a single electron spin with electric fields.** *Science*, **318**(5855), 1430 (2007). 11
 - [18] S. Nadj-Perge, S. Frolov, E. Bakkers, and L. P. Kouwenhoven. **Spin-orbit qubit in a semiconductor nanowire.** *Nature*, **468**(7327), 1084 (2010). 11
 - [19] B. Maune, M. Borselli, B. Huang, T. Ladd, P. Deelman, K. Holabird, A. Kiselev, I. Alvarado-Rodriguez, R. Ross, and A. Schmitz. **Coherent singlet-triplet oscillations in a silicon-based double quantum dot.** *Nature*, **481**(7381), 344 (2012). 11, 21
 - [20] J. J. Pla, K. Y. Tan, J. P. Dehollain, W. H. Lim, J. J. L. Morton, D. N. Jamieson, A. S. Dzurak, and A. Morello. **A single-atom electron spin qubit in silicon.** *Nature*, **489**(7417), 541 (2012). 11, 14, 47
 - [21] E. Rashba. **Properties of semiconductors with an extremum loop.**
1. Cyclotron and combinational resonance in a magnetic field per-

REFERENCES

- pendicular to the plane of the loop.** *Soviet Physics, Solid State*, **2**, 1109 (1960). 13
- [22] Y. A. Bychkov and E. I. Rashba. **Oscillatory effects and the magnetic susceptibility of carriers in inversion layers.** *Journal of Physics C: Solid State Physics*, **17**(33), 6039 (1984). 13
- [23] G. Dresselhaus. **Spin-orbit coupling effects in zinc blende structures.** *Physical Review*, **100**(2), 580 (1955). 13
- [24] M. Dyakonov and V. Y. Kachorovskii. **Spin relaxation of two-dimensional electrons in noncentrosymmetric semiconductors.** *Soviet Physics Semiconductors*, **20**(1), 110 (1986). 13
- [25] R. Winkler. *Spin-orbit coupling effects in two-dimensional electron and hole systems.* Springer (2003). 13
- [26] A. V. Khaetskii and Y. V. Nazarov. **Spin relaxation in semiconductor quantum dots.** *Physical Review B*, **61**(19), 12639 (2000). 14
- [27] A. V. Khaetskii and Y. V. Nazarov. **Spin-flip transitions between Zeeman sublevels in semiconductor quantum dots.** *Physical Review B*, **64**(12), 125316 (2001). 14, 15
- [28] R. Hanson, L. Kouwenhoven, J. Petta, S. Tarucha, and L. Vandersypen. **Spins in few-electron quantum dots.** *Reviews of Modern Physics*, **79**(4), 1217 (2007). 14, 15, 62, 99, 117
- [29] T. Fujisawa, D. G. Austing, Y. Tokura, Y. Hirayama, and S. Tarucha. **Al-**

REFERENCES

-
- lowed and forbidden transitions in artificial hydrogen and helium atoms. *Nature*, **419**(6904), 278 (2002). 14
- [30] T. Fujisawa, D. G. Austing, Y. Tokura, Y. Hirayama, and S. Tarucha. **Nonequilibrium transport through a vertical quantum dot in the absence of spin-flip energy relaxation.** *Physical Review Letters*, **88**(23), 236802 (2002). 14
- [31] R. Hanson, B. Witkamp, L. Vandersypen, L. W. van Beveren, J. Elzerman, and L. Kouwenhoven. **Zeeman energy and spin relaxation in a one-electron quantum dot.** *Physical Review Letters*, **91**(19), 196802 (2003). 14
- [32] R. Hanson, L. W. van Beveren, I. Vink, J. Elzerman, W. Naber, F. Koppens, L. Kouwenhoven, and L. Vandersypen. **Single-shot readout of electron spin states in a quantum dot using spin-dependent tunnel rates.** *Physical Review Letters*, **94**(19), 196802 (2005). 14
- [33] J. Elzerman, R. Hanson, L. H. W. Van Beveren, B. Witkamp, L. Vandersypen, and L. P. Kouwenhoven. **Single-shot read-out of an individual electron spin in a quantum dot.** *Nature*, **430**(6998), 431 (2004). 14, 74, 102
- [34] M. Kroutvar, Y. Ducommun, D. Heiss, M. Bichler, D. Schuh, G. Abstreiter, and J. J. Finley. **Optically programmable electron spin memory using semiconductor quantum dots.** *Nature*, **432**(7013), 81 (2004). 14
- [35] T. Meunier, I. Vink, L. W. van Beveren, K. Tielrooij, R. Hanson, F. Koppens, H. Tranitz, W. Wegscheider, L. Kouwenhoven, and L. Vandersypen.

REFERENCES

- Experimental signature of phonon-mediated spin relaxation in a two-electron quantum dot.** *Physical Review Letters*, **98**(12), 126601 (2007). 14
- [36] C. Simmons, J. Prance, B. Van Bael, T. S. Koh, Z. Shi, D. Savage, M. Laggally, R. Joynt, M. Friesen, and S. Coppersmith. **Tunable Spin Loading and T_1 of a Silicon Spin Qubit Measured by Single-Shot Readout.** *Physical Review Letters*, **106**(15), 156804 (2011). 14, 18, 21, 93, 98
- [37] C.H. Yang, A. Rossi, R. Ruskov, N. S. Lai, F. A. Mohiyaddin, S. Lee, C. Tahan, G. Klimeck, A. Morello, and A. S. Dzurak. **Spin-valley lifetimes in a silicon quantum dot with tunable valley splitting.** *Nature Communications*, **4** (2013). 14, 110, 111, 112, 115, 116
- [38] F. Marquardt and V. A. Abalmasov. **Spin relaxation in a quantum dot due to Nyquist noise.** *Physical Review B*, **71**(16), 165325 (2005). 14
- [39] M. Borhani, V. N. Golovach, and D. Loss. **Spin decay in a quantum dot coupled to a quantum point contact.** *Physical Review B*, **73**(15), 155311 (2006). 14
- [40] L. Woods, T. Reinecke, and Y. Lyanda-Geller. **Spin relaxation in quantum dots.** *Physical Review B*, **66**(16), 161318 (2002). 15
- [41] V. N. Golovach, A. Khaetskii, and D. Loss. **Phonon-induced decay of the electron spin in quantum dots.** *Physical Review Letters*, **93**(1), 016601 (2004). 15

REFERENCES

-
- [42] D. V. Bulaev and D. Loss. **Spin relaxation and anticrossing in quantum dots: Rashba versus Dresselhaus spin-orbit coupling.** *Physical Review B*, **71**(20), 205324 (2005). 15, 99, 109
 - [43] B. Glavin and K. Kim. **Spin-lattice relaxation in Si quantum dots.** *Physical Review B*, **68**(4), 045308 (2003). 15, 109
 - [44] C. Tahan. **Silicon in the Quantum Limit: Quantum Computing and Decoherence in Silicon Architectures.** *arXiv preprint arXiv:0710.4263* (2007). 15, 109
 - [45] S. Amasha, K. MacLean, I. Radu, D. Zumbuhl, M. Kastner, M. Hanson, and A. Gossard. **Measurements of the spin relaxation rate at low magnetic fields in a quantum dot.** *arXiv preprint cond-mat/0607110* (2006). 15
 - [46] A. Morello, J. J. Pla, F. A. Zwanenburg, K. W. Chan, K. Y. Tan, H. Huebl, M. Möttönen, C. D. Nugroho, C. Yang, and J. A. van Donkelaar. **Single-shot readout of an electron spin in silicon.** *Nature*, **467**(7316), 687 (2010). 15, 68, 74, 98, 107
 - [47] M. Raith, P. Stano, and J. Fabian. **Theory of single electron spin relaxation in Si/SiGe lateral coupled quantum dots.** *Physical Review B*, **83**(19), 195318 (2011). 15, 99, 109
 - [48] S. Tarucha, D. Austing, T. Honda, R. Van der Hage, and L. Kouwenhoven. **Shell filling and spin effects in a few electron quantum dot.** *Physical Review Letters*, **77**(17), 3613 (1996). 16, 17, 54, 56, 104

REFERENCES

- [49] L. P. Kouwenhoven, D. Austing, and S. Tarucha. **Few-electron quantum dots**. *Reports on Progress in Physics*, **64**(6), 701 (2001). 16, 104
- [50] D. Sprinzak, Y. Ji, M. Heiblum, D. Mahalu, and H. Shtrikman. **Charge distribution in a Kondo-correlated quantum dot**. *Physical Review Letters*, **88**(17), 176805 (2002). 17
- [51] J. Elzerman, R. Hanson, J. Greidanus, L. H. W. Van Beveren, S. De Franceschi, L. Vandersypen, S. Tarucha, and L. Kouwenhoven. **Few-electron quantum dot circuit with integrated charge read out**. *Physical Review B*, **67**(16), 161308 (2003). 17, 68, 74
- [52] L. DiCarlo, H. Lynch, A. Johnson, L. Childress, K. Crockett, C. Marcus, M. Hanson, and A. Gossard. **Differential charge sensing and charge delocalization in a tunable double quantum dot**. *Physical Review Letters*, **92**(22), 226801 (2004). 17, 68, 74
- [53] J. Petta, A. Johnson, C. Marcus, M. Hanson, and A. Gossard. **Manipulation of a single charge in a double quantum dot**. *Physical Review Letters*, **93**(18), 186802 (2004). 17, 68, 74
- [54] A. Johnson, J. Petta, C. Marcus, M. Hanson, and A. Gossard. **Singlet-triplet spin blockade and charge sensing in a few-electron double quantum dot**. *Physical Review B*, **72**(16), 165308 (2005). 17, 68, 74
- [55] M. Cassidy, A. Dzurak, R. Clark, K. Petersson, I. Farrer, D. Ritchie, and C. Smith. **Single shot charge detection using a radio-frequency quantum point contact**. *Applied Physics Letters*, **91**(22), 222104 (2007). 17, 68, 74

REFERENCES

-
- [56] M. Pioro-Ladriere, T. Obata, Y. Tokura, Y.-S. Shin, T. Kubo, K. Yoshida, T. Taniyama, and S. Tarucha. **Electrically driven single-electron spin resonance in a slanting Zeeman field.** *Nature Physics*, **4**(10), 776 (2008). 17
- [57] T. Obata, M. Pioro-Ladriere, Y. Tokura, Y.-S. Shin, T. Kubo, K. Yoshida, T. Taniyama, and S. Tarucha. **Coherent manipulation of individual electron spin in a double quantum dot integrated with a micro-magnet.** *Physical Review B*, **81**(8), 085317 (2010). 17
- [58] T. Fujisawa, T. Hayashi, H. Cheong, Y. Jeong, and Y. Hirayama. **Rotation and phase-shift operations for a charge qubit in a double quantum dot.** *Physica E: Low-dimensional Systems and Nanostructures*, **21**(2), 1046 (2004). 18
- [59] M. A. Eriksson, M. Friesen, S. N. Coppersmith, R. Joynt, L. J. Klein, K. Slinker, C. Tahan, P. Mooney, J. Chu, and S. Koester. *Spin-based quantum dot quantum computing in silicon*, pages 133-146. Springer (2005). 18
- [60] C. Simmons, M. Thalakulam, N. Shaji, L. J. Klein, H. Qin, R. Blick, D. Savage, M. Lagally, S. Coppersmith, and M. Eriksson. **Single-electron quantum dot in Si/SiGe with integrated charge sensing.** *Applied Physics Letters*, **91**(21), 213103 (2007). 18, 68, 74
- [61] C. Simmons, M. Thalakulam, B. Rosemeyer, B. Van Bael, E. Sackmann, D. Savage, M. Lagally, R. Joynt, M. Friesen, and S. Coppersmith. **Charge**

REFERENCES

- sensing and controllable tunnel coupling in a Si/SiGe double quantum dot. *Nano Letters*, **9**(9), 3234 (2009). 18, 68, 74
- [62] M. A. Eriksson, J. R. Prance, Z. Shi, C. Simmons, J. K. Gamble, T. S. Koh, D. Savage, M. Lagally, L. Schreiber, and L. Vandersypen. **Single-Shot Measurement of One and Two-Electron Spin States in Si/SiGe Gated Quantum Dots**. In *Silicon-Germanium Technology and Device Meeting (ISTDM), 2012 International*, pages 1-2. IEEE (2012). 18
- [63] J. Prance, Z. Shi, C. Simmons, D. Savage, M. Lagally, L. Schreiber, L. Vandersypen, M. Friesen, R. Joynt, and S. Coppersmith. **Single-shot measurement of triplet-singlet relaxation in a Si/SiGe double quantum dot**. *Physical Review Letters*, **108**(4), 46808 (2012). 18, 21
- [64] T. S. Koh, J. K. Gamble, M. Friesen, M. Eriksson, and S. Coppersmith. **Pulse-Gated Quantum-Dot Hybrid Qubit**. *Physical Review Letters*, **109**(25), 250503 (2012). 18
- [65] T. Boykin, G. Klimeck, M. Eriksson, M. Friesen, S. Coppersmith, P. Von Allmen, F. Oyafuso, and S. Lee. **Valley splitting in strained silicon quantum wells**. *Applied Physics Letters*, **84**, 115 (2004). 19, 98, 120
- [66] D. Culcer, Ł. Cywiński, Q. Li, X. Hu, and S. D. Sarma. **Quantum dot spin qubits in silicon: Multivalley physics**. *Physical Review B*, **82**(15), 155312 (2010). 19, 28, 66, 93, 94
- [67] S. Goswami, K. Slinker, M. Friesen, L. McGuire, J. Truitt, C. Tahan, L. Klein, J. Chu, P. Mooney, and D. Van Der Weide. **Controllable valley**

REFERENCES

-
- splitting in silicon quantum devices.** *Nature Physics*, **3**(1), 41 (2006).
19, 98
- [68] K. Takashina, Y. Ono, A. Fujiwara, Y. Takahashi, and Y. Hirayama. **Valley Polarization in Si(100) at Zero Magnetic Field.** *Physical Review Letters*, **96**(23), 236801 (2006). 19, 98
- [69] Y. Wu, Y. Cui, L. Huynh, C. Barrelet, D. Bell, and C. Lieber. **Controlled growth and structures of molecular-scale silicon nanowires.** *Nano Letters*, **4**(3), 433 (2004). 19
- [70] Z. Zhong, Y. Fang, W. Lu, and C. Lieber. **Coherent single charge transport in molecular-scale silicon nanowires.** *Nano Letters*, **5**(6), 1143 (2005). 19
- [71] F. Zwanenburg, C. van Rijmenam, Y. Fang, C. Lieber, and L. Kouwenhoven. **Spin states of the first four holes in a silicon nanowire quantum dot.** *Nano Letters*, **9**(3), 1071 (2009). 19
- [72] S. P. Dash, S. Sharma, R. S. Patel, M. P. de Jong, and R. Jansen. **Electrical creation of spin polarization in silicon at room temperature.** *Nature*, **462**(7272), 491 (2009). 19
- [73] D. Cobden and J. Nygrd. **Shell filling in closed single-wall carbon nanotube quantum dots.** *Physical Review Letters*, **89**(4), 46803 (2002).
20
- [74] P. Jarillo-Herrero, S. Sapmaz, C. Dekker, L. Kouwenhoven, and H. van der

REFERENCES

- Zant. **Electron-hole symmetry in a semiconducting carbon nanotube quantum dot.** *Nature*, **429**(6990), 389 (2004). 20
- [75] K. Novoselov, A. K. Geim, S. Morozov, D. Jiang, Y. Zhang, S. Dubonos, I. Grigorieva, and A. Firsov. **Electric field effect in atomically thin carbon films.** *Science*, **306**(5696), 666 (2004). 20
- [76] K. Novoselov, A. K. Geim, S. Morozov, D. Jiang, M. K. I. Grigorieva, S. Dubonos, and A. Firsov. **Two-dimensional gas of massless Dirac fermions in graphene.** *Nature*, **438**(7065), 197 (2005). 20
- [77] Y. Zhang, Y.-W. Tan, H. L. Stormer, and P. Kim. **Experimental observation of the quantum Hall effect and Berry's phase in graphene.** *Nature*, **438**(7065), 201 (2005). 20
- [78] J. W. McClure. **Diamagnetism of Graphite.** *Physical Review*, **104**(3), 666 (1956). 20
- [79] B. Trauzettel, D. V. Bulaev, D. Loss, and G. Burkard. **Spin qubits in graphene quantum dots.** *Nature Physics*, **3**(3), 192 (2007). 20
- [80] H. Min, J. Hill, N. Sinitsyn, B. Sahu, L. Kleinman, and A. MacDonald. **Intrinsic and Rashba spin-orbit interactions in graphene sheets.** *Physical Review B*, **74**(16), 165310 (2006). 20
- [81] D. Huertas-Hernando, F. Guinea, and A. Brataas. **Spin-orbit coupling in curved graphene, fullerenes, nanotubes, and nanotube caps.** *Physical Review B*, **74**(15), 155426 (2006). 20

REFERENCES

-
- [82] C. Volk, C. Neumann, S. Kazarski, S. Fringes, S. Engels, F. Haupt, A. Mller, and C. Stampfer. **Probing relaxation times in graphene quantum dots.** *Nature Communications*, **4**, 1753 (2013). 20
 - [83] N. Lai, W. Lim, C. Yang, F. Zwanenburg, W. Coish, F. Qassemi, A. Morello, and A. Dzurak. **Pauli spin blockade in a highly tunable silicon double quantum dot.** *Scientific Reports*, **1** (2011). 21
 - [84] W. M. Witzel, M. S. Carroll, A. Morello, Ł. Cywiński, and S. Das Sarma. **Electron spin decoherence in isotope-enriched silicon.** *Physical Review Letters*, **105**(18), 187602 (2010). 21
 - [85] A. Tyryshkin, S. Lyon, A. Astashkin, and A. Raitsimring. **Electron spin relaxation times of phosphorus donors in silicon.** *Physical Review B*, **68**(19), 193207 (2003). 21
 - [86] A. M. Tyryshkin, S. Tojo, J. J. L. Morton, H. Riemann, N. V. Abrosimov, P. Becker, H. J. Pohl, T. Schenkel, M. L. W. Thewalt, and K. M. Itoh. **Electron spin coherence exceeding seconds in high-purity silicon.** *Nature Materials*, **11**(2), 143 (2011). 21
 - [87] T. Ando, A. B. Fowler, and F. Stern. **Electronic properties of two-dimensional systems.** *Reviews of Modern Physics*, **54**, 437 (1982). 21, 92, 98
 - [88] W. Lim, C. Yang, F. Zwanenburg, and A. Dzurak. **Spin filling of valley-orbit states in a silicon quantum dot.** *Nanotechnology*, **22**(33), 335704 (2011). 21, 60, 92, 93, 120

REFERENCES

- [89] M. G. Borselli, R. S. Ross, A. A. Kiselev, E. T. Croke, K. S. Holabird, P. W. Deelman, L. D. Warren, I. Alvarado-Rodriguez, I. Milosavljevic, and F. C. Ku. **Measurement of valley splitting in high-symmetry Si/SiGe quantum dots.** *Applied Physics Letters*, **98**(12), 123118 (2011). 21, 56, 93, 104
- [90] J. R. Chelikowsky and M. L. Cohen. **Electronic structure of silicon.** *Physical Review B*, **10**(12), 5095 (1974). 24
- [91] M. Xiao, M. House, and H. Jiang. **Parallel spin filling and energy spectroscopy in few-electron Si metal-on-semiconductor-based quantum dots.** *Applied Physics Letters*, **97**(3), 032103 (2010). 27, 64, 68, 74
- [92] M. Xiao, M. House, and H. Jiang. **Measurement of the spin relaxation time of single electrons in a silicon metal-oxide-semiconductor-based quantum dot.** *Physical Review Letters*, **104**(9), 096801 (2010). 27, 93, 98
- [93] M. House, H. Pan, M. Xiao, and H. Jiang. **Non-equilibrium charge stability diagrams of a silicon double quantum dot.** *Applied Physics Letters*, **99**, 112116 (2011). 27
- [94] B. Koiller, X. Hu, and S. Das Sarma. **Exchange in Silicon-Based Quantum Computer Architecture.** *Physical Review Letters*, **88**(2), 027903 (2001). 28
- [95] D. Culcer, X. Hu, and S. D. Sarma. **Interface roughness, valley-orbit**

REFERENCES

-
- coupling, and valley manipulation in quantum dots.** *Physical Review B*, **82**(20), 205315 (2010). 28, 123
- [96] L. P. Kouwenhoven, C. Markus, P. L. McEuen, S. Tarucha, R. M. Westervelt, and N. S. Wingreen. **Electron transport in quantum dots.** *NATO ASI Series E Applied Sciences-Advanced Study Institute*, **345**, 105 (1997). 32, 54, 61
- [97] W. Lim, H. Huebl, L. van Beveren, S. Rubanov, P. Spizzirri, S. Angus, R. Clark, and A. Dzurak. **Electrostatically defined few-electron double quantum dot in silicon.** *Applied Physics Letters*, **94**, 173502 (2009). 46, 47
- [98] 51
FEMTO Messtechnik GmbH.
- [99] M. Ciorga, A. Sachrajda, P. Hawrylak, C. Gould, P. Zawadzki, S. Jullian, Y. Feng, and Z. Wasilewski. **Addition spectrum of a lateral dot from Coulomb and spin-blockade spectroscopy.** *Physical Review B*, **61**(24), 16315 (2000). 54
- [100] M. Friesen and S. Coppersmith. **Theory of valley-orbit coupling in a Si/SiGe quantum dot.** *Physical Review B*, **81**(11), 115324 (2010). 58, 80, 123
- [101] Y. Hada and M. Eto. **Electronic states in silicon quantum dots: Multivalley artificial atoms.** *Physical Review B*, **68**(15), 155322 (2003). 59, 60, 64, 66

REFERENCES

- [102] D. Weinmann, W. Husler, and B. Kramer. **Spin blockades in linear and nonlinear transport through quantum dots.** *Physical Review Letters*, **74**(6), 984 (1995). 66
- [103] L. Rokhinson, L. Guo, S. Chou, and D. Tsui. **Spin transitions in a small Si quantum dot.** *Physical Review B*, **63**(3), 035321 (2001). 66
- [104] B. Hu and C. Yang. **Electron spin blockade and singlet-triplet transition in a silicon single electron transistor.** *Physical Review B*, **80**(7), 075310 (2009). 66
- [105] M. Field, C. Smith, M. Pepper, D. Ritchie, J. Frost, G. Jones, and D. Hasko. **Measurements of Coulomb blockade with a noninvasive voltage probe.** *Physical Review Letters*, **70**(9), 1311 (1993). 68
- [106] J. Elzerman, R. Hanson, L. Willems van Beveren, L. Vandersypen, and L. Kouwenhoven. **Excited-state spectroscopy on a nearly closed quantum dot via charge detection.** *Applied Physics Letters*, **84**(23), 4617 (2004). 68, 82, 105, 107
- [107] E. Nordberg, H. Stalford, R. Young, G. Ten Eyck, K. Eng, L. Tracy, K. Childs, J. Wendt, R. Grubbs, and J. Stevens. **Charge sensing in enhancement mode double-top-gated metal-oxide-semiconductor quantum dots.** *Applied Physics Letters*, **95**(20), 202102 (2009). 68, 74
- [108] Y. Hu, H. O. H. Churchill, D. J. Reilly, J. Xiang, C. M. Lieber, and C. M. Marcus. **A Ge/Si heterostructure nanowire-based double quantum dot with integrated charge sensor.** *Nature Nanotechnology*, **2**(10), 622 (2007). 68, 69, 74

REFERENCES

-
- [109] M. Biercuk, D. Reilly, T. Buehler, V. Chan, J. Chow, R. Clark, and C. Marcus. **Charge sensing in carbon-nanotube quantum dots on microsecond timescales.** *Physical Review B*, **73**(20), 201402 (2006). 68, 69, 74
 - [110] L. J. Wang, G. Cao, T. Tu, H. O. Li, C. Zhou, X. J. Hao, Z. Su, G. C. Guo, H. W. Jiang, and G. P. Guo. **A graphene quantum dot with a single electron transistor as an integrated charge sensor.** *Applied Physics Letters*, **97**(26), 262113 (2010). 68, 74
 - [111] G. Podd, S. Angus, D. Williams, and A. Ferguson. **Charge sensing in intrinsic silicon quantum dots.** *Applied Physics Letters*, **96**(8), 082104 (2010). 68, 74
 - [112] S. Angus, A. Ferguson, A. Dzurak, and R. Clark. **A silicon radio-frequency single electron transistor.** *Applied Physics Letters*, **92**(11), 112103 (2008). 68, 78
 - [113] T. Buehler, V. Chan, A. Ferguson, A. Dzurak, F. Hudson, D. Reilly, A. Hamilton, R. Clark, D. Jamieson, and C. Yang. **Controlled single electron transfer between Si: P dots.** *Applied Physics Letters*, **88**(19), 192101 (2006). 69
 - [114] D. Culcer, Ł. Cywiński, Q. Li, X. Hu, and S. D. Sarma. **Realizing singlet-triplet qubits in multivalley Si quantum dots.** *Physical Review B*, **80**(20), 205302 (2009). 80, 98
 - [115] G. Klimeck, R. Lake, S. Datta, and G. W. Bryant. **Elastic and inelas-**

REFERENCES

- tic scattering in quantum dots in the Coulomb-blockade regime. *Physical Review B*, **50**(8), 5484 (1994). 82
- [116] C. Yang, W. Lim, F. Zwanenburg, and A. Dzurak. **Dynamically controlled charge sensing of a few-electron silicon quantum dot.** *AIP Advances*, **1**(4), 042111 (2011). 82, 102
- [117] L. M. Roth. **g factor and donor spin-lattice relaxation for electrons in Germanium and Silicon.** *Physical Review*, **118**(6), 1534 (1960). 91
- [118] A. Saraiva, M. Caldern, R. B. Capaz, X. Hu, S. D. Sarma, and B. Koiller. **Intervalley coupling for interface-bound electrons in silicon: An effective mass study.** *Physical Review B*, **84**(15), 155320 (2011). 93, 98, 120, 122
- [119] L. Sham and M. Nakayama. **Effective-mass approximation in the presence of an interface.** *Physical Review B*, **20**(2), 734 (1979). 98
- [120] A. Saraiva, M. Caldern, X. Hu, S. D. Sarma, and B. Koiller. **Physical mechanisms of interface-mediated intervalley coupling in Si.** *Physical Review B*, **80**(8), 081305 (2009). 98, 123
- [121] T. Ando. **Valley splitting in the silicon inversion layer: Misorientation effects.** *Physical Review B*, **19**(6), 3089 (1979). 98, 123
- [122] M. Friesen, S. Chutia, C. Tahan, and S. Coppersmith. **Valley splitting theory of SiGe Si SiGe quantum wells.** *Physical Review B*, **75**(11), 115318 (2007). 98, 120, 123

REFERENCES

-
- [123] M. Friesen, M. Eriksson, and S. Coppersmith. **Magnetic field dependence of valley splitting in realistic Si SiGe quantum wells.** *Applied Physics Letters*, **89**, 202106 (2006). 98, 123
 - [124] G. P. Lansbergen, R. Rahman, J. Verduijn, G. C. Tettamanzi, N. Collaert, S. Biesemans, G. Klimeck, L. C. L. Hollenberg, and S. Rogge. **Lifetime-Enhanced Transport in Silicon due to Spin and Valley Blockade.** *Physical Review Letters*, **107**(13), 136602 (2011). 98
 - [125] B. Roche, E. Dupont-Ferrier, B. Voisin, M. Cobian, X. Jehl, R. Wacquez, M. Vinet, Y.-M. Niquet, and M. Sanquer. **Detection of a large valley-orbit splitting in silicon with two-donor spectroscopy.** *Physical Review Letters*, **108**(20), 206812 (2012). 98
 - [126] Q. Li, Ł. Cywiński, D. Culcer, X. Hu, and S. D. Sarma. **Exchange coupling in silicon quantum dots: Theoretical considerations for quantum computation.** *Physical Review B*, **81**(8), 085313 (2010). 98
 - [127] V. Smelyanskiy, A. Petukhov, and V. Osipov. **Quantum computing on long-lived donor states of Li in Si.** *Physical Review B*, **72**(8), 081304 (2005). 98
 - [128] D. Culcer, A. Saraiva, B. Koiller, X. Hu, and S. D. Sarma. **Valley-based noise-resistant quantum computation using Si quantum dots.** *Physical Review Letters*, **108**(12), 126804 (2012). 98
 - [129] R. R. Hayes, A. A. Kiselev, M. G. Borselli, S. S. Bui, E. T. Croke III, P. W. Deelman, B. M. Maune, I. Milosavljevic, J.-S. Moon, and R. S. Ross.

REFERENCES

- Lifetime measurements (T1) of electron spins in Si/SiGe quantum dots.** *arXiv preprint arXiv:0908.0173* (2009). 98, 109
- [130] F. A. Zwanenburg, A. S. Dzurak, A. Morello, M. Y. Simmons, L. C. Hollenberg, G. Klimeck, S. Rogge, S. N. Coppersmith, and M. A. Eriksson. **Silicon Quantum Electronics.** *arXiv preprint arXiv:1206.5202* (2012). 98, 107, 109
- [131] C. Yang, W. Lim, N. Lai, A. Rossi, A. Morello, and A. Dzurak. **Orbital and valley state spectra of a few-electron silicon quantum dot.** *Physical Review B*, **86**(11), 115319 (2012). 104, 110, 117, 120
- [132] C. Tahan, M. Friesen, and R. Joynt. **Decoherence of electron spin qubits in Si-based quantum computers.** *Physical Review B*, **66**(3), 035314 (2002). 109
- [133] P. Stano and J. Fabian. **Theory of phonon-induced spin relaxation in laterally coupled quantum dots.** *Physical Review Letters*, **96**(18), 186602 (2006). 109
- [134] P. Stano and J. Fabian. **Orbital and spin relaxation in single and coupled quantum dots.** *Physical Review B*, **74**(4), 045320 (2006). 109
- [135] Z. Wilamowski, W. Jantsch, H. Malissa, and U. Rössler. **Evidence and evaluation of the Bychkov-Rashba effect in SiGe/Si/SiGe quantum wells.** *Physical Review B*, **66**(19), 195315 (2002). 112
- [136] M. Nestoklon, L. Golub, and E. Ivchenko. **Spin and valley-orbit split-**

REFERENCES

-
- tings in SiGe Si heterostructures. *Physical Review B*, **73**(23), 235334 (2006). 112
- [137] L. Wang, K. Shen, B. Sun, and M. Wu. **Singlet-triplet relaxation in multivalley silicon single quantum dots.** *Physical Review B*, **81**(23), 235326 (2010). 117
- [138] S. Lee. *Development of a massively parallel nanoelectronic modeling tool and its application to quantum computing devices.* PhD thesis (2011). 120, 122
- [139] G. Klimeck, S. S. Ahmed, N. Kharche, M. Korkusinski, M. Usman, M. Prada, and T. B. Boykin. **Atomistic simulation of realistically sized nanodevices using NEMO 3-DPart II: Applications.** *Electron Devices, IEEE Transactions on*, **54**(9), 2090 (2007). 120
- [140] I. S. Engineering. **Dessis v10 Manual** (2004). 120
- [141] R. E. Bank and D. J. Rose. **Global approximate Newton methods.** *Numerische Mathematik*, **37**(2), 279 (1981). 122

REFERENCES
